Landslide monitoring using robust RFID localization in harsh environment

Arthur Charlety

THÈSE

Pour obtenir le grade de

DOCTEUR DE L'UNIVERSITÉ GRENOBLE ALPES

École doctorale : STEP - Sciences de la Terre de l'Environnement et des Planètes
Spécialité : Sciences de la Terre et de l'Environnement
Unité de recherche : Institut des Sciences de la Terre

Suivi de glissement de terrains par localisation de tags RFID en environnement extérieur

Landslide monitoring using robust RFID localization in harsh environment

Présentée par :

Arthur CHARLETY

Direction de thèse :

Laurent BAILLET Professeur, UGA	Directeur de thèse
Eric LAROSE DIRECTEUR DE RECHERCHE, Université Grenoble Alpes	Co-directeur de thèse
Smail TEDJINI Grenoble INP	Co-encadrant de thèse
Mathieu LE BRETON Geolithe	Co-encadrant de thèse

Rapporteurs :

Jordi VILà-VALLS
ASSOCIATE PROFESSOR, ISAE-SUPAERO
Cécile LASSERRE
DIRECTRICE DE RECHERCHE, CNRS

Thèse soutenue publiquement le **22 mars 2024**, devant le jury composé de :

Laurent BAILLET PROFESSEUR, Université Grenoble Alpes	Directeur de thèse
Jordi VILà-VALLS ASSOCIATE PROFESSOR, ISAE-SUPAERO	Rapporteur
Cécile LASSERRE DIRECTRICE DE RECHERCHE, CNRS	Rapporteure
Etienne PERRET PROFESSEUR, Grenoble INP	Président
Michel JABOYEDOFF PROFESSEUR, Université de Lausanne	Examinateur
Yvan DUROC PROFESSEUR, UNIVERSITE LYON	Examinateur

Invités :

Eric Larose
DIRECTEUR DE RECHERCHE, UGA
Mathieu Le Breton
PHYSICIEN, Géolithe

Résumé

Les glissements de terrain représentent un risque naturel majeur pour notre société. A une époque d'urbanisation continue et d'extrêmes climatiques de plus en plus fréquents, la surveillance des instabilités gravitaire est un levier essentiel pour la réduction des risques naturels. Dans ce contexte, la technologie d'identification radio-fréquence (RFID) représente un outil prometteur pour le suivi de glissement de terrain à bas-coût, via la localisation d'étiquettes RFID en mouvement. Ce travail de thèse présente différentes approches de traitement de donnée RFID long-terme en environnement extérieur, visant notamment à améliorer la stabilité des mesures de phase. Des méthodes de traitement du signal déterministes et bayesiennes (filtrage Kalman) sont développées, exploitant la redondance et la complémentarié des données. La localisation à 2D et 3D est ensuite étudiée en termes de sensibilité à la géometrie du système, puis démontrée avec une précision centimétrique. Des déplacements d'ordre métrique sont confirmés sur le secteur instrumenté. Les séries de données RFID pluriannuelles donnent accès à la cinématique du glissement de l'Harmalière (France), mettant à jour une regression de l'escarpement et des changements de comportements de surface en différentes zones du secteur instrumenté. Couplées à des observations hydrologiques et de bruit de fond sismique, les mesures de déplacement permettent d'interpréter les comportements saisonniers du glissement de l'Harmalière. Enfin, la possibilité de localiser des tags par antenne aéroportée est étudiée. La localisation par Antenne à Ouverture Synthétique est démontrée grâce à un système de mesures temps-réel GPS et RFID. La localisation sous couvert végétal et neigeux offre une précision inférieure à 10 cm, alors qu'une précision centimétrique est obtenue dans l'espace libre. La méthode d'optimisation statistiques Markov-Chain Monte Carlo est exploitée pour caractériser les résultats de localisation, offrant de nombreux avantages par rapport aux méthodes classiques. Les concepts de traitement de signal RFID et les problématiques liées aux radiofréquences, montrent des similarités avec les méthodes GPS.

Les avancées de cette thèse ouvrent de nouvelles perspectives d'applications bas-coût pour l'auscultation et la surveillance de glissements de terrain.

Abstract

Landslides represent a major natural hazard for our society. In the time of continuous urbanization and more frequent climate extremes, monitoring landslides is an essential lever for natural risk reduction. In this context, Radio-Frequency Identification (RFID) is used nowadays as a promising low-cost landslide monitoring tool, through the localization of moving RFID tags. This doctoral work presents diverse processing approaches for long-term outdoor RFID data, notably devoted to improving the stability of phase measurements. Signal processing methods are developed, both deterministic and bayesian (Kalman filter), in order to exploit data redundancy and complementarity.

2D and 3D localization is studied in terms of sensibility to system geometry, then demonstrated with a centimeter accuracy. Metric displacements are confirmed on the instrumented sector. The year-long RFID data provide insights on the kinematics of the Harmalière landslide (France), shedding light on a scarp retrogression and changes in surface behavior on different zones of the instrumented sector. Coupled to hydrological and ambient-noise seismic observations, displacement measurement allows for an interpretation of the seasonal behavior of the Harmalière landslide.

Finally, the ability to localize tags with airborne antennas is studied. Synthetic Aperture Radar localization is demonstrated using a real-time RFID an GPS measurement setup. Localization under snow and vegetation cover yields an accuracy below 10 cm, whereas free-space localization provides a centimeter accuracy. The Markov-Chain Monte Carlo statistical optimization method is exploited in order to characterize the localization results, with several advantages compared to classical methods. The signal processing concepts and the radio-frequency challenges show similarities with GPS processing. The advances of this work open new perspectives of low-cost applications in monitoring and auscultating landslide hazards.

Financement

Ce travail de thèse a été financé en partie par la région Auvergne-Rhone-Alpes, via le projet RISQID, et par Géolithe via le LabCom GEO3ILAB. Il a bénéficié de nombreux soutiens à ISTerre, au GIPSA-lab, à Geolithe. Ce travail a été hébergé par le CNRS et l'Université Grenoble Alpes.

Contents

List of Acronyms and Abbreviations

- **DOP** Dilution of Precision
- **EKF** Extended Kalman Filter
- **ETSI** European Telecommunications Standards Institute
- **EWS** Early Warning System
- **FD-PD** Frequency-Difference Phase-Difference
- **GHz** Gigahertz
- **GNSS** Global Navigation Satellite Systems
- **GPS** Global Positioning System
- **IMU** Inertial Measurement Unit
- **InSAR** Interferometric Synthetic Aperture Radar
- **IoT** Internet of Things
- **KF** Kalman Filter
- **LEWS** Landslide Early Warning System
- **LOS** Line Of Sight
- **LiDAR** Light Detecting And Ranging
- **MCMC** Markov-Chain Monte-Carlo
- **MHz** Megahertz
- **NTP** Newtork Time Protocol
- **PDoA** Phase Difference of Arrival
- **PPK** Post-Processed Kinematics
- **PPP** Precise Point Positionning
- **PSO** Particle Swarm Optimization
- **QRA** Qualitative Risk Assessment
- **RF** Radio-Frequency
- **RFID** Radio-Frequency Identification
- **RMS** Root Mean Square
- **RSSI** Received Signal Strength Indicator
- **RTK** Real-Time Kinematics
- **SA** Simulated Annealing
- **SAR** Synthetic Aperture Radar
- **SLAM** Simultaneous Localization and Mapping
- **TD-PD** Time-Difference Phase-Difference
- **Tag** RFID target
- **UAV** Unmanned Aerial Vehicle
- **UHF** Ultra-High Frequency
- **WSN** Wireless Sensor Network

List of Symbols

- ϕ : RFID phase
- λ : Carrier wavelength
- V_p : Velocity of longitudinal (compression) seismic wave
- V_s : Velocity of transverse (shear) seismic wave
- c : Light velocity
- f : Carrier wave frequency
- x, y, z : Cartesian coordinates
- **CC** : seismic cross-correlation coefficient
- **cm, m** : centimeters, meters
- **dV/V** : relative seismic velocity change
- **ms, s** miliseconds, seconds

Remerciements

Je tiens tout d'abord à remercier les membres du jury et notamment les rapporteur.ices, d'avoir accepté de se pencher sur mon travail. Merci donc à Cécile et à Jordi, merci à Etienne, Michel et Yvan.

Merci à mes encadrants Eric, Laurent et Mathieu, qui m'ont soutenu et supporté durant ce périple. Vous m'avez souvent mis face à moi-même et j'ai beaucoup appris à vos côtés. Merci de m'avoir fait confiance et de m'avoir donné les moyens d'avancer, dans mes directions de recherche ou mes déplacements géographiques. Merci particulièrement à Mathieu, qui m'a aiguillé de nombreuses fois et sans qui ce travail n'aurait pu aller si loin.

Merci à Olivier, avec qui j'ai collaboré durant une bonne partie de la thèse, et qui m'a permis de faire un beau voyage. Nos réunions mathématiques et matinales resteront un souvenir tout particulier de mon quotidien de doctorant. Merci à Ludovic pour tes propositions pertinentes, qui ont mené à l'encadrement d'un stage. Merci à Morgane, pour ton implication durant tes quelques mois à ISTerre. Merci à Gregory et Antoine qui m'ont aidé à élargir la portée interprétative de mes données.

Un remerciement tout particulier au service Gestion d'ISTerre, et notamment à Delphine, qui m'a toujours aidé à partir en mission malgré les difficultés administratives et les montagnes de facture.

Merci au service des ingénieur.es d'ISTerre, vous qui m'avez tant aidé à travers mes pérégrinations techniques. Merci à Ildut, Benjamin, Guilhem pour votre aide pratique et toujours enthousiaste.

Merci aux collègues doctorant.es d'ISTerre, je me souviendrai longtemps de ces années passées avec vous. Merci à Bene, Naomi, Tristan, Audrey, Shan, Leo, Pauline, et les autres.

Merci au collectif Faut-Il-Continuer, et à Laurent, à Lucien, à Olivier. Vous ne vous reconnaitrez peut-être pas dans ce manuscrit, mais vous m'avez aidé à tenir bon en incarnant mon engagement militant jusque dans le travail.

Merci à Marlène, tu m'as devancé de quelques mois et j'ai pris note de ta volonté de me tirer dans

la "bonne" direction, c'est à dire la plus difficile. Merci à Lise, partenaire académique si lointaine et pourtant si proche !

Merci Nogat, merci la Cagette, vous rendez ma vie plus belle.

Merci à Maria, tu es la "chercheuse très intelligente" qui m'a montré qu'on pouvait être beaucoup d'autres choses aussi.

Merci à Marion. Tu avais raison sur beaucoup de choses et notamment sur ma thèse !

Merci à Maman et à Marie pour votre positivité à toute épreuve, vous êtes mes phares dans la nuit.

Merci à Pacha, qui est finalement le seul être vivant à m'avoir suivi au quotidien, du début à la fin de ce travail.

Aerial picture of l'Harmalière landslide. In the background, the Matheysine region and Taillefer mountain range.

Chapter 1

Introduction

1.1 Landslides : a general presentation

Landslides, risk and environmental change

Landslides have been a growing concern for society in the last three decades [Wu et al., 2015]. In the context of global warming [Pörtner et al., 2022], developing urbanization and deforestation [Cui et al., 2019], the impact of landslides on human societies is constantly increasing [Gariano and Guzzetti, 2016, Haque et al., 2019]. Landslide hazard is sensitive to both human activity and climate change, especially in mountainous regions [Huggel et al., 2012]. The Alpine region already suffers from accelerated temperature increase, strong seasonal shifts, higher extremes in temperature and precipitation, as well as a strong decrease of snow cover [Gobiet et al., 2014]. These changes are expected to intensify with time [Beniston et al., 2018]. Consequently, it is expected that natural hazards will affect more populated and less prepared regions in the coming years [Calvello et al., 2016, Schneiderbauer et al., 2021].

In the last decade, more than 40 fatal landslides per year and 4000 death casualties were reported worldwide [Froude and Petley, 2018], as shown in Figure 1.1. For Europe specifically, more than 10 fatal landslides per year with tens of death casualties were reported [Haque et al., 2016].
The various drivers impacting landslide activity worldwide do not indicate a clear and simple trend, i.e. climate change does not simply increase the number of landslides. Nonetheless, the uncertain climate

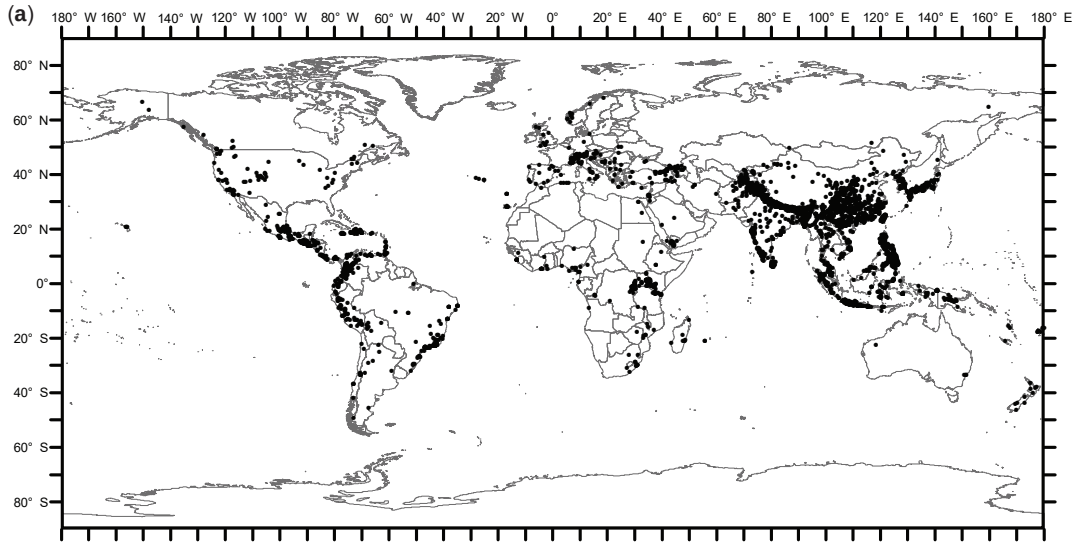

FIGURE 1.1 From [Froude and Petley, 2018] : Global non-seismically triggered fatal landslide occurrence between 2004 and 2016.

impact on ground stability and its coupling with human-induced factors make landslides a pressing issue in terms of research, monitoring, early warning, susceptibility mapping and risk management [Gariano and Guzzetti, 2016, Dai et al., 2002].

Throughout this manuscript, a selection of images referring to landslides and their effect will be shown, in order to provide a visual experience of the objects at stake.

General informations on landslides

The term landslide encompasses a variety of complex geomorphological phenomena, from instantaneous mudflows to year-long slow creeping. It can be broadly defined as the downward and outward movement of slope-forming material [Causes, 2001]. A wide variety of deformation mechanisms exist, as initially classified by [Varnes, 1978] and refined by [Hungr et al., 2014]. The majority of landslides are triggered by external causes, either natural or linked to human activity, although this distinction becomes quite blurry in the context of major human-caused climate disruption. The main landslide triggers are rainfall [Segoni et al., 2018], be it sudden or accumulated, and earthquakes [Havenith et al., 2003]. Concerning rainfall, the soil water intake acts on unstable blocks through diverse mechanisms, such as increasing block buoyancy, downward hydraulic pushing, fluidization of material, loss of suction

forces, and external or internal erosion. The main human triggers usually correspond to a change in soil material properties : deforestation removes tree root uptake and evapotranspiration, water management and construction can load or drain the ground, mining and quarrying or road construction can weaken the slope.

As landslide velocities and volumes can vary by multiple orders of magnitude, the range of their impacts vary as well [Turner, 2018]. Large human fatalities are usually due to very fast or extremely fast landslides, whereas buildings on very slow-moving landslides can remain in use for decades. Apart from the damage directly attributed to the landslide, indirect losses are also a major contribution : these include notably travel detours, disruption of the local economy, and environmental impacts. In 2015, the Chambon landslide triggered in a steep valley with a major road link [Dubois et al., 2016], connecting the village of La Grave to Grenoble (Isère, French Alps). For about a year, the village was isolated from the other part of the valley. As the local economy mostly relied on tourism, and the other access routes depended on the accessibility of the Lautaret mountain pass, this landslide deeply disrupted the local communities, even though no loss of life occured.

Slow-moving clayey Landslides

Clayey landslides tend to exhibit a complex behavior, generally advancing at a relatively slow rate (m/year) with sudden dramatic acceleration (m/day) with complex triggering mechanisms [Fiolleau et al., 2021, Lacroix et al., 2020]. The role of water in this context is often dominant, notably through the water table level, the instantaneous and accumulated precipitation, and the water infiltration properties of the ground. The exceptional sensitivity of clay to water content also plays a major role in the long-term degradation of the landslide cohesion : the shrink-swell seasonal cycles tend to both create dense fissure networks that strongly impact water infiltration, and propagate cracks that weaken the material. As shown by [Schulz et al., 2018], clay swelling can also increase the resistance to movement by applying pressure along the landslide's lateral boundaries. At present the water-induced landslide complex phenomena are still under investigation.

A simple model explaining mechanical failure in landslides was provided by the Coulomb-Terzaghi criterion [Terzaghi, 1950], linking resistance to shear failure, material cohesive sress and pore-water pressure. An increase of pore-water pressure, induced by the presence of water (from water table or precipitation), would lead to a decreased effective stress, lowering the frictional resistance of the

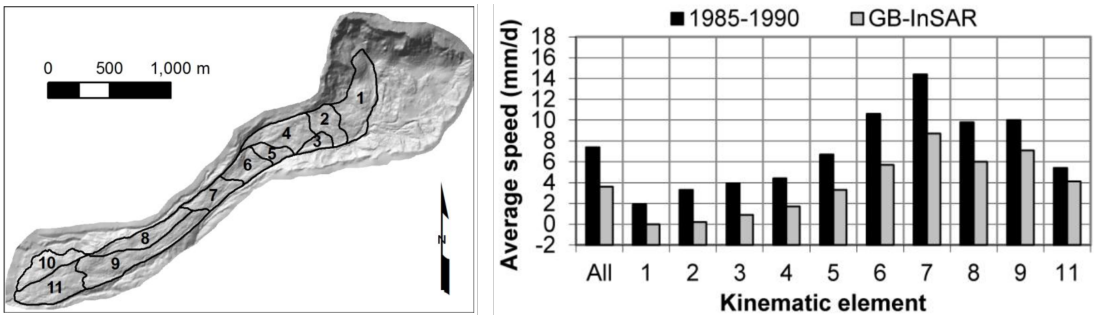

FIGURE 1.2 (Left) Aerial view of the Slumgullion landslide (Colorado, USA) and the identified kinematic elements. (Right) Average speed for every kinematic element for two different time periods, in 1985-1990 and 2012. Modified from [Schulz et al., 2012].

material and triggering movement. While this behavior is generally verified, several other factors constrain the triggering of landslide movements, such as hydro-geological characteristics [Matsuura et al., 2008], weathering, dynamic loading or past sliding history. More obvious triggers exist such as seismic activity, river incision, or human impact.

The high sensitivity to water is partly explained by the clays' microstructure : the clay particles naturally organize in heterogeneous and fragile structures [Gylland et al., 2013], with a stability partly dependent on the water pore pressure [Bogaard et al., 2007]. This delicate microstructure is very sensitive to the hydro-mechanical environment, and quickly collapses under constraint [Schäbitz et al., 2018]. Depending on the conditions, the clay particles organize in different ways, that translate in different rheological properties. In sensitive or "quick" clays, the soil can change from firm ground to an almost liquid mass when set in movement. [Carrière et al., 2018] studied the geophysical parameters of clay samples (notably from Harmalière) at the solid-fluid transition. Under high shear stress and water content, the seismic shear wave velocity V_s (linked to the materials bulk modulus and rigidity) shows a strong decrease, associated to sample fluidiziation. This non-linear relationship between water content and mechanical properties of clay, explains the unpredictable behavior of quick-clay landslides.

On a macroscopic scale, the dynamics of clayey landslides often show segments with coherent movements. In [Schulz et al., 2012] various "kinematic elements" were identified on the Slumgullion landslide (Colorado, USA), each showing a specific behavior varying in time. As shown in Figure 1.2, the velocity mapping of these elements provides precious insights on the landslides' internal structure and its evolution in time. Notably the differential velocities of kinematic elements informs on the long-term tendencies of the landslide, and can illustrate inner mechanisms linked to the hydro-geological

environment.

The Harmalière landslide (introduced below) also features a succession of segments with different mechanisms [Fiolleau et al., 2020] : the upper part is a compound earthslide with velocities of about 1m/year, which evolves in the lower part into an earthflow and a mudflow [Bièvre et al., 2011].

Presentation of the Harmalière landslide

Presentation extracted from [Charléty et al., 2022b] (Chapter 4). The present work mainly investigates the Harmalière landslide, a Southern France deep-seated clayey landslide. It is located in the Trièves area about 50 km south of Grenoble in the western Prealps. Trièves appears as a sedimentary plateau eroded by the Drac river; the plateau is formed by Quaternary varved clays and alluvial material deposited in a glacially dammed lake during the Würm period [G., 1973]. Quaternary sediments also include silts, sometimes with a morainic cover, and rest on either interglacial Riss-Würm period glaciofluvial materials (gravels and sands) or on the underlying Jurassic carbonate bedrock. The thickness of the clay deposits can vary from 0 to a maximum of 200 m [Jongmans et al., 2009]. The landslide is southeast oriented, 400 m wide at the top, narrowing to 150 m at the toe. It develops from an altitude of 735 m (above see level), down to the Monteynard Lake (480 m), over a distance of about 1.5 km. It was abruptly activated in 1981 and has remained active ever since, with new peaks of activity in 2016 and 2017. The slow moving landslide shows regressive behaviour, the headscarp retreating at an average velocity of 1 m/year, with very strong variations from year-to-year (including almost a decade of rest). The central body of the landslide is moving at velocities ranging from cm/year to m/year, with possible dramatic acceleration phases (m/day). A variety of research subjects are currently investigated in connection with it. In the recent years, [Fiolleau et al., 2019] exploited UAV-LiDAR imagery to monitor surface deformation as well as to characterize the soil type ; multi-method investigation, notably seismic and hydrology was performed [Fiolleau et al., 2021] ; and [Lacroix et al., 2018] used optical satellite data to detect precursory landslide motion.

As stated above, landslide behavior is dictated by a complex set of environmental parameters, such as hydro-geological context, water intake, or the nature of the constituting clay material. Understanding general and specific landslide behavior is an important matter when trying to mitigate their impact on society. Next section will discuss various ways of landslide mitigation.

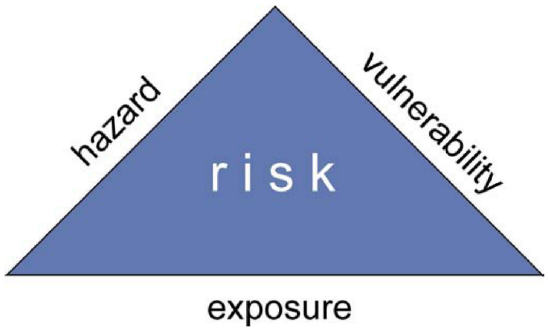

FIGURE 1.3 The "risk triangle" : risk is quantified as as product of hazard, vulnerability and exposure. From [Schneiderbauer and Ehrlich, 2004].

Landslide mitigation

Landslide mitigation describes any human activity aimed at reducing the negative impacts of landslides. Landslides are often considered in a Quantitative Risk Assessment frame [Van Ryzin, 1980], which calls for a definition of risk itself but also hazard, vulnerability and exposure. A hazard defines a possible adverse event such as a landslide, exposure is the number of people (or buildings) in the hazard area, and vulnerability is the degree of susceptibility of the actor exposed to that hazard. The latter is related to the preparedness of the local communities, generally linked to the level of poverty in the area [Schneiderbauer and Ehrlich, 2004]. By definition the risk of landslide takes place in anthropized areas, where the hazardous event can cause harm to society. Risk is defined as the product of hazard, vulnerability and exposure, in other words it is the probability of an adverse event times the consequences if the event occurs (see Figure 1.3). [Lacasse et al., 2009] published a detailed study of the diverse landslide mitigation techniques, ranging from political aspects of hazard zonation to construction work for slope consolidation. Considering the "risk triangle", mitigation can target one of the three pillars constituting risk, for example :

- reducing exposure : converting the areas at risk to a use which is less vulnerable. This includes inhabitants relocation.
- reducing hazard : slope stabilization work to prevent dramatic slope failure.
- reducing vulnerability : reinforcing building structures, or setting up early warning systems.

As the risk associated to landslides is changing on account of climate and land use, there is a need for permanent recognition of risk. Beyond risk communication and awareness, more pro-active mea-

sures exist such as structural slope-stabilization, land-use planning and landslide early-warning systems (LEWS). The latter can serve multiple purposes : risk assessment and management, regional warning, or understanding the behavior of the monitored object. Depending on the objective, different types of measurements will be of use in LEWS : direct displacement measurement is most adequate for estimating the instability in real-time, but indirect measurements such as pore pressure or precipitation level can provide information on the inner mechanisms of the instability. In that regard, multi-method monitoring is a comprehensive approach, taking advantage of all possible sources [Casagli et al., 2023, Fall et al., 2006]. Next section will cover Landslide Early Warning Systems.

Landslide Early Warning Systems

In this section, the practical aspects that are covered originate from interviews with the Geolithe staff, as well as a literature review.

Early warning approaches are non destructive methods, based on real-time measurement of quantities correlated to landslide triggering. The most direct measurement is of course the surface displacement, but many other parameters can be monitored in order to define critical thresholds for landslide activity. Practically, the first and basic measurement installed on a monitored landslide are precipitation measurements [Segoni et al., 2018], piezo-meters [V Ramesh and Vasudevan, 2012] and tilt-meters [García et al., 2010]. Indeed the hydro-geological context is crucial, and notably the relationship between rainfall, water table level and soil destructuration [Fall et al., 2006].

Early Warning Systems can be considered locally, regarding a specific object such as a landslide or an unstable rock column, but they can also span wider areas such as a valley or a region. The scales, parameters and heuristics involved are not the same in either case. Typically, local LEWS consist of more robust, mechanical or threshold-based alert systems, while regional systems are based on more empirical, meteorological, geophysical and model-based systems [Stähli et al., 2015]. Moreover, as stated by [Intrieri et al., 2012], early warning system are not only a sum of monitoring systems, "[they] also involve other aspects such as the identification of risk scenarios, emergency plans, societal considerations, [and] public awareness". [Guzzetti et al., 2020] propose a critical review of landslide early-warning fundamental assumptions, and concrete implementations notably at the regional-scale, which consist of several *in-situ* sensors distributed over the land. They highlight the difficulty of evaluating the performance of LEWS or comparing different systems. Finally they encourage the

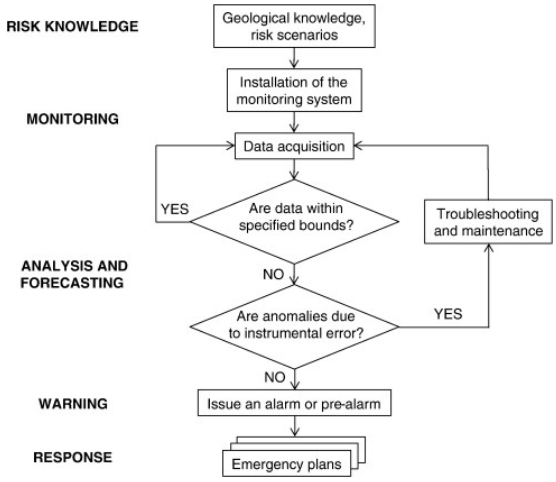

FIGURE 1.4 Generic flowchart describing the steps for implementing early warning systems. Extracted from [Intrieri et al., 2012]

LEWS community to propose shared standards for design, implementation, and management of LEWS systems. Conversely [Intrieri et al., 2012] describe the step-by-step implementation of a local EWS. They emphasize that having a lot of sensors is not enough. Understanding the unstable object, pointing the critical parameters to monitor, setting up a robust network and warning the local communities are critical aspects which should not be neglected. They even note that working on the local population's risk awareness, is by far the most cost-effective means of reducing the risk. They propose a generic flowchart of early-warning systems, which is reproduced in Figure 1.4.

In the past years, efforts have been deployed notably in the development of novel and innovative landslide monitoring techniques. [Pecoraro et al., 2019] reviews local or *in situ* landslide early-warning systems (Lo-LEWS) operational all around the world. The choice of the system is dictated by the following parameters : covered landslide area, corresponding volume, and main landslide cause. The observables are classified in three main groups : deformation (including displacement, velocity and acoustic emission), groundwater (pore pressure, water table level) and trigger (rainfall, snowmelt).

In the last decade, seismic ambient noise interferometry has also been applied to landslide early warning. This method relies on the reconstruction of the medium's transfer function by cross-correlating the noise measured passively from two sensors. Introduced by [Lobkis and Weaver, 2001] using ultrasonic waves, the method developed on a wide range of earth-sciences applications [Larose et al., 2015] including landslide monitoring [Le Breton et al., 2021]. The apparent surface wave velocity varia-

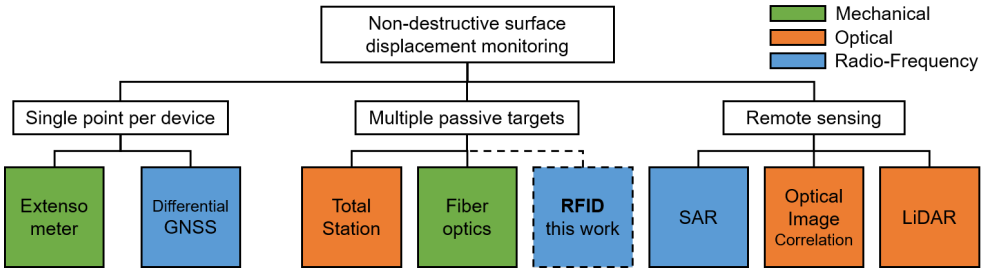

FIGURE 1.5 Classification of LEWS, depending on the sensing scheme. Modified from [Le Breton, 2019].

tion, also called dV/V, attracted much attention since it was identified as a precursor for landslide failure [Mainsant et al., 2012] notably correlated to clay fluidization [Carrière et al., 2018]. Relative seismic velocity is now used as a landslide monitoring tool, providing access to subsurface information, and complementing the punctual measurements provided by tilt-meters.

As the current work focuses on displacement monitoring, deformation measuring devices will be presented in more detail. A classification of displacement-monitoring devices is proposed in Figure 1.5. Below is a non-exhaustive list of the main types, illustrated by Figure 1.6.

- Wire extensometer : used to measure the displacement between two objects, usually through a coiled cable which displacement is monitored internally [Corominas et al., 2000]. This has the advantage of providing absolute displacement between two points, on a year-long period of time. On the other hand, the wire can be damaged or displaced by snow accumulation, hence biasing the measurement. These sensors are fit for short-range monitoring (short cable), as long-range cables pose practical issues.
- Tacheometer (or Total Station) : exploits line-of-sight optical measurements using a laser beam, to triangulate reflectors and provide their position in a local frame. Nowadays most monitoring stations are automatized, and provide millimeter precision [Dematteis et al., 2022]. The main limitation of this method is the need for a free line-of-sight path between device and reflector, and the risk of mixing targets together as they are not identified.
- GPS : provides absolute positioning using satellite communication, even in foggy or inaccessible environments. The need for reducing the cost of such monitoring techniques has been emphasized in recent works [Lacroix et al., 2020]. Even low-cost GPS solutions such as in [Benoit et al., 2015] still cost a few k€ per point, with the need of individual power for every point. Moreover, GPS

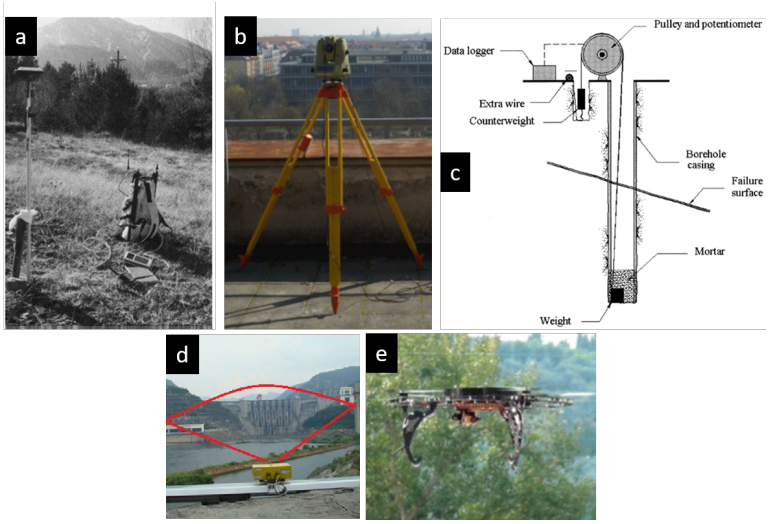

FIGURE 1.6 Illustration of the list of Landslide Early Warning Systems (non-exhaustive) : (a) Global Positioning System (from [Gili et al., 2000]), (b) tacheometer (from [Wasmeier, 2003]), (c) wire extensometer (from [Corominas et al., 2000]), (d) ground-based remote sensing monitoring a dam (from [Qiu et al., 2020]), and (e) airborne remote sensing device mounted on an Unmanned Aerial Vehicle (from [Casagli et al., 2017]).

do not necessarily provide high accuracy in mountains or on densely vegetated slopes.

- Ground-based remote sensing : These in-situ methods provide both real-time and long-term displacement monitoring, and allow for other measurements such as hydrological parameters and precipitation [Chae et al., 2017]. Just like other radio-frequency techniques, its main downside is the cost of the device.

- Airborne remote sensing : techniques such as Interferometric Synthetic Aperture Radar (InSAR) are widely used for landslide detection and monitoring [Carlà et al., 2019, Dini et al., 2020]. As they rely on satellite availability, the sampling frequency is limited to several days, hence real-time monitoring is impossible. Moreover, optical imagery does not work in the presence of clouds. On the other hand, they allow for much wider area monitoring. On a more local scale, the use of Unmanned Aerial Vehicles (UAV) is well adapted to characterization of active sites where *in-situ* methods cannot be employed.

In order to improve reactivity and sensor complementarity, Landslide Early Warning Systems are often included in Wireless Sensor Networks (WSN). Connected to a central station or server, these sensor networks allow for centralized data monitoring, enabling coordination at a regional scale [Ramesh,

2014]. On more local scales they provide dense information with numerous multi-measurement stations including inclinometers, soil moisture sensors [Jeong et al., 2019], rain gauges or seismic sensors [Ramesh, 2009]. Although GPS and extensometers can belong to WSNs, the term usually depicts more autonomous and local sensors [Dini et al., 2021]. WSNs are easily deployed in harsh environments and provide real-time monitoring with minimum maintenance. These systems are often limited by the battery lifetime of the active sensors, as well as a relatively high cost.

From a practical point of view, there are two main objectives for LEWS that do not imply the same level of system robustness : forecasting the event, and securing the endangered stakes.

Diagnose, Forecast Understanding the object in order to predict failure conditions is part of the early warning approach [Intrieri et al., 2012]. To that end both surface and volume measurements are used to auscultate the landslide, as well as precipitation measurements. Typically, the cyclical behaviour of the object is studied, in relation to weather (rainfall), soil rigidity (ambient noise), and surface displacement (GPS). Photogrammetry or radar [Stumpf et al., 2015] offer wide area coverage for surface displacement, and UAV is also a promising solution for frequent and low-cost auscultation. Generally, the diagnosis and forecasting provides insights on the landslide mechanisms on a day-to-year time scale.

Secure the stakes In order to safely secure and warn against a hazard, low-complexity and local independent loops are necessary, with minute-to-second reaction time. Securing cannot rely on intricate data processing methods nor on permanent network connection. Usually, simple methods with clear threshold detection are employed : tilt-meter, extenso-meters, automatized tacheometry, or radar interferometry [Carrel et al.,]. Local micro-seismic monitoring is also possible, to detect rockfalls and mudflows [Feng et al., 2021]. In real-time securing scenarios, the methods must be working in all-weather, night and day. Hence optical methods cannot be used due to weather sensitivity, nor GPS monitoring which does not provide real-time information.

Taking into consideration the above remarks, it must be added that the choice of the LEWS solution is heavily site-dependent [Pecoraro et al., 2019]. There is a great variety of hazards, in different geometries and context : monitoring a hazard in the Reunion Island is very different from doing so in

the French Alps.

In landslide displacement monitoring, the critical aspects that stand out are the cost and maintenance of the monitoring devices, their sampling frequency and their ability to measure in all meteorological conditions. In this context, Radio-Frequency Identification (RFID) is foreseen as a promising solution, notably by ISTerre and Géolithe. Indeed, RFID yields dense measurements both in space and time, is weather-robust and available even in snowy or vegetated scenarios, with no need for line-of-sight, and with year-long durability. Next section will introduce RFID, and its application to landslide monitoring in more detail.

1.2 RFID and landslide monitoring

Some material of this section is based on the author's contribution to [Le Breton et al., 2022].

Radio Frequency Identification (RFID) is a wide-spread communication system, that enables to detect and identify a target (or tag) via a radio-frequency communication link. It is commonly used in logistics to identify goods in the supply chain [Tan and Sidhu, 2022] as a replacement of barcodes, in the healthcare sector to track objects or people [Abugabah et al., 2020], and in the general Internet of Things paradigm [Landaluce et al., 2020]. The Earth Science community has shown a growing interest for RFID over the recent years, notably for pebble tracking, unstable boulder monitoring, or soil moisture sensing [Le Breton et al., 2022]. This chapter will shortly cover a basic introduction to RFID, then the specific case of tag tracking and localization will be presented.

RFID basics

Radio-Frequencies (RF) constitute a portion of the large electromagnetic spectrum. RF is classified by the frequency of the electromagnetic wave, from 9 kHz to 3000 GHz. In this work, the concerned bandwidth is close to 865 MHz (communication protocol EPC Gen2, 2015), which corresponds to the domain of Ultra-High Frequencies (UHF). This frequency corresponds to a typical wavelength λ of 34 cm, linked to light velocity c in air :

$$\lambda = \frac{c}{f}$$

Any electromagnetic wave is characterized by two coupled oscillating fields, the electric and magnetic fields, described by the Maxwell equations [Fleisch, 2008]. When travelling through various media, these two fields will interact with the surrounding material. The polarization of the material and the resulting electromagnetic field will induce a retroactive modification of the wave propagation, depending on the dielectric permittivity and magnetic permeability of the medium [Fano, 2020]. In the case of outdoor RFID where most propagation occurs through air, water and snow, the permittivity ϵ is the main concern. Conversely, the interaction between RF wave and metallic structures is at the core of RFID communication. Indeed the design of RFID chips is mostly based on the geometry and material of the metallic chip [Cho et al., 2005], which impacts the tags range, directionality and sensitivity to surrounding material. Different categories exist amongst RFID, notably in the way they store their identifier and the electromagnetic communication used to interrogate them. We will herein focus on

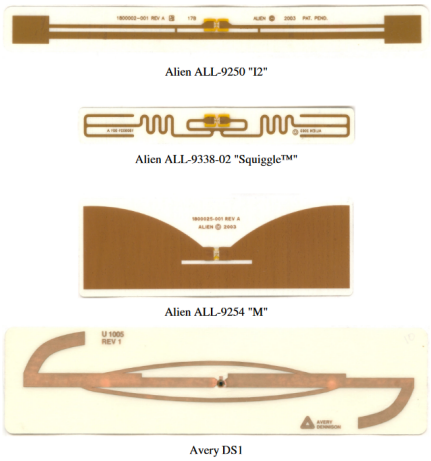

FIGURE 1.7 Example of passive UHF-RFID chips. Extracted from [Ramakrishnan and Deavours, 2006].

UHF backscattering microchip tags, although chipless tags exist, as well as tags relying on inductive coupling rather than backscattering [Chawla and Ha, 2007]. The main advantage of the latter is the ability to read tags at distances reaching tens of meters, which is necessary in a growing number of applications [Griffin and Durgin, 2009]. Another major advantage is the capacity to distinguish the response of individual tags amongst hundreds, thanks to anti-collision communication protocols [Klair et al., 2010]. Two main categories of tags exist : active and passive RFID, depending on the power sources of the tag. In active RFID, the battery-powered tag emits its own RF signal to an interrogator (or reader antenna). Passive RFID will be covered in more details below. Figure 1.7 shows examples of RFID chips in various shapes.

As any type of wave, RF waves can be reflected, refracted, diffracted, or absorbed and they suffer from propagation loss. Along with Maxwell's equations, this is at the basis of antenna theory [Huang, 2021]. The importance of these effects on RFID detection has been widely studied, notably by [Fletcher et al., 2005] and [Nikitin and Rao, 2008]. Fletcher measured the UHF wave transmission and reflection in the presence of a water layer, and concluded that reflection and interference play a much more important role than absorption in liquid materials. Nikitin covered major aspects concerning propagation and antennas, in particular the path loss effect related to ground reflection interference (or multipath), as well as specific considerations regarding passive battery-less RFID tags.

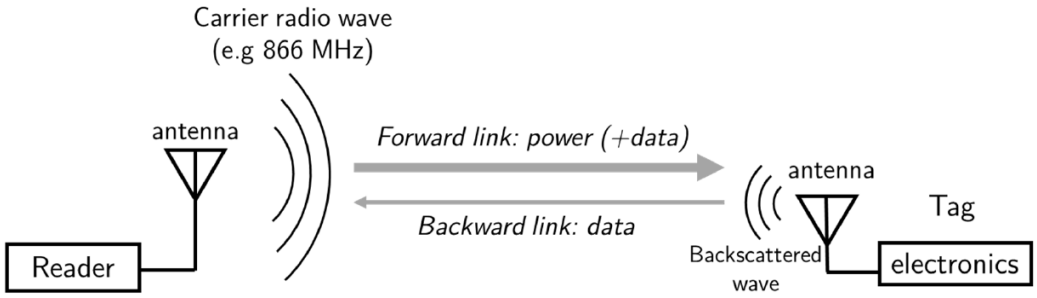

FIGURE 1.8 Schematic of the communication process between an RFID reader and a passive tag. From [Le Breton, 2019].

This work will focus on semi-passive RFID, based on battery-assisted backscatter communication : the RF wave emitted by the reader powers up the tag, which will respond with its identification number and potentially other sensor information, by modulating the back-scattered signal [Sorrells, 1998], with an increased backscattered power thanks to the battery. This reader-tag "handshake", depicted in Figure 1.8, also yields information concerning signal propagation, notably the Received Signal Strength Indicator (RSSI) and the Phase of Arrival (PoA) which are both of interest in the RFID-based monitoring applications. RSSI provides information about the signal amplitude, which decreases with travelling distance, but also in the presence of multipath interference or high-permittivity material. Phase is mostly driven by reader-tag distance, although it remains sensitive to the environment [Le Breton et al., 2017]. Due to its higher stability and overall better accuracy than RSSI, phase has been attracting interest in the field of RFID localization for the past years. A more detailed introduction on RFID phase localization, is presented in Chapter 4 [Charléty et al., 2022b].

RFID tag localization

Tags can be located in space, using their signal amplitude or the variations of phase delay. The simplest method is to detect a tag and conclude that it is nearby, within the detection range of the interrogator. The method has been used extensively to track the displacement of pebbles in rivers using low-frequency tags with sub-metric detection range [Cassel et al., 2017]. Nevertheless this technique has a spatial resolution that depends on the detection range, from several decimeters to meters. The localization of tags at longer distances uses UHF tags [Miesen et al., 2011b], and exploits the received

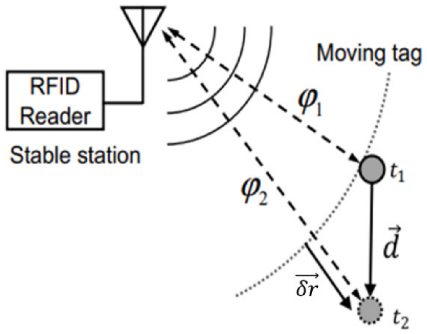

FIGURE 1.9 From [Nikitin et al., 2010]. Schematic view of the Phase Difference of Arrival (PDoA) approach. Equation 1.2 expresses relationship between phase and radial distance.

signal strength (RSSI) or the phase of arrival (PoA). Signal-strength-based methods have been initially introduced for tag localization [Griffin and Durgin, 2009,Ni et al., 2003], followed by phase-based methods which usually offer the best accuracy, reaching one centimeter or less [Scherhäufl et al., 2015,Zhou and Griffin, 2012]. In practice the phase-based methods show the best potential for observing ground displacements [Le Breton et al., 2019]. Backscattering communication used in passive RFID can easily measure the phase difference arrival because the reader transmits and receives the same carrier wave, compared to active RFID which uses two distinct RF front-ends on the tag and reader.

The phase of arrival in free space ϕ relates to the delay of propagation, and depends on the speed of light in the air c, the distance between the tag and the reader r , the carrier frequency f, and an offset ϕ_0 caused by the devices:

$$\phi = \frac{4\pi f}{c} r + \phi_0 \tag{1.1}$$

In practice, the phase of arrival measured by the reader is ambiguous, wrapped within $[0, \pi]$ or $[0, 2\pi]$ rad [Miesen et al., 2013], reducing its intrinsic value as a single measurement. However, the Phase Difference of Arrival $\delta\phi$ measured between two different phase readings ϕ_n is exploitable for relative localization [Nikitin et al., 2010]. It relates to the change in tag-reader radial distance δr that occurred between the two reading positions :

$$\delta\phi = \phi_2 - \phi_1 = -\frac{4\pi f}{c}\delta r \tag{1.2}$$

Where $\delta\phi$ represents the measured phases at different positions related to δr. Note that this equa-

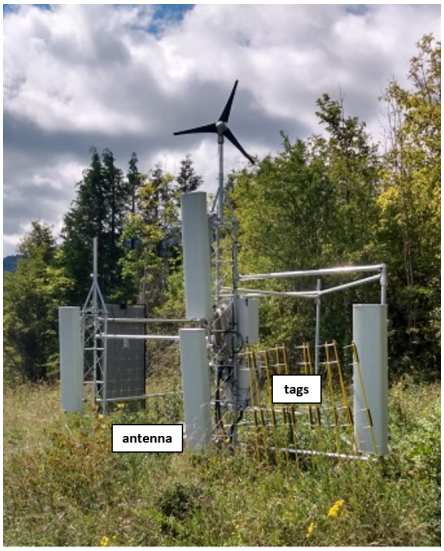

FIGURE 1.10 The RFID setup installed on the Harmalière landslide, with four antennas and about twenty tags. The tags (Confidex Survivor B) are placed by pairs on poles, fixed in the ground.

tion holds only for phase shifts smaller than the readers measurement ambiguity ($\pi/2$ or π). Simplest usage of this approach estimate 1D distance or displacement between a tag and a station antenna (see Fig. 1.9). Optionally it can locate the tag in 2D or 3D using multiple station antennas and trilateration [Scherhäufl et al., 2015], as in the Harmalière setup shown in Figure 1.10. The two main phase-based localization schemes exploit either the variation of the phase in time which is a relative localization technique, or the variation of phase with signal frequency which allows for absolute ranging. The latter shows less accuracy and seems not suited to track slow displacements [Le Breton, 2019, Le Breton et al., 2023b].

Using arrays of tags allows for estimating the tilt of the array relatively to the station antenna (by comparing the phase differences between tags). For reciprocity reasons, this approach also holds for arrays of antenna facing fixed tags [Scherhäufl et al., 2015]. The approaches mentioned previously allow for a centimeter-scale error for punctual measurements as well as month-long monitoring in outdoor conditions [Charléty et al., 2023a].

One of the main limitations of RFID phase localization is the phase wrapping ambiguity and the

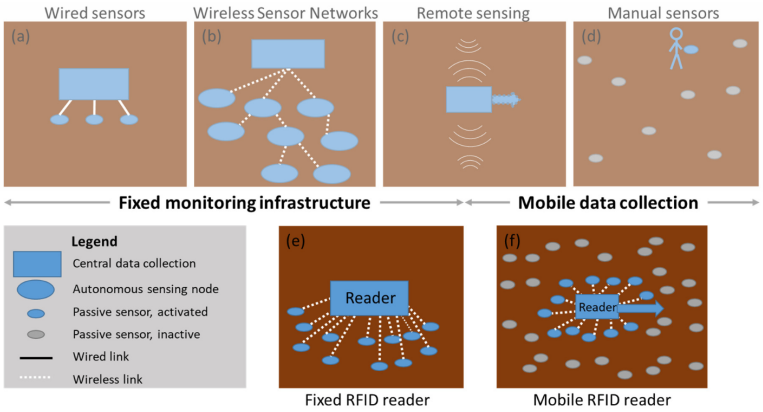

FIGURE 1.11 From [Le Breton et al., 2022]. Schematic description of data collection in geosciences. Blue squares represent an autonomous acquisition system, that stores data or communicates it to a remote server. (e) and (f) represent typical RFID schemes that are used in this work : a fixed reader system interrogating moving tags, or a mobile reader interrogating fixed tags.

influence of multipathing [Faseth et al., 2011, DiGiampaolo and Martinelli, 2020, Ma et al., 2018]. A way to reduce these effects is the Time of Flight method [Arnitz et al., 2010, Arthaber et al., 2015], which avoids ambiguity as the full-time shift is measured. It can also reduce the influence of multi-path when the time of first arrival is measured, and when a wide-band pulse is used. However such methods often require custom devices that are not on the market nor standardized. Nonetheless, RFID localization using standard commercial equipment has proven doable and is currently a flourishing research topic, offering a centimetric to decimetric spatial resolution. [Ma et al., 2017] notably proposed a breakthrough method for off-the-shelf narrow-band tag localization by emulating an ultra-wide bandwidth, computing time-of-flight in order to identify the line-of-sight and distances, and finally using multi-frequency phase measurements to localize tags with a centimeter accuracy.

To conclude, RFID localization is nowadays investigated in various fields of application and through several approaches. It shows great capability and adaptability both in indoor and outdoor environments, with multiple ways to bypass the current limitations. Landslide surface displacement monitoring has been demonstrated [Le Breton et al., 2019] with outdoor-conditions validation of phase measurements [Le Breton et al., 2017]. It yielded a centimeter accuracy with 1D measurements in long-term outdoor scenarios. From a LEWS point of view, we foresee RFID as a future securing method in closed-loop warning system. As shown in Figure 1.11, RFID enlarges the spectrum of data collection

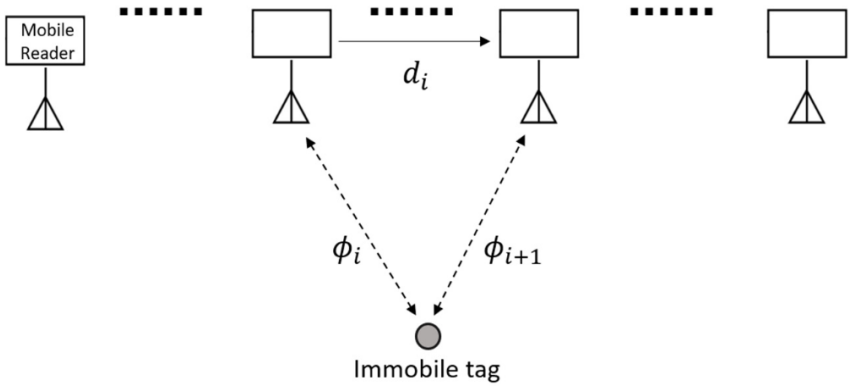

FIGURE 1.12 From [Le Breton et al., 2022]. Description of the Synthetic Aperture Radar approach with RFID. ϕ_i and ϕ_{i+1} represent two successive phase measurements.

approaches in geoscience. Next section will shortly describe another RFID localization approach, based on a moving antenna and fixed tags.

Synthetic Aperture Radar

The synthetic aperture radar (SAR) is another use of phase measurements, used typically for satellite or ground-based radars. It relies on the combination of multiple measurements from different antenna positions, to generate a virtually larger synthetic antenna. Interferometric Synthetic Aperture radar (InSAR) is widely used in earth sciences and specifically landslide mapping and monitoring [Lacroix et al., 2018], due to its high sensitivity to vertical displacement. The ability of Unmaned Aerial Vehicle (UAV) to carry embedded measurement systems, allows for a broader implementation of SAR approaches [Buffi et al., 2018]. Applied to RFID, SAR implies moving one or more reader antennas along known trajectories [Bernardini et al., 2020b, Wu et al., 2019], often carried by a mobile robot or UAV. The typical scenario illustrated in Figures 1.12 and 1.13, consists in flying the UAV equipped with RFID reader, above the landslide where tags are deployed. After RFID-SAR measurement, inversion is performed, i.e. the minimization of a cost function comparing real phase measurements and simulated measurements computed from the antenna trajectory and a probable tag position [Buffi et al., 2018]. Optimization algorithms like particle swarms or Kalman filters are often used to decrease the computational cost of such calculations [Bernardini et al., 2020b, Gareis et al., 2020]. SAR localization has proven to reach a centimeter-scale precision. However, the shape of the reader trajectory has a strong impact on the localization accuracy, and has to be chosen carefully to locate the tag in all investigated

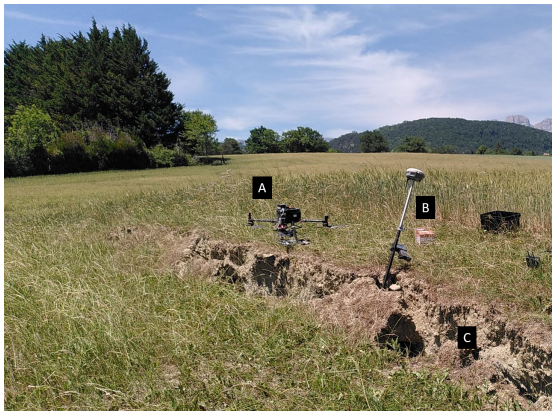

FIGURE 1.13 Illustrative image taken during an UAV-RFID acquisition on the Harmalière landslide. (A) drone equipped with RFID reader, (B) GPS-RTK rover station and (C) landslide scarp.

dimensions [Bernardini et al., 2020a]. Consequently every measurement campaign requires reference measurements, from Global Positionning Systems (GPS) for example (see Figure 1.13). More details on SAR-RFID are provided in Chapter 6.

Next section is dedicated to connecting RFID tracking to GPS tracking methods. Indeed it has appeared to the authors that, although RFID localization is a unique subject with specific stakes and challenges, many similarities exist with GPS systems.

Optimal filtering and GPS

In the Internet of Things era, the profusion of smart-sensors is generating a vast quantity of information. This "deluge of unclean sensor data" [Krishnamurthi et al., 2020] poses new challenges in terms of processing, such as data denoising, outlier detection, missing data imputation and data aggregation. Analysing big-data flows to produce meaning is now a challenge that relies heavily on machine-learning, data fusion and signal processing tools to perform relevant decision-making and interpretation [Alam et al., 2017]. This also applies to Earth Science data [Lunga and Dias, 2022] where the multitude of remote sensing approaches and geophysical measurements [Zhang, 2010] allow for finer and finer characterization of monitored objects [Hibert et al., 2012]. In the field of data fusion and processing, Kalman filters occupy a key place as they combine general knowledge about the observed system and various (noisy) sensor information [Crowley and Demazeau, 1993]. Kalman filters are hence widely

used both in the field of RFID [Motroni et al., 2021] and landslide monitoring [Cai et al., 2022].

In regard to bayesian approaches for state estimation based on noisy measurements, RFID phase processing shows similarities with GPS processing algorithms. Although RFID and real-time satellite positioning have specificities related to hardware and scales of measurement, the present work has shown remarkable similarities between both systems, in terms of data processing and challenges. Both RFID positioning and GPS are based on phase measurement inversion [Langley et al., 2017], at least partially, and the difficulties related to phase unwrapping are shared in the two domains. Notably, Real-Time Kinematics (RTK) is particularly focused on carrier phase issues. In GPS-RTK positioning, the measurement scheme is directed towards estimating the number of wavelengths separating the receiver and all the satellites in view. To that end, differential measurements are performed to compare measurements from a base and a moving rover [Feng et al., 2008] (see Figure 1.13). When this fixed-integer solution is found (number of wavelengths), the accuracy is at its highest, within the wavelength ambiguity which is typically 20 cm. The value of the phase informs on the position of the receiver inside this 20 cm window, up to sub-centimetric precision in ideal cases. Usually, this fixed solution is not obtained instantaneously and a floating solution is provided : the number of wavelengths is not precisely estimated, and the precision is generally about 20 cm. In order to maintain a fixed-solution even during displacement, GPS data can be coupled to inertial measurements through fusion algorithms such as Kalman Filters. This approach allows to maintain a fixed-integer solution even with high rover speeds and accelerations. Similar approaches have been used in RFID [Zhou and Griffin, 2018], combining complementary ranging methods using data fusion. This composite ranging allowed for sub-centimeter absolute localization, as well as a reduction of multipath impacts.

Although based on more developed and complex approaches, GPS data processing resembles RFID phase processing by many aspects. The concept of GPS position dilution of precision [Banerjee et al., 1997] related to system geometry is very translatable to RFID localization, as is developed in Chapter 4. The use of reference points to enhance individual measurements is used in RFID as well [Jin et al., 2006]. Phase ambiguity resolution is a crucial step in both methods, facing the critical issue of phase decoherence. The related phenomena, such as multipath interference and shading, or phase jumps due to high accelerations, encourage to use the GPS processing methods in RFID phase processing [Kos

et al., 2010, Lazaro et al., 2009].

The UAV-RFID approach on its side [Parr et al., 2013], is even more comparable to satellite-based ranging as the antenna is following a known trajectory. The knowledge of the moving antenna position is used for predicting the next measured phase based on the knowledge of previous information. This is applied notably in InSAR phase measurement, where the successive satellite orbital positions have to be estimated with high precision in order to resolve centimeter-level phase ambiguities [Shirzaei and Walter, 2011].

1.3 Structure of the manuscript

The above introductory Chapter was aimed at setting the scene of the present doctoral work. By describing landslides and LEWS, we showed how RFID outdoor tracking can improve landslide hazard monitoring. The principles of RFID were explained as well as the phase-based tracking methods used for displacement monitoring. The potential for RFID tracking under UAV's was shortly explained, along with the connections between GPS systems and RFID localization. These two domains share similar aspects of signal processing and optimal filtering, which are key elements in all the data-driven methods showed herein.

Next chapters will describe my research work regarding RFID landslide monitoring. Signal processing approaches are first presented in Chapter 2 and 3. Chapter 4 covers 2D landslide monitoring, and Chapter 5 exploits RFID results for unraveling landslide kinematics. Finally, Chapter 6 describes the SAR-RFID localization experiments.

The Monteynard lake from the top of the Harmalière landslide. Four seasons from left to right and top to bottom : spring, summer, autumn and winter.

Chapter 2

RFID landslide monitoring : long-term outdoor signal processing and phase unwrapping

This chapter was published in IEEE Journal of Radio Frequency Identification (Volume: 7) [Charléty et al., 2022a].

Authors : Arthur Charléty, Mathieu Le Breton, Laurent Baillet, Eric Larose.

2.1 Introduction

Radio-Frequency Identification (RFID) has recently drawn the attention of the Earth Sciences community [Breton et al., 2021], notably for environment remote sensing at low cost. RFID tag localization has been a growing research topic in the past years [Nikitin et al., 2010], with multiple localization methods [Scherhäufl et al., 2015,Rohmat Rose et al., 2020] and applications [Vojtech et al., 2015,Buffi et al., 2014]. Apart from solely localization-based monitoring, RFID technology is foreseen as a promising way to perform low-cost and spatially diverse environmental sensing. Notably in outdoors scenarios, long-term RFID monitoring (months to years) in complex environments that generate high measurement

noise, is a current and growing research field. In diverse application domains such as infrastructure monitoring [Strangfeld et al., 2019], agricultural monitoring [Deng et al., 2020, Rayhana et al., 2021], social insects behavior monitoring [Nunes-Silva et al., 2019], ice formation [Wagih and Shi, 2021] or snow depth monitoring [Le Breton et al., 2023b], and of course earth surface processes monitoring [Breton et al., 2021], robust and synthetic RFID information is needed to ensure optimal data continuity and exploitation. Although not focused on displacement monitoring, these applications would clearly benefit from a data availability increase.

In most scientific works regarding RFID localization, the presented datasets show smooth and correctly-sampled measurements that correspond to laboratory-controled experiments [Tzitzis et al., 2019, DiGiampaolo and Martinelli, 2020, Tzitzis et al., 2021, Chatzistefanou et al., 2021, Yang et al., 2021, Li et al., 2009, Zeng et al., 2019, Peng et al., 2021, Tripicchio et al., 2022]. In real-life scenarios such as retail environments [Nikitin et al., 2010] or outdoor landslide monitoring [Charléty et al., 2022b, Breton et al., 2021], the acquired data is inevitably noisier and intermittent. At the same time, RFID generally yields abundant and redundant data that can enhance the data from each tag [Qiu et al., 2017, Zhang et al., 2017]. In many cases the objects are monitored by multiple tags, multiple antennas or through multiple carrier frequencies, with the objective of forming tag arrays or yielding more robust data. Moreover as the size of the instrumented sites grow, the overall number of tags also increase, with a growing need for synthesizing redundant data and making it more exploitable. This data redundancy poses new data processing challenges regarding the reliability of RFID-phase information, especially with regards to phase ambiguity and unwrapping which are crucial elements when recovering tag displacements.

With the combined perspectives of long-term RFID measurements and of data redundancy exploitation, RFID landslide monitoring experiments represent unique candidates for providing long-term, real-life noisy and redundant signals. This method has already proven its centimeter-scale accuracy through multiple works [Le Breton et al., 2019, Charléty et al., 2022b]. The feedback offered by the past years of monitoring is of great use for understanding real-application scenarios, especially concerning the process of phase unwrapping.

Several techniques already exist for landslide displacement monitoring, such as optical approaches [Jaboyedoff et al., 2012], radar interferometry [Monserrat et al., 2014] or GPS [Gili et al., 2000]. Despite their simplicity, optical methods are sensitive to obstruction by obstacles, fog or heavy rain. Radiofrequency methods are much less sensitive to these obstacles, but they require more complex and expensive systems, and usually rely on active sensors. Compared to these classical methods, RFID monitoring offers a lower-cost alternative in terms of installation and maintenance, because the tags are passive. Additionally, RFID provides dense measurements both in space and time with easy reflector identification, that are little sensitive to obstruction (vegetation, snow cover, fog). This is a great advantage in an all-season long-term monitoring approach.

Among various RFID localization schemes, phase-based methods have shown the best accuracy in outdoor scenarios [Le Breton et al., 2017], with centimeter precision. In particular we will use the Time-Domain Phase-Difference (TD-PD) method [Nikitin et al., 2010] for its robustness and high precision. The unwrapping process is a central subject in the phase-based RFID localization literature [Tzitzis et al., 2019, Wu et al., 2019]. It is the main step that allows phase data to be interpreted in terms of displacements. The main difficulty that unwrapping poses is that of phase ambiguity, which has been thoroughly investigated in the past years [Sarkka et al., 2011a, Scherhäufl et al., 2014]. Recently, several works have focused on exploiting implicit information or bayesian filters in order to improve phase unwrapping even in noisy and multipath-rich environments [Giannelos et al., 2021, Hoffman and Bester, 2020, Tao et al., 2020, Li et al., 2021]. But the challenge of data availability and quality in itself is seldom tackled, being a more *applied* challenge with a strong dependency on the context. It is nonetheless of utmost importance, as in our experience the main causes of unwrapping errors are data gaps and data noise : an absence of data during a rapid tag displacement will very likely generate unwrapping errors, and a very noisy signal will have high chances of being incorrectly unwrapped.

In this paper, which is an extended version of [Charléty et al., 2022a], we propose to discuss the recent advances in RFID-phase monitoring as applied to soil surface displacement monitoring using RFID, with data and experience from the past years on several instrumented landslides. We present new algorithms and data processing methods aimed at solving issues concerning RFID data availability and quality. We also propose a discussion on the various ways RFID phase unwrapping

can be performed in a diversity of contexts, especially when handling real-life noisy and partial phase data. After presenting the RFID tracking method as applied on different monitored landslides (2.2), we discuss the different data availability challenges that the method poses as well as the software solutions implemented in order to overcome those challenges (2.3). The signal processing methods used to obtain robust synthetic measurements are presented, using data fusion and processing algorithms (2.4). At every processing step, a short literature review of similar methods is proposed. Most of the presented approaches exploit the high redundancy of RFID data, allowed by the important number of tags that are deployed and by the multiple channels through which the tags are read. The concept of a guide for unwrapping phase data is presented. To our knowledge, this work is the first attempt at applying the concept of an unwrapping guide to RFID data. The data availability improvements obtained for phase data, are quantified and discussed for all instrumented sites (2.5). These methods, here applied to outdoor long-term monitoring, can be of great use in the implementation of long-term monitoring scenarios in challenging environments.

2.2 Equipment and localization method

RFID Instrumentation

This study will discuss the RFID data from 4 landslides, that all share the same measurement scheme. Several RFID tags (Confidex Survivor) are continuously read by an acquisition system consisting of an interrogator (Impinj SR420 or equivalent) and at least two reader antennas. A micro-computer and a modem ensure continuous data acquisition and transfer.

The measurement rate depends on the site and the available power : autonomous stations relying on solar/wind energy use a lower acquisition frequency than power-grid-connected stations. On average the available data gives a minimum of 100 phase readings per day and per tag. Both the Phase of Arrival (PoA) and the Received Signal Strength (RSSI) are measured, in order to estimate the quality of the received phase signal. All measurements are performed at four different carrier frequencies : 865.7, 866.9, 866.9 and 867.5 MHz in Europe (ETSI EN 302 208).

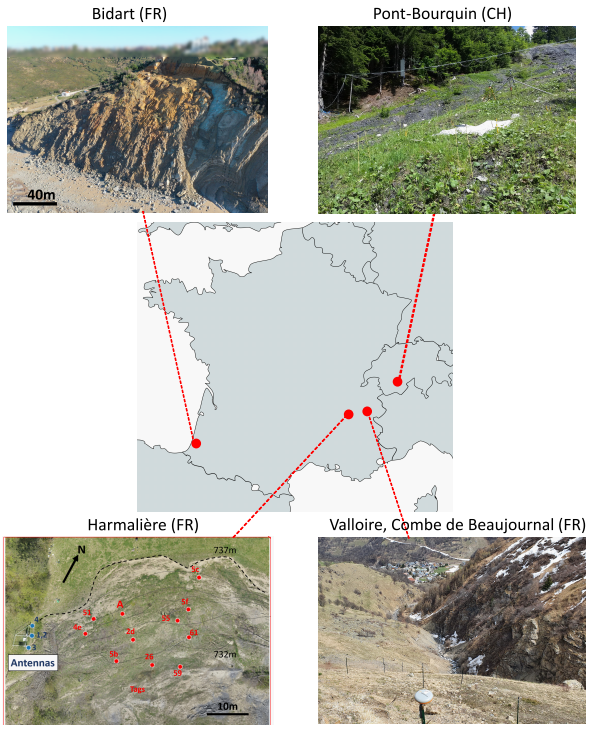

FIGURE 2.1 Map of the RFID-instrumented sites across France and Switzerland, represented as red dots.

Monitored sites

The four instrumented sites are located across France and Switzerland (see Fig. 2.1). All sites grossly correspond to the typical setup presented in Figure 2.2, with a group of tags facing the antennas, placed by pairs on fiber glass or metal stakes at an elevation of approximately 1m above ground. For generalization purposes, these stakes can be simply considered as tagged objects. The reader antennas are positioned on stable ground close to the landslide, usually at a higher altitude than the tags. The tagged objects are placed on (slowly) moving ground. The maximum read range for the system is about 50-60 m.

The main objective of our approach is to monitor each tagged object (metallic stake equipped of two tags) individually through time. In reality, a landslide usually consists of one or multiple blocks. Tagged objects on the same block behave the same way, and hence present coherent displacements.

In all the presented cases, the landslide general movement is known *a priori* and the antennas are

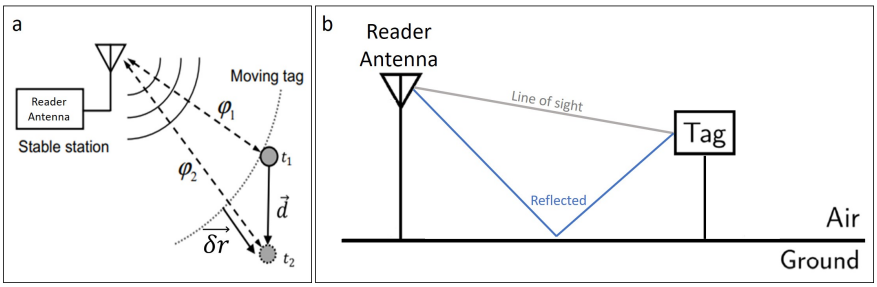

FIGURE 2.2 Schematic principle of all RFID monitoring sites. (a) The principle of relative TD-PD localization : the phase variation between two measurements is linked to the projected radial distance variation (see Equation 2.1). (b) The tags are placed on the monitored objects (metallic or fiberglass stakes) about 1m above ground, which can generate multipath interference between the line of sight (grey) and reflected (blue) paths.

positioned optimally with regard to this movement. Except from l'Harmalière (see below), the 1D radial distance measured by each antenna roughly corresponds to the landslide movement.

- The Bidart landslide is located on the south-east coast of France. It has been under observation by the Bureau de recherches géologiques et minières (BRGM) and Geolithe, for more than 3 years. The RFID setup was installed in 2022 and consists of 2 reader antennas and about 30 tags. Reference measurements are frequently acquired using GPS and tacheometry. This coastal landslide has shown strong activity since its recent instrumentation, with displacement rates up to 5 meters per year.
- The Harmalière landslide (Sinard, France) is located near Grenoble in the western Pre-Alps, and is a slow moving landslide currently active and investigated by many research projects [Fiolleau et al., 2021]. The RFID setup, installed in 2020 [Charléty et al., 2022b], consists of 4 reader antennas and 32 tags spread in a 30 m by 30 m investigated zone. Tacheometry reference measurements are frequently performed. The Harmalière landslide RFID experiment was built in a different way than the other RFID sites, with an open multi-antenna setup oriented towards 2D and 3D monitoring [Charléty et al., 2022b]. Although this installation was built
- The Pont-Bourquin landslide is located in the western Pre-Alps near Lausanne in Switzerland. The setup installed in 2017 [Le Breton et al., 2019], consists of 2 reader antennas and 20 tags. An extensometer located near the installation is used as a 1D-reference for surface displacement (see 2.4). This reference is notably unavailable during winter due to snow cover on the extensometer wire. This site shows the longest monitoring time, with several data features to interpret : strong

acceleration phases, snow creep, harsh weather conditions.

- The Valloire landslide is located in a steep valley (Beaujournal) above the city of Valloire (France). In the case of exceptional rainfall events this landslide threatens to feed debris flow and endanger the city. The site was instrumented in 2019, and features RFID as well as photogrammetry and seismic monitoring instrumentation. The Valloire landslide has not shown measurable activity since its RFID instrumentation.It has nonetheless been an important source of data to test and improve the methods herein presented.

The sites presented above cover a wide variety of topographies, weather conditions and environmental risk, highlighting the versatility of the presented technique.

Amongst other factors, data gaps are often related to the power supply failure of RFID stations. Most stations need to be electrically autonomous due to their location, and this implies the use of in-situ power sources such as wind turbines or solar panels. For such systems where energy is a scarce resource, a compromise is necessary between measurement sampling frequency (which depletes the batteries) and data continuity over time (which requires available battery power). As of now, the measurement scheme has been adapted depending on the power source of each station : the autonomous station in Harmalière was set to a lower sampling frequency (2 minutes of measurement over 20 minutes : 10% duty cycle) than the Pont-Bourquin station (100% duty cycle), which is connected to the Swiss power grid. On an energy-saving setup such as l'Harmalière, the strategy could be further adapted by increasing the sampling frequency when increasing displacements are detected.

RFID Relative localization scheme

A schematic of the TD-PD localization method is presented in Figure 2.2a. TD-PD is a relative ranging technique based on a phase variation $\delta\phi = \phi_2 - \phi_1$ between two measurements of the same moving point, at different points in time. $\delta\phi$ is related to the radial distance variation $\delta r = r_2 - r_1$ between the tag and the reader antenna, by the following equation:

$$\delta r = -\frac{c}{4\pi f}\delta\phi \tag{2.1}$$

where f is the frequency of the electromagnetic wave (in Europe 865.7, 866.9, 866.9 or 867.5 MHz) and c is the speed of light in the propagation medium. It is important to note that Eq.(2.1) is only valid for displacements smaller than $\lambda/4 \approx 8$ cm between two phase measurements because of phase ambiguity. This ambiguity which should ideally be $\lambda/2$, is further reduced due to the reader setup used. In the present case the $\lambda/4$ condition is generally fulfilled as the incremental displacements are small compared to the wavelength (usually less than 1 cm between two successive acquisitions). In the case where the phase is correctly unwrapped, Eq.(2.1) is valid for any unwrapped phase variation. Phase unwrapping is a crucial step in recovering true tag displacement, as we will see below (2.4).

2.3 Challenges for RFID data availability

This section will present and discuss the main challenges encountered with the RFID-phase monitoring technique, in terms of data availability, quality and processing.

Increase data availability with multiple antennas and tags

The availability of data at all times is crucial in the context of early warning systems, especially at the start of a soil surface movement. The quality of the signal is usually worse during strong precipitation events, when the risk of landslide activation is generally higher [Guzzetti et al., 2007]. Additionally, the experience showed that RFID phase availability is heavily dependent on tag/antenna orientation and multipath shading. In order to increase data availability and redundancy, most sites were equipped with two tags per monitored object, at a short distance from one another (about 20-50 cm). Additionally, multiple antennas often read the same tag, providing more data redundancy. This alone can mitigate several problems : the multipath-induced artifacts can be detected and compensated, and the data availability is higher which can further increase the continuity of the displacement measurement (see section 2.4).

In all the following sections, data availability does not refer to the sheer amount of acquired data. Rather, it reflects the fact that at any point in time, there is an available data point for every monitored object.

Avoid unwrapping errors due to data gaps

Data continuity over long periods of time is a key challenge in order to correctly estimate tag displacement. In the TD-PD relative localization scheme, the maximum readable displacement between two measurements is limited to a few centimeters. When a data gap coincides with a rapid displacement higher than the unwrapping ambiguity, this localization scheme alone does not allow true displacement estimation. Such data gaps can be caused by various phenomena such as hardware failures, multipath shading, or harsh environmental conditions.

The unwrapping ambiguity is geometrically dependent on the angle between tag displacement and antenna-to-tag radial vector. In the Harmalière landslide [Charléty et al., 2022b], a multi-antenna setup is described with a localization approach taking advantage of the Angle-of-Arrival concepts [Azzouzi et al., 2011], although the distance between the antennas is much higher than the required distance for an Angle-Of-Arrival solution. The system aperture is parallel to the tags displacements, which increases the size of the acceptable ambiguity. In such setups, tags can be tracked even when incremental displacements are higher than 8 cm. The downside of such methods is the higher sensitivity of the localization to a phase measurement error. In order to take advantage of both approaches (Angle-of-Arrival and 1D phase unwrapping), new methods could be developed in the future.

The next section will describe the various data processing methods that were implemented in order to improve the quality of the RFID data, with an objective of decreasing the number of unwrapping errors and obtaining more synthetic results.

2.4 Data fusion and processing

The data continuity and availability issues are mitigated via a signal processing data-fusion approach, notably by taking advantage of the information redundancy provided by a dense network of tags, as well as the multi-frequency and multi-antenna measurements. All these processes will be illustrated by following the data improvement of one specific tagged object (stake) monitored with two tags, in the Pont-Bourquin landslide (see Figures 2.4 to 2.6). The overall data workflow is summarized in Figure 2.3, with simple schematics summarizing the various approaches. At every step of the process, a short and specific literature review will allow to put the proposed method into perspective.

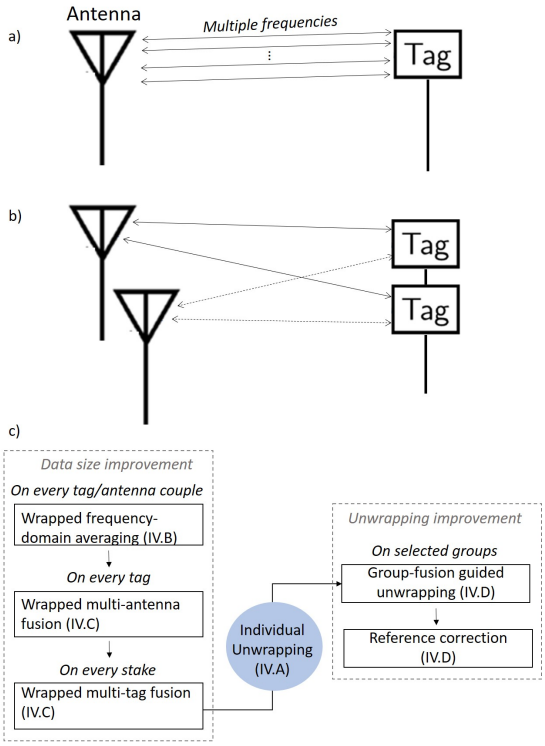

FIGURE 2.3 (a) Schematic of the multi-frequency approach : every tag-antenna couple yields four phase measurement series. (b) Schematic of the multi-tag and multi-antenna approaches. (c) Flowchart for data fusion with all approaches : multi-frequency (MF), multi-antenna (MA), multi-tag (MT) and guided unwrapping.

Complex rolling window unwrapping

As explained above, phase unwrapping is a very important step in phase processing. Many approaches have been presented in the recent literature to tackle different phase unwrapping situations.

In general, the unwrapping methods based on bayesian state-space models are fit for scenarios where either the antennas or tags move along inertia-dominated paths : flying or sliding object, conveyor belt, unmaned-aerial vehicle equipped with a reader. [Sarkka et al., 2011a] resolves the phase ambiguity using an Extended Kalman Filter in a multi-antenna, moving-tag scenario with an accuracy of 0.02 m. [Giannelos et al., 2021] implements a particle filtering approach with a moving antenna to resolve distance ambiguity, taking into account the potential multipath-rich environments. They reach accuracies around the 0.2 m scale.

Other more deterministic unwrapping methods also exist, often considering the problem as an optimization problem with the objective of linearizing it. Such methods are often sensitive to other reference measurements, such as reference tags or known antenna/tag trajectory. [Tzitzis et al., 2019] presents an unwrapping algorithm based on the segmentation of the signal in coherent measurement sets. Each segment is first unwrapped with a simple algorithm, then the whole set is unwrapped by minimizing a cost function based on the antenna positions. Predicted accuracy is below 0.1 m.

In order to overcome the errors on reference measurement or due to strong multipath interference, machine learning has also been applied. Notably the tag/antenna displacement trajectories can be taken into account in training the algorithms. For example, [Li et al., 2021] performs unwrapping using a random forest algorithm and [Li et al., 2022] proposes a deep learning approach, reaching accuracies between 0.5 m and 0.1 m.

In the present scenario, a noise-robust unwrapping algorithm is required, because of the highly variable RFID data quality in an outdoor scenario. We implement an unwrapping algorithm based on a complex smoothing approach. Let ϕ be the measured phase series (from 0 to 2π) and z_ϕ be the corresponding complex angle series :

$$z_\phi = e^{i\phi}$$

We decompose this complex series in a low-frequency smoothed z_s component and a high-frequency $\tilde{z}$

component, in order to avoid discontinuities :

$$z_\phi = z_s + \tilde{z}$$

z_s is obtained by average smoothing over a variable time window, usually ten minutes. After this separation, both components are reverted back to real angle values as ϕ_s and $\tilde{\phi}$.

$$\phi_s = Arg(z_s) \qquad \tilde{\phi} = Arg(\tilde{z})$$

We then unwrap the smoothed component ϕ_s using a classical unwrapping algorithm [PyU,] to obtain the smoothed unwrapped phase ϕ_s^U, to which we add the noise to get the final unwrapped measurement ϕ^U:

$$\phi^U = \phi_s^U + \tilde{\phi}$$

Note that by construction the noisy component $\tilde{\phi}$ is considered smaller than π and does not need unwrapping. This algorithm, although quite simple in its implementation, greatly reduces the influence of data noise on the unwrapping process. Nonetheless it does not reduce the quantity of information, as the high-frequency component is not lost in the process : the smoothing is simply used as a temporary step to increase the unwrapping reliability.

Frequency-domain measurement averaging (MF)

In this section we describe a method for combining the RFID measurements at different frequencies, in one synthetic phase measurement. This approach is compatible with frequency-hopping [Li et al., 2009], and brings the same advantages in terms of mitigating multipath interference [Yang et al., 2021]. It would benefit even more from a larger frequency band than the ETSI band.

Let us first recall the relationship between phase, radial distance r and carrier frequency [Nikitin et al., 2010], related to the Frequency-Difference Phase-Difference (FD-PD) ranging method :

$$r = \frac{c}{4\pi} \frac{d\phi}{df} \tag{2.2}$$

If we hypothesize that the total distance r presents negligible relative variations over the considered time, we can convert all phase measurements to the same equivalent frequency. More precisely, that is

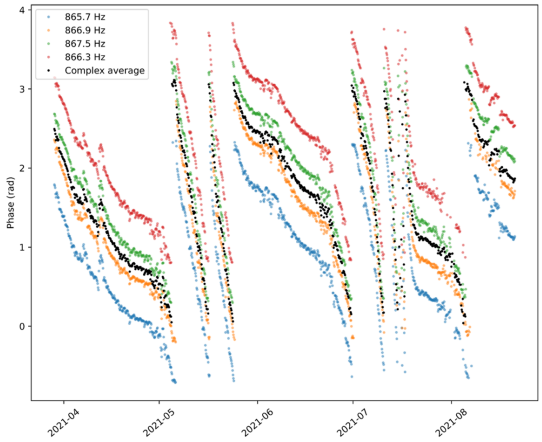

FIGURE 2.4 Phase measurements at four different frequencies and the corresponding fused measurement (black dots) for one tag on the Pont-Bourquin landslide. The initial sampling frequency is one measurement per minute for every tag and antenna couple, but the presented data was resampled for readability. The total displacement is about 60 cm. Each frequency channel was offset to increase readability. The best mono-frequency series shows 26111 data points, and the multi-frequency averaging series shows 49055 points.

when the displacement measured by the TD-PD method (Eq. 2.1) is small compared to the absolute distance estimated via the FD-PD method (Eq. 2.2).

$$\delta r_{TD-PD} << r_{FD-PD}$$

This approximation is accurate in the case of slow moving landslides, where total radial distances are generally higher than 10 m and their monthly variations on the 0.1 m scale. In this situation, the phase difference $\Delta\phi_f$ between a phase series measured at frequency f, and an equivalent frequency f_{eq} (usually set as 865.7 MHz) can be computed :

$$\Delta\phi_f = r(f - f_{eq})\frac{4\pi}{c} \tag{2.3}$$

Using Eq.(2.3) all phase series ϕ_f measured at various frequencies f, are superimposed by subtracting the value $\Delta\phi_f$. This subtraction yields $n_{freq} = 4$ superimposed data series (illustrated in Fig.2.4) that are fused in a frequency-synthetic complex phase series z_{MF} (MF stands for multi-frequency) :

$$z_{MF} = \frac{1}{n_{freq}} \sum_{f=1}^{n_{freq}} e^{i(\phi_f - \Delta\phi_f)}$$

Computing the complex argument of z_{MF} provides a wrapped-phase synthetic measurement. The final wrapped multi-frequency phase fusion ϕ_{MF} result is computed by :

$$\phi_{MF} = Arg(z_{MF})$$

The fusion approach presented above exploits frequency diversity and allows to concatenate all available frequency channels in one measurement, increasing the size of exploitable data by reducing the data gaps, as shown in Figure 2.4. The method described is valid for other frequency channels, making it usable with any UHF-RFID standard bandwidth. In fact any frequency channel can be used, provided the computed $\Delta\phi_f$ is smaller than π.
In the next section, we propose methods to further merge multi-channel data, using multi-tag and multi-antenna data series.

Combining data across space : multiple tags (MT) and reader antennas (MA)

Another common way of enhancing RFID data is to exploit the spatial diversity of reader antennas and tags. Historically, a major step in tag localization was brought by the k-Nearest-Neighbors approach using reference tags [Ni et al., 2003] and received signal strength measurements. A bayesian filter was added [Xu et al., 2017] to increase the accuracy from 1 m to about 0.1 m. Using phase measurements, [Siachalou et al., 2019] exploits the difference between tags in order to locate them among a grid of already-localized tags. With a flying antenna without onboard accurate positioning they obtain a tag localization accuracy around 0.2 m. [Li et al., 2019b] exploits the data from different tags in order to perform tag-to-tag relative localization, and obtains a 0.3 m accuracy. Double-tag arrays are also used by [Zeng et al., 2019] in order to solve phase ambiguity and improve localization accuracy up to about 0.2 m.

Antenna spatial diversity is usually exploited in order to perform 2D or 3D localization, with a generally better accuracy when performed in the plane [Tripicchio et al., 2022,Charléty et al., 2022b]. [Yang et al., 2021] exploits the data from multiple antennas for phase or distance disambiguation, with a 2D localization accuracy below 10 cm. Phase-based relative 2D localization was also performed using multiple antennas for landslide monitoring [Charléty et al., 2022b]. [Megalou et al., 2022] uses a trained

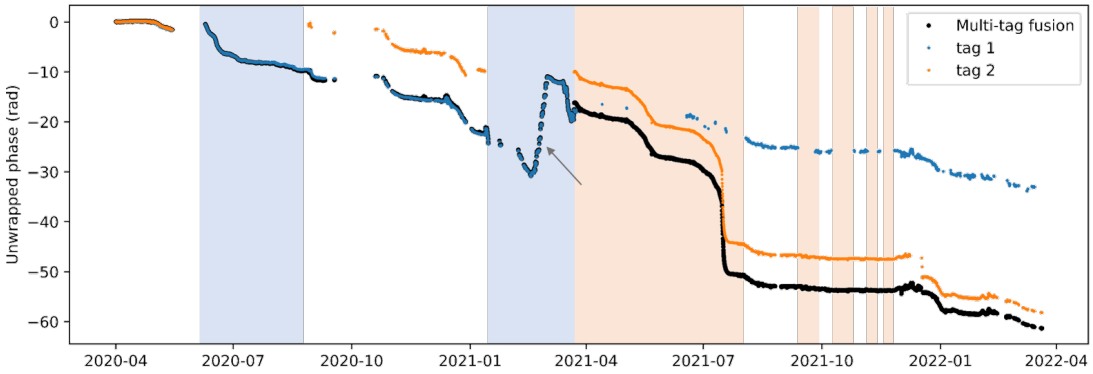

FIGURE 2.5 Unwrapped data series from the two tags on the same object, and the fused measurement (Pont-Bourquin landslide). The background colors highlight the fact that only one tag is read. The steep phase variation (grey arrow) in February 2021 corresponds to snow melt, generating a backwards displacement due to the bending elasticity of the fiber poles holding the tags.

neural network to perform multi-antenna phase difference hyperbolic positioning, without any given initial position, reaching an accuracy of 0.5 m. [Tripicchio et al., 2022] performs hyperbolic localization based on multi-antenna measurements, in an indoors Synthetic Aperture Radar approach and with an accuracy close to the centimeter scale. [Tzitzis et al., 2021] uses a multi-antenna Synthetic Aperture approach with a Particle Swarm Optimization algorithm [Bernardini et al., 2020b], reaching a 3D localization accuracy below 0.2 m.

In the present scenario, we exploit both the multi-tag and multi-antenna approaches in order to obtain better unwrapping results. When two antennas (reader or tag) are close together, the measured phase variations are generally similar and can be superimposed after complex mean subtraction. We thus consider that tags on the same object behave similarly, and that all antennas will measure the same phase variation for each specific tag. Note that we do not aim to use the spatial diversity of tags and antennas to localize objects in 2D or 3D space. Rather we intend to maximize 1D data continuity. The 3D case was investigated elsewhere [Charléty et al., 2022b].

Figure 2.5 shows such correspondence for multi-tag fusion, with a difference between the superimposed phases (from tags on the same object) never exceeding 1 rad ; this difference is most likely a combination of multipath interference and small position difference between the two tags. Fusing several partial vectors in complex space, gives rise to an improved synthetic measurement ϕ_{fused}. After

the multi-frequency averaging operations are performed, the complex phase series from all tags on the same object are fused by complex superposition and averaging. The fused phase is then unwrapped in order to recover the estimated displacement. If we define the unwrapping algorithm by U (as described in 2.4), the unwrapped phase ϕ^{unw}_{fused} is obtained using the wrapped fused phase ϕ_{fused} :

$$\phi^{unw}_{fused} = U(\phi_{fused})$$

This whole process tends to synthesize all available data from each tagged object, into one displacement indicator. The next section will present various approaches to obtain further information by exploiting the near environment.

Guided unwrapping

When individual data series are not dense enough to correctly unwrap the phase (such as in Figure 2.5), the unwrapping process can be guided using a reference. This reference can be an absolute measurement or a synthetic fusion vector.

The concept a guide for phase unwrapping already exists in 2D interferometry, where unwrapping is equally a crucial step prior to data analysis. For example, [Wang et al., 2011, Liu et al., 2019, Ajourlou et al., 2019] use a quality-guide to unwrap 2D interferograms. This method comes down to using high-quality unwrapped references to progressively unwrap the surroundings. The following methods apply roughly the same concept to the RFID phase data.

This guiding approach is obviously based on the common motion of multiple tagged objects, which is generally observed as the coherent landslide blocks are large. We use this coherence between different displacements, to better unwrap each and every phase data series. Hence the use of grouped-fusion, which is a loose generalization of the multi-tag approach.

Grouped fusion for individual unwrapping In the case of a data gap during a rapid displacement, simply taking data from each object is usually not enough to correctly unwrap the phase. In such situations, one possibility is to implement a fusion operation over a group of tagged objects sharing the same behavior. All measured phases from the group are merged to produce a synthetic guide containing more information than individual phase series. This guide can then help unwrap every individual tag. Let ϕ_t be the phase series from tag t, then the reference group fusion ϕ_{ref} is computed

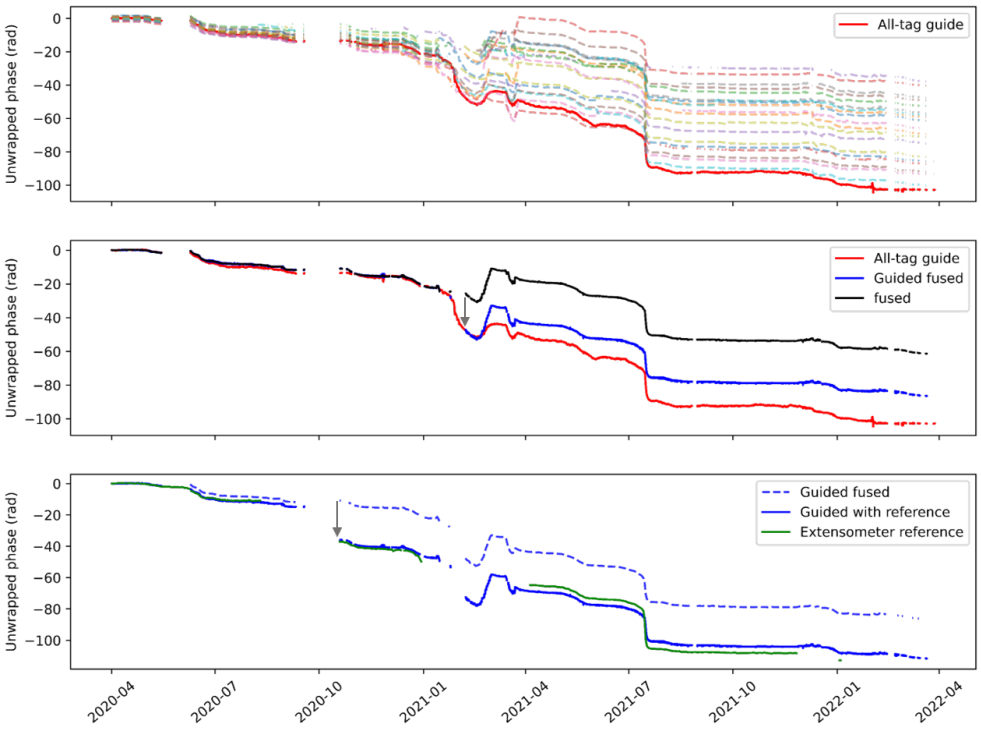

FIGURE 2.6 Example of guided unwrapping process for one tag on the Pont-Bourquin landslide. (Top) Computation of a group-guide based on all phase data. The group is shown in red, and each dotted color line represents a tagged object. (Middle) Guided unwrapping of the single multi-tag data ("fused" in black, see Figure 2.5) using the group guide in red. The result is in blue. (Bottom) Guided unwrapping using the extensometer data (in green) ; the dotted blue line corresponds to the full blue line in the middle plot ; the final result is again in full blue. The main unwrapping corrections are highlighted by a grey arrow.

from the rate of change $\dot{\phi}_t$ using a simple average operation :

$$\dot{\phi}_{ref} = \frac{1}{n_t} \sum_{t=0}^{n_t} \dot{\phi}_t \tag{2.4}$$

With n_t the number of tags in a group, and $\dot{\phi}_{ref}$ the group fusion time derivative. Equation 2.4 essentially computes an average velocity of the group of tags. ϕ_{ref} is then obtained by time integration, and presents more features than every individual phase series (see Figure 2.6). This reference is then used as a guide to unwrap the individual series. Using the unwrapping algorithm U as discussed above, guided unwrapping corresponds to the following operation :

$$\phi_g = U(\phi_m - \phi_{ref}) + \phi_{ref} \tag{2.5}$$

Where ϕ_m is the measured phase and ϕ_g the unwrapped phase guided by ϕ_{ref}. The main idea behind this operation is that if the measured phase presents an unwrapping error, it will be highlighted and corrected by subtraction of the reference which supposedly shows a better phase continuity. Although the unwrapping is not guided by a high-quality reference but rather by a synthetic group reference, this methods yields coherent results even when the reference and the phase series do not fit perfectly (see Figure 2.6).

Absolute reference measurement When at least one absolute reference measurement (tacheometry, GPS or extensometer) is available on a field, it is used to help unwrap the whole dataset. This was the case in the Pont-Bourquin landslide where absolute displacement data was available (although scarce in time) via an extensometer. If the reference data is continuous in time, guided unwrapping can be performed. If not, discrete corrections are performed either automatically or by manually correcting the phase. This approach allows keeping track of long-term displacements, as shown in Figure 2.6.

Putting things together

All the previously mentioned approaches are integrated in a hierarchical data processing workflow described in Figure 2.3. The four frequency channels are first fused together to obtain a synthetic phase series for each tag-antenna couple. Next, the data from all antennas are fused for every tag, in order to have one synthetic measurement for each tag. Then the tags from each object are fused together, and the resulting series are unwrapped by complex unwrapping. Finally, on sites where it is applicable, guided unwrapping is performed using an absolute reference, a group-fusion guide or both.

2.5 Results and discussion

In this section we present and discuss the results obtained after the phase processing. First we describe the specific data quality and unwrapping improvements concerning one specific tag, then we present and discuss the general improvements brought on all instrumented landslides. Finally we come back to the other monitoring challenges on landslides, and the implemented solutions.

Processing step	Pont-Bourquin	Valloire	Harmalière	Bidart
MF (%)	13 (26)	23 (48)	2 (10)	2 (13)
MA (%)	4 (19)	2 (30)	3 (18)	3 (31)
MT (%)	15 (58)	2 (22)	2 (18)	-
ALL (%)	38 (129)	28 (64)	3 (50)	5 (37)

TABLE 2.1 Overall available data size improvement for each processing layer compared to the previous one, for the four RFID-instrumented sites. The increase is given in percentage of average data availability increase, with the maximum value in parenthesis. Pont-Bourquin landslide : 5-year monitoring period and 20 tags. Valloire landslide : 1-year period and 15 tags (MT and MA are cumulated because of their low value). Harmalière : 2-year period and 15 tags. Bidart : 10-month period and 40 tags (no multi-tag available).

Data availability improvement and unwrapping for one tag

Figure 2.4 presents each frequency channel for one tag, and the corresponding MF phase series during a 5-month period. Over this small time period, the MF fusion yields an available and continuous data size 80% larger than the mono-frequency phase series : the best individual series shows 26111 data points, and the MF fusion shows 49055.

The unwrapped multi-tag (MT) fusion results are shown in Figure 2.5 for the same tagged object, with several corrected unwrapping errors compared to the two individual data series. The noisy variations occurring around March 2021 correspond to snow melt before the metallic stakes were installed, and an unwrapping error (June 2020) remains in the final data. We note that the partially-observed displacement originating from snow creep (February-March 2021), generates unwrapping errors : the total displacement after winter is lower than before winter. This issue is partially solved by using the group-guide on all tags from the Pont-Bourquin landslide : on Figure 2.6, we see that the whole winter period is covered by the guide, and yields a more coherent displacement after snow creep. Furthermore, the extensometer reference measurements allow for long-term phase correction, notably after September 2020 where displacements occurred but where not measured.

General improvement on all sites

Table 2.1 shows the general data availability improvement of the fusion approach on all 4 sites. Each layer increases the exploitable data by the given percentage. We can note that for Valloire and Pont-

Unwrapping errors	Before	After
Bidart Group 1	11	3
Bidart Group 2	7	3

TABLE 2.2 Number of cumulative detected unwrapping errors with and without applying the grouped fusion, for two different groups of tags in the Bidart landslide.

Bourquin, the multi-frequency (MF) fusion brings a high data availability increase above 10%. Comparatively the multi-antenna (MA) fusion does not bring a significant improvement on average, with some individual exceptions especially on Valloire (+30%) and in Bidart (+31%).
In total the three processing layers (ALL) increase the data availability by 3 to 38% depending on the site, with peaks for specific objects reaching more than 50% data availability increase.

As seen in Figure 2.6, the use of a synthetic guide allows a better signal reconstruction by reducing the number of unwrapping errors. In the Bidart landslide, the data was split in two distinct groups of tags with coherent behaviour, in order to unwrap the data using a group-guide. The improvements obtained by this method are quantified in Table 2.2, compared to the previous processing which consisted of individual mono-frequency series unwrapping. This shows a strong reduction of detected cumulative unwrapping errors. These errors are computed based on reference measurements over a 2 months period with displacements of about 1m, from March to May 2022.

Figure 2.7 compares the data availability improvement to the normalized read rate for each and every tag. The normalized read rate is computed by comparing the number of measurements to the ideal number (with no data gap) expected on the measurement period. As could be expected, we note that the processing is least beneficial to the tagged objects with the best read rates ; on the contrary, the data availability increase is much higher for tags with low read rates.

Discussion

Figure 2.7 shows that the main benefits of the fusion approach arise in the scenario of a difficult tag reading, e.g. when multipath interference is strong or when the signal strength is poor. In most cases this occurs on tag that are either at a great distance from the antenna, or when the read angle is high.

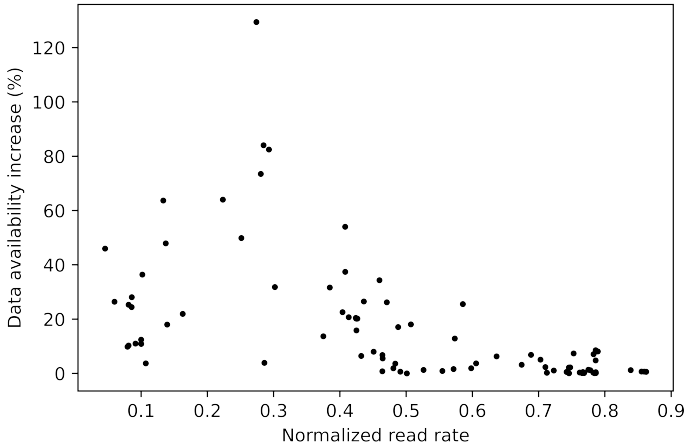

FIGURE 2.7 Data availability increase in percentage after applying the MF/MA/MT processing, as a function of the normalized read rate for every site.

Nb of frequencies used	2	3	4
Data availability increase (%)	8	11	13

TABLE 2.3 Cumulative data availability increase brought by the MF processing on Pont-Bourquin, depending on the number of frequency channels taken into account.

The increase in data robustness is clearly highlighted in such situations. We also note that several tags with the lowest read rates (close to 0.1) do not benefit as much from the processing.

We now turn to a more specific discussion on the processing steps, based on the results from Table 2.1.

The MF fusion is the main contribution to data availability increase. Table 2.3 shows the cumulative improvement brought by each new frequency channel, on the Pont-Bourquin site. This highlights that frequency diversity is a major aspect, and that even broader frequency windows would further improve the data availability. The MF fusion approach yields much better results on Pont-Bourquin and Valloire than on the two other sites. This is most likely due to the environmental conditions on these two sites : a higher altitude with stronger presence of snow. The corresponding multipath effects and signal strength diminution, although not critical in general, can worsen the data quality in already deteriorated situations. In such scenarios, the multi-frequency approach proves to be valuable.

The relatively low increase from the MA processing on all sites, is most likely due to the nature of

the general measurement setup : antennas are the same model and often rather close together. Hence the situations where one antenna reads a tag and not the others are rare.

We note that the multi-tag (MT) fusion brings a highly variable improvement. This can be explained by the height difference between tags on an object : the objects shaded by multipath interference or micro-topography will greatly benefit from MT fusion, whereas those that are in a better radio-frequency environment will not. Also, in cases where the lowest of the two tags is poorly read, the MT fusion will not bring significant improvements either, because most of the data comes from the topmost tag.

Moreover, Table 2.1 shows that the data from l'Harmalière and Bidart benefit much less from the processing, than the two other sites. This is most likely because both setups were already optimized to obtain the highest reading availability : relatively short distances between antenna and tags, more overall measurements thanks to higher number of antennas, as well as tag and antenna orientation optimization.

Measurement quality and trueness is also sensitive to multipath interference, which is a general challenge in RFID localization [DiGiampaolo and Martinelli, 2020]. Multipath is related to terrain topography, system geometry, but also to soil humidity and snow cover. As studied in [Charléty et al., 2022b] multipath generates both a measurement bias, a higher random error and a potential data loss due to the weak signal. The measurement errors amount to a centimeter-scale localization error in the horizontal plane. As of now, the presented data processing scheme can mitigate some of these effects : the multi-frequency approach takes advantage of the different multipath behavior with varying frequency, and the multi-tag and multi-antenna approaches yield a more multipath-robust measurement thanks to spatial diversity.

Environmental conditions can also have a strong influence on RFID-phase measurements. Phase random fluctuations can imply centimeter value errors in localization, as studied in [Le Breton et al., 2017]. This study confirms the need for using appropriate hardware for outdoor phase-stable RFID measurements. The main limitation to a spatial up-scaling of the method is the tag reading range. The current method cannot read the Survivor RFID tags past a 60 m maximum distance, which limits

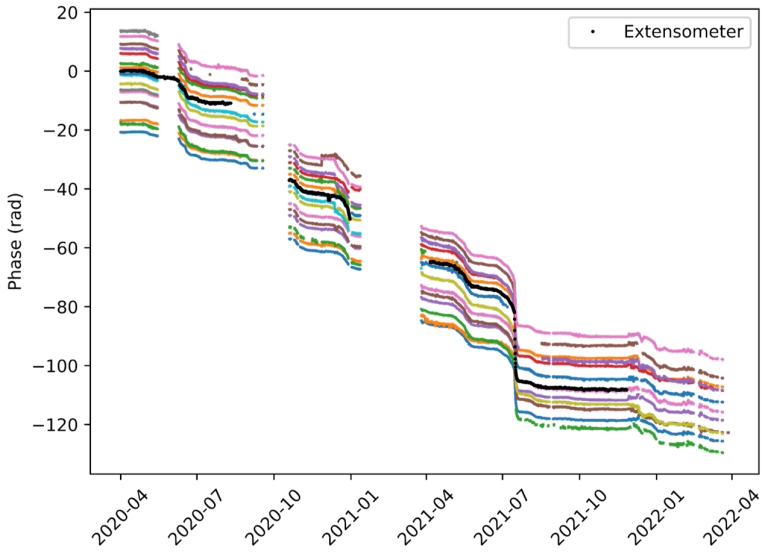

FIGURE 2.8 Final results from the last two years of RFID data on the Pont-Bourquin site. Each colored line represents the displacement of a tagged object, after all processing (MF, MA then MT) and after guided unwrapping with the group-guide and extensometer data (black line). An offset was added to every data series to increase readability.

the size of the monitored field. The reader antennas directivity can also limit the angular range, both horizontally and vertically.

In order to increase the size of the monitored areas, long-range tags were installed along with a more sensitive reader (Impinj R700). For even wider areas, new methods are developped based on Unmaned Aerial Vehicle (UAV), as described in [Breton et al., 2021, Buffi et al., 2018].

Figure 2.8 illustrates a portion of the final results for the Pont-Bourquin landslide. Through this figure we do not claim to present quantitative results concerning the localization accuracy of the RFID monitoring approach. Ideally speaking, the validation of our approach would necessitate independent reference measurement on the position of each tag, which is hardly feasible for technical and economical reasons. Nevertheless we point out that this method has already proven its centimeter-scale accuracy through multiple works [Le Breton et al., 2017, Le Breton et al., 2019, Charléty et al., 2022b], and that the present paper mostly aims at enhancing phase data.

2.6 Conclusion and perspectives

This paper proposes various data processing and fusion techniques, that take advantage of the RFID data redundancy in order to increase data availability and quality. These approaches are based on multi-source (frequency/antenna/tag) data fusion and on phase calibration using various references, with an objective of both increasing the available data size and decreasing the number of phase unwrapping errors. By applying such methods to RFID phase-based landslide monitoring, we show that these processes are valuable in long-term outdoor and complex environments. The overall average data availability improvement of the process was between 3% and 38% depending on the site, with several monitored objects greatly benefiting from the processes (+50% data availability). Moreover, the process yields more synthetic data which is therefore more exploitable.

Earth surface displacement monitoring with RFID has proven to be a viable solution, with four equipped sites across France and Switzerland. The varying nature of outdoor RFID data quality, will bring us to further develop data fusion approaches. In particular we foresee that applying bayesian filters to such measurement systems is a promising path.

Winter image of the Harmalière RFID measurement station. In the foreground, the first meters of damaged soil that constitue the landslide scarp.

Chapter 3

Kalman Smoothing for better RFID Landslide Monitoring

This chapter was published in the 31st European Signal Processing Conference (EUSIPCO) [Charléty et al., 2023b].

Authors : Arthur Charléty, Olivier Michel, Mathieu Le Breton.

Abstract

The use of Radio-Frequency Identification (RFID) in Earth Sciences has been growing in the recent years, notably for landslide monitoring using phase-of-arrival localization schemes. In this article, an Extended Kalman Filtering approach is presented to exploit RFID phase data for landslide displacement monitoring. The filtering is based on a stochastic Langevin equation for the state-space model, introducing a heuristic coupling based on the mechanical continuity of the landslide material. This helps correct measurement biases and deal with missing data in the tracking of multiple tags. The Kalman state covariance matrix is a useful indicator of the tags localization quality. It can be exploited to discriminate true displacements from multipath-induced artifacts. Phase unwrapping is performed implicitly through the state model. Preliminary clustering calculations suggest the existence of coherent landslide blocks. This is a new way of studying the landslide activation kinematics.

3.1 Introduction

The use of RFID in Earth Sciences has been growing in the recent years [Le Breton et al., 2022], with notable applications in landslide monitoring [Le Breton et al., 2019]. RFID tags are low-cost and versatile devices that can be easily deployed, and represent cheap and dense solutions for displacement monitoring. This was already demonstrated in both 1D and 2D long-term monitoring [Charléty et al., 2022b, Le Breton et al., 2017], with centimeter accuracy and weather robustness.

The counterpart of these advantages is the need to handle phase noise and ambiguity [Charléty et al., 2023]. The high amount of data and its redundancy, both in space and time, implies a high number of different sensors with inhomogeneous data sampling, variable noise levels and the risk of measurement bias (caused by multi-path interference for example [Giannelos et al., 2021]). For such datasets, fusion approaches based on Kalman Filters or Extended Kalman Filters (EKF) have been widely investigated for the localization of moving tags [Henriques Abreu et al., 2014]. EKF enable to work with missing data and variable measurement errors, which makes them particularly fit for redundant and noisy datasets. Moreover, the continuity of displacements can be implemented in the EKF physical model to further increase the robustness of the filter, like with RTK-GNSS localization [Gao et al., 2021]. Kalman-based sensor coupling is vastly demonstrated for GNSS sensor fusion [Sirtkaya et al., 2013, Falco et al., 2017]. Data fusion from multiple sensors is the main motivation for applying EKF to RFID tag localization [Yang et al., 2019] [Magnago et al., 2019]. In [Sarkka et al., 2011a, Bekkali et al., 2007] an EKF is used to fuse data from multiple antennas in order to perform indoor localization. In a real-world scenario, [Hoffman and Bester, 2020] demonstrates RSSI and phase data fusion to improve absolute ranging and relative displacement estimation.

EKF are also widely used in Earth Sciences, notably in landslide monitoring scenarios.They often address data scarcity through sensor fusion [Cai et al., 2022, Tan et al., 2020], or to synthesise different observables and models [Zhang et al., 2022, Lu and Zeng, 2020].

In general, combining RFID tags considerably enhances the precision of phase results, notably using an average operator [Le Breton et al., 2023b]. In this work, we aim to improve RFID data combination with a Kalman-based approach. We address data scarcity and varying accuracy by exploiting data redundancy and physical heuristics in order to link multiple tags together. Namely, we implement the continuity of position and velocity both in space and time at the observation scale (about 1-10 m). The

main specificity of the proposed method lies in the coupling of multiple tags at different positions, based on the concept of landslide kinematic element [Schulz et al., 2017]. The approach we propose yields an improved and model-based phase unwrapping, as well as data completion and fusion. Furthermore it provides an estimate of the quality of the localization estimation, which is of great importance from a user point-of-view. This work is the first attempt at applying the EKF to improve long-term, outdoor and slow-moving RFID monitoring.

3.2 Experimental Setup

The Harmalière landslide (Sinard, France) is a slow moving landslide located near Grenoble in the western Pre-Alps. It is investigated by many research projects [Fiolleau et al., 2021]. The RFID setup, installed in 2020, consists of 4 reader antennas and 32 tags spread in a 30m by 30m investigated zone. Tacheometry reference measurements are frequently performed. The experimental setup (see Fig. 3.1) was described and validated elsewhere [Le Breton et al., 2017, Le Breton et al., 2019, Charléty et al., 2022b], as well as signal processing methods for data availability improvement [Charléty et al., 2023], and showed centimeter-accuracy in 2D over year-long monitoring.

3.3 Model and Kalman filter

Measurement setup A set of M antennas (4 in our setup) at respective positions $\mathbf{x}_a^m$, $m \in \{1, \dots, M\}$ are spread at the border of the landslide area (see Fig.3.1A). The antenna of index m estimates a phase propagation delay for each single tag at position $\mathbf{x}$. This phase is:

$$\Phi_m = \frac{4\pi f}{c} d_m + \Phi_{off} \, ,$$

where Φ_{off} holds for the phase offset and $d_m = \|\mathbf{x} - \mathbf{x}_a^m\|$. All phases are only observable modulo π (8 cm ambiguity) due to RFID reader constraints. A first order approximation with respect to the tag displacement gives:

$$\delta d_m = \mathbf{u}_m^T \delta\mathbf{x} + o(\|\delta\mathbf{x}\|), \quad \delta\Phi_m \approx \tfrac{4\pi f}{c} \mathbf{u}_m^T \delta\mathbf{x} \tag{3.1}$$

where $\mathbf{u}_m = \frac{\mathbf{x}-\mathbf{x}_a^m}{\|\mathbf{x}-\mathbf{x}_a^m\|}$ is a unit norm vector. For this single tag and M antennas, we get:

$$\delta\mathbf{\Phi} = [\delta\Phi_1, \ldots, \delta\Phi_M]^T = \frac{4\pi f}{c} \begin{pmatrix} \mathbf{u}_1^T \\ \vdots \\ \mathbf{u}_M^T \end{pmatrix} \delta\mathbf{x} = \mathbf{K}\delta\mathbf{x}\,, \tag{3.2}$$

Where $\mathbf{K} \in \mathbb{R}^{d\times M}$ and d is the space dimension (3 in our case). The classical MSE estimation of the tag position change, given a set of M phase measurements leads to solve the normal equation:

$$\mathbf{K}\mathbf{K}^T\delta\mathbf{x} = \mathbf{K}\delta\mathbf{\Phi}\,.$$

Assuming that phase measurements errors are Gaussian distributed, this solution matches with the maximum likelihood estimate. It provides an unbiased estimate of $\delta\mathbf{x}$ and with a variance equal to $(\mathbf{K}\mathbf{K}^T)^{-1}$.

This approach exhibits two problems: first it requires that the antenna/tag geometry ensures that $\mathbf{K}\mathbf{K}^T$ has full rank (as studied in [Charléty et al., 2022b]), and the variance depends on the conditioning of this latter matrix. This builds the motivation for developing an alternative approach relying on Kalman filtering. To that end, a state equation is required, usually directly related to the displacement physical model.

In early-warning and monitoring applications, empirical or kinematic landslide models are often used [Bernardie et al., 2015, Intrieri et al., 2019]. A simple and approximate model is derived below.

Physical model Let Z_t be a state vector in $\mathbb{R}^{2dN}$, constructed from both positions $\mathbf{P}_t$ and velocities $\mathbf{V}_t$ of a set of N tags at time t:

$$Z_t = \begin{pmatrix} \mathbf{P}_t \\ \mathbf{V}_t \end{pmatrix} = (\mathbf{x}_t^{1\,T} \ldots \mathbf{x}_t^{N\,T} \mathbf{v}_t^{1\,T} \ldots \mathbf{v}_t^{N\,T})^T\,.$$

We propose a model constructed from both the fundamental principle of dynamics in physics and from an heuristics stating that close enough tags will have coupled trajectories. Consequently, we assume that all movements are due to random forces or accelerations. Note that although gravity is the major long-term driving force constraining downwards displacements, local landslide block activity generates displacements in all directions (for example, block rotation generates upward movement).

Thus velocities behave like Wiener-Levy processes, and the system will follow the following Langevin equation [Arnold, 1973]:

$$d\begin{pmatrix}\mathbf{P}_t\\ \mathbf{V}_t\end{pmatrix}=\begin{pmatrix}\mathbf{0} & C\\ \mathbf{0} & \mathbf{0}\end{pmatrix}\begin{pmatrix}\mathbf{P}_t\\ \mathbf{V}_t\end{pmatrix}dt+\begin{pmatrix}0_{Nd}\\ \sqrt{\beta}\mathbf{1}_{Nd}\end{pmatrix}\begin{pmatrix}0_{Nd}\\ d\mathbf{w}_t\end{pmatrix}, \tag{3.3}$$

where $\mathbf{0}$ and C are $Nd \times Nd$ matrices, 0_{Nd} and $\mathbf{1}_{Nd}$ are constant (resp. 0 ad 1) vectors of dimension Nd. $\mathbf{w}_t$ is the Nd dimensional Wiener Levy process with unit covariance matrix (assuming that all driving forces are independent and have identical diffusion constants). C is the velocity coupling matrix whose expression will be discussed later. $\sqrt{\beta}$ entails inertial mass and power of the driving force. It represents the diffusion coefficient of the process. From Eq. (3.3) the Fokker-Planck ordinary differential equation followed by the covariance matrix of Z_t is derived and after integrating on the interval $[0, t]$, we get [Arnold, 1973, Jazwinski, 2008]:

$$\Gamma_z(t)=\beta\begin{pmatrix}\frac{t^3}{3}CC^T & \frac{t^2}{2}C\\ \frac{t^2}{2}C^T & t\mathbb{I}_{Nd\times Nb}\end{pmatrix}. \tag{3.4}$$

The above expression of $\Gamma_z(t)$ is of major interest as it accounts for both the decrease of the model reliability when the time t between two consecutive observations increases, and for the statistical dependence of position an velocity estimates. This latter dependence is related to the fact that velocities are not observed but derived from the position estimates.

Velocity coupling matrix: Arguing that tags near each other should have similar velocities (because they belong to the same kinematic elements [Schulz et al., 2017]), the following structure for C is proposed:

$$[C]_{ii}=(1-\alpha)\quad [C]_{ij}=\frac{\alpha}{\sigma_j^2}\mathrm{e}^{-\frac{d_{ij}}{\lambda}}\quad i,j\in\{1,\dots,N\}\quad , \tag{3.5}$$

where λ accounts for the characteristic distance above which tags are considered to have possibly independent velocities, and σ_j^2 will be the tag j estimated velocity error variance. This allows to lower the influence of tags whose velocity is badly estimated. Note that C is time dependent (d_{ij} and σ_j vary with time). Forcing C to be the identity will lead to a solution where each tag position and velocity may be tracked independently from each other.

State equation: All previous results and equations lead to the state equation (integral form of Eq. (3.3),

between t and $t' > t$):

$$Z_{t'} = \begin{pmatrix} \mathbf{I} & C_t \\ \mathbf{0} & \mathbf{I} \end{pmatrix} Z_t + \gamma_{t'} = AZ_t + \gamma_{t'} \ , \tag{3.6}$$

where $\gamma_{t'}$ is a $2Nd$-dimensional white noise with correlation matrix $\Gamma_z(t - t')$ defined by Eq. (3.4). Note that the larger the time elapsed between two observations (at t and t'), the larger the covariance matrix of the state noise $\gamma_{t'}$.

Observation equation: It is derived from Eq. (3.2), to which some observation noise is added. The measurement covariance matrix of the observation noise $\xi_{t'}$, noted Γ_Φ, depends upon the instrument used to estimate $\delta\mathbf{\Phi}$ (see [Le Breton et al., 2017, Charléty et al., 2023] for more details). Finally, by assuming that $\delta\mathbf{x}_{t'} \approx (t' - t)\mathbf{V}_t$ (this is satisfied if the velocities vary slowly on the interval $[t, t']$), we get:

$$\delta\mathbf{\Phi}_{t'} = \begin{pmatrix} \mathbf{0} & (t' - t)\mathbf{K}_t \end{pmatrix} Z_{t'} + \xi_{t'} = H_t Z_{t'} + \xi_{t'} \ . \tag{3.7}$$

Although this equation is linear at each step, it is important to notice that H_t varies with t.

Remarks: In practice, forcing row and column of index k of Γ_Φ to take very large values at some time instants where measurements from antenna k are missing allows the Kalman filter to rely only on the state equation at these time instants; actually, it can be shown that the Kalman gain k-th component will be thus forced to a near zero value. Nonetheless, the velocity coupling term C_t will still force some local ensemble movement. The problem of phase unwrapping disappears in the Kalman formulation as the 'modulo π' term is determined by considering the forecast:

$$\delta\hat{\mathbf{\Phi}}(t'|t) = H\hat{Z}_{t'|t} \ .$$

This quantity is estimated at t' from the system observed until time t only. Setting both state and noise covariance matrices is critical, as it deals with the precision/robustness tradeoff. Choosing β is therefore critical. On the contrary, setting $C = \mathbf{I}$ in Γ_z has a lower importance in practice, and will be adopted in order to simplify the Kalman filter implementation.

The terms σ_j and d_{ij} are replaced in Eq. (3.5) by the estimated velocity error covariance for tag j and by $|\hat{\mathbf{x}}_i - \hat{\mathbf{x}}_j|$ respectively, estimated at time t. The derivation of the Kalman filter equation is then classical and is not detailed is this short article.

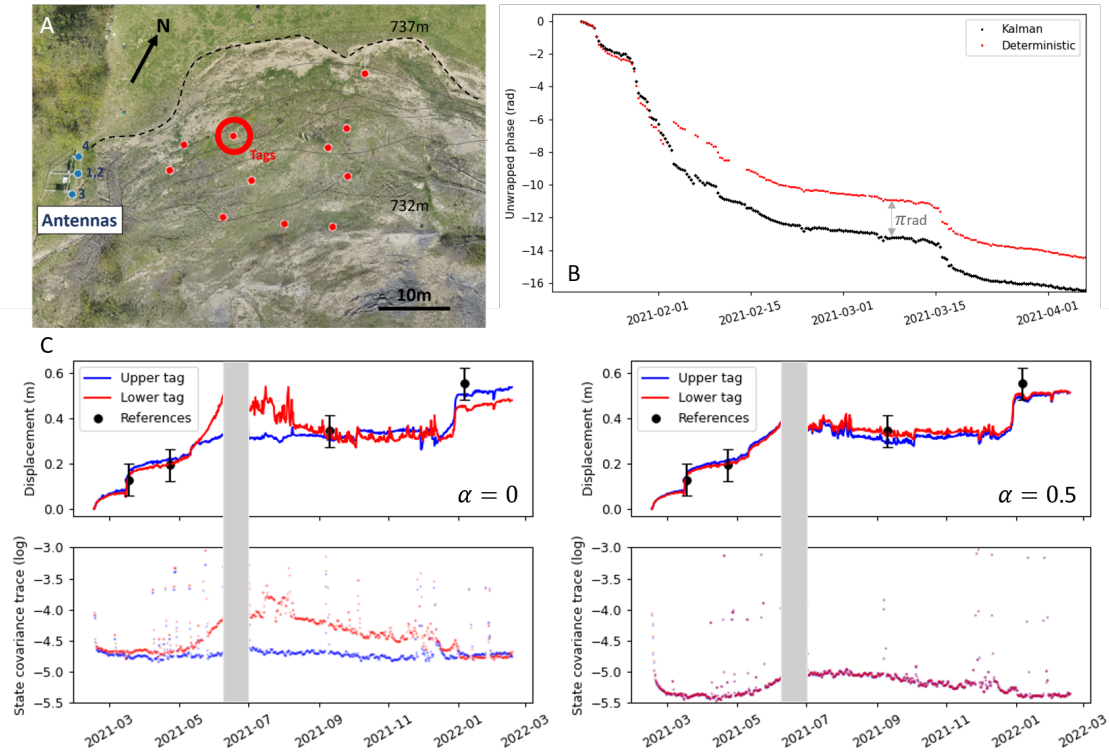

FIGURE 3.1 A : Aerial view of the landslide equipped with RFID monitoring. B : Example of phase series, unwrapped by the Kalman filter or by a deterministic approach [Charléty et al., 2023]. C : (Top) Displacement for two tags on the same support at different heights (highlighted tag in A). The two tags were chosen among 32 to be those with the best quality of recorded data. Left: $\alpha = 0$ (no coupling between tag velocities). Right: $\alpha = 0.5$ (equal contribution of mutual velocities). The black dots represent reference measurement, with the corresponding error bar. (Bottom) Trace of the Kalman covariance state matrix for each tag.

We have derived an Extended Kalman Filtering approach including sensor state coupling, and accounting for position-velocity error correlation. Next section will comment on simple real-data results.

3.4 Results and discussion

Figure 3.1C presents displacement results from a pair of tags, with their *a posteriori* (after Kalman filtering) error covariance estimation ; results for two different values of α (different C matrices) are compared. The grey bar represents a data gap caused by hardware failure. Two main phases of activity stand out : March 2021 and January 2022, with peak velocities of 2 cm/day.

As expected, the covariance estimation shows a strong sensibility to missing data, with extremely

high values that are not shown here. Except from these (useful) values which can be filtered out, the variation of the covariance trace informs the user about the overall quality of the localization.

In the case where $\alpha = 0$ ($C = \mathbf{I}$) it can be considered as a proxy for detecting interference phenomena or defective material. The presented pair of tags should share approximately the same displacement, as they are positioned on the same object. Nonetheless we see a drift of the lower tag occurring from May to October 2021, with a temporary displacement difference of 20 cm between the two tags. This drift, along with the strong increase in state covariance, is most likely a sign of radiofrequency interference [Whitney et al., 2018]. This interpretation is confirmed by the received signal strength indicator which strongly decreases during the same period. As shown in [Charléty et al., 2022b] for the same setup, this phenomenon mostly impacts tags positioned closer to the ground. The state covariance estimate is a tool for assessing the confidence of a result. In the present case, the apparent displacement shown by the lowest tag around June 2021 can be discarded, it is identified as an artifact due to the important state covariance increase.

In the case of $\alpha = 0.5$ the drift between tags is diminished, as the model imposes a partially-shared velocity. It can be shown that the choice of $\alpha > 0$ implies a decrease in the *a posteriori* covariance, and this theoretical result is validated by observation. However this higher precision is obtained at the cost of a decreased robustness of the filter : it is less stable with respect to a departure between model and reality. We also note that the drift of the lower tag is propagated to the upper tag, generating a displacement artifact on both tags for the whole period of May to October 2021. Using a higher number of tags as well as a different value for α should be a way of solving this issue [Eom et al., 2011].

An example of model-based phase unwrapping is shown in Fig. 3.1B. The velocity propagation implemented in the model allowed for a correct unwrapping compared to deterministic methods [Charléty et al., 2023].

The coupling between tags relies on the concept of kinematic element, stating that landslide blocks stand out with coherent displacements. In practice this assumption is often verified in the current geomorphological environment [Schulz et al., 2017]. Nonetheless, the distance-based correlation does not fully correspond to the landslide block situation : close tags could behave differently if they're on a different block. Implementing a correlation function based on tag clusters could improve the results.

3.5 Conclusion

Extended Kalman Filters applied to long-term outdoor RFID data allow to complete data gaps with multi-tag guidance thanks to a position-velocity model, and to perform model-based phase unwrapping. The Kalman state covariance matrix is a usefull indicator of the localization quality. It can be exploited to discriminate true displacements from multipath-induced artifacts.

Images depicting most hardware used throughout the present research work. (Left) GPS mobile laying oh the main landslide scarp. (Top right) Tacheometer, fixed station, and flying UAV. (Bottom right) RFID tags on the field during an experiment.

Chapter 4

2D Phase-Based RFID Localization for On-Site Landslide Monitoring

This chapter was published in MDPI Remote Sensing Volume 14, Issue 15 [Charléty et al., 2022b].

Authors : Arthur Charléty, Mathieu Le Breton, Eric Larose, Laurent Baillet.

Abstract

Passive radio-frequency identification (RFID) was recently used to monitor landslide displacement at a high spatio-temporal resolution but only measured 1D displacement. This study demonstrates the tracking of 2D displacements, using an array of antennas connected to an RFID interrogator. Ten tags were deployed on a landslide for 12 months and 2D relative localization was performed using a phase-of-arrival approach. A period of landslide activity was monitored through RFID and displacements were confirmed by reference measurements. The tags showed displacements of up to 1.2 m over the monitored period. The centimeter-scale accuracy of the technique was confirmed experimentally and theoretically for horizontal localization by developing a measurement model that included antenna and

tag positions, as well as multipath interference. This study confirms that 2D landslide displacement tracking with RFID is feasible at relatively low instrumental and maintenance cost.

4.1 Introduction

Ground deformation monitoring with high resolution both in space and time remains a challenge due to the high cost of existing solutions, and to environmental limitations, such as meteorological phenomena, rough terrain or dense vegetation. Amongst several remote sensing methods [Scaioni et al., 2014, Zhao and Lu, 2018], surface monitoring of large landslides can be typically performed through interferometric synthetic aperture radar (InSAR), either by space-borne measurements [Colesanti and Wasowski, 2006, Strozzi et al., 2005] or using ground-based stations [Wang et al., 2020b, Tarchi et al., 2003, Monserrat et al., 2014, Helmstetter and Garambois, 2010, Aryal et al., 2012]. Despite the high space resolution of these methods, the station cost remains high and the time resolution can be multiple days in the case of satellite remote sensing. More localized techniques, such as GPS [Benoit et al., 2015, Li et al., 2017, Šegina et al., 2020, Dong et al., 2020] and radiofrequency-transponders [Intrieri et al., 2018, Mucchi et al., 2018], show higher time resolution, but also require on-board power sources which greatly increase initial cost and maintenance.

In this context, radio-frequency identification (RFID) has shown increasing potential for earth science applications [Schneider et al., 2014, Breton et al., 2021]. Amongst other applications, it is foreseen as a promising alternative for landslide and civil engineering structure deformation monitoring [Le Breton et al., 2019] due to its low cost relative to other solutions, and because it works under rain, snow and vegetation cover conditions [Le Breton et al., 2017, Le Breton, 2019]. It can thus be used as a tool for landslide early-warning [Intrieri et al., 2012], forecasting or long-term monitoring [Intrieri et al., 2019]. A wide range of solutions exist for tag localization using RFID [Balaji et al., 2020, Miesen et al., 2011a], with various possibilities both in measured quantity and in terms of the measuring scheme.

The quantities most used for localization are the received signal strength and the back-scattered phase of arrival. Signal-strength-based methods have been widely used for tag localization [Ni et al., 2003, Subedi et al., 2017, Rohmat Rose et al., 2020, Martinelli, 2015, Subedi et al., 2017, Shen et al., 2019]. However, phase-based methods have shown better precision and reliability in recent years [Scherhäufl et al., 2015, Wang et al., 2016, Zhou and Griffin, 2012], primarily because they are less sensitive to

environmental variations and because the phase of the signal varies more rapidly with distance than the received signal strength.

Phase-based localization is divided into multiple schemes, which are extensively presented elsewhere [Li et al., 2019a, Huiting et al., 2013, Pelka et al., 2014, Nikitin et al., 2010]. These schemes generally rely on either multistatic stationary antennas and different carrier frequencies [Povalac and Sebesta, 2011, Scherhäufl et al., 2014, Scherhäufl et al., 2015], or on a moving antenna with a known trajectory (e.g., the synthetic aperture radar technique) [Buffi et al., 2017, Buffi et al., 2018, Motroni et al., 2018, Bernardini et al., 2020b, Gareis et al., 2020]. This paper focuses on a monostatic multi-antenna time-domain phase difference (TD-PD)-inspired scheme, as TD-PD has shown the best results for measuring relative displacements outdoors [Le Breton et al., 2019], with a precision of about 1 cm over long time periods for 1D displacement tracking. To date, RFID systems deployed to monitor moving ground only provide one-dimensional distance information and are subject to phase unwrapping issues that could be solved by using multiple antennas. In this article, we test the stationary configuration for 2D RFID tag localization using a set of four antennas in a TD-PD relative localization approach, and also discuss 3D localization perspectives. To the best of our knowledge, this is the first attempt at 2D-localization of RFID tags in an outdoor scenario, using a monostatic, monofrequency multi-antenna setup.

In the following section, we present the instrumentation of the experimental site and the methodology for data acquisition and processing. Section 4.4 provides theoretical background and experimental validation of the RFID measurement error in order to decide on ideal antenna positioning by optimizing the localization accuracy and phase ambiguity. Section 4.5 reports on an example of 12 months of surface deformation monitoring on the slow-moving Harmalière landslide.

4.2 Instrumentation and Methods

Experimental Site: Harmalière Landslide

The Harmalière landslide (Sinard, Isère, France) is located in the Trièves area about 50 km south of Grenoble in the western Prealps (see Figure 4.1). Trièves appears as a sedimentary plateau eroded by the Drac river; the plateau is formed by Quaternary varved clays and alluvial materials deposited in a glacially dammed lake during the Würm period [G., 1973]. Quaternary sediments also include

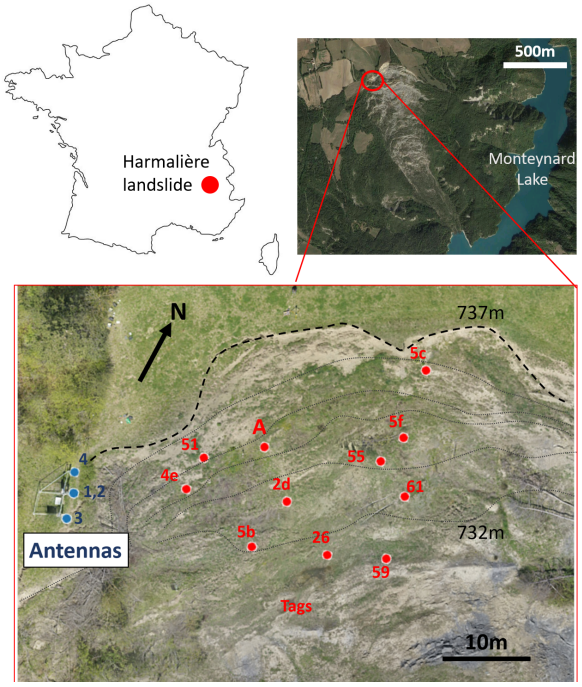

FIGURE 4.1 (**Top**) The Harmalière landslide location in France. (**Bottom**) Overview of the Harmalière landslide, with the RFID tag distribution (red points). Blue points : antennas and acquisition system. The dotted black line represents the landslide scar, the gray dotted lines represent 1-meter isolines.

silts, sometimes with a morainic cover, and rest on either interglacial Riss-–Würm period glaciofluvial materials (gravels and sands) or on the underlying Jurassic carbonate bedrock. The thickness of the clay deposits can vary from 0 to a maximum of 200 m [Jongmans et al., 2009]. The landslide is southeast oriented, 400 m wide at the top, narrowing to 150 m at the toe. It develops from an altitude of 735 m (asl), down to the Monteynard Lake (480 m), over a distance of about 1.5 km. It was abruptly activated in 1981 and has remained active ever since, with new peaks of activity in 2016 and 2017 [Fiolleau et al., 2019]. The slow moving landslide shows regressive behaviour, the headscarp retreating at an average velocity of 1 m/year, with very strong variations from year-to-year (including almost a decade of rest). The central body of the landslide is moving at velocities ranging from cm/year to m/year, with possible dramatic acceleration phases (m/day). A variety of research subjects are currently investigated in connection with it [Fiolleau et al., 2021, Fiolleau et al., 2019].

RFID Instrumentation and Localization

RFID Instrumentation

In February 2020, a section of the landslide was equipped with an RFID system consisting of 32 battery-assisted passive tags and an acquisition station located near the landslide scar (see Figure 4.1). These tags can last about a decade without maintenance or replacement in the present real-time monitoring scenario. The station includes four antennas, an interrogator (Impinj SR420), a micro-computer (RPI-3B), and a modem to send the data automatically to a remote server, as described by (patent pending FR-17/53739). It is powered by a photovoltaic module and a wind turbine. The station collects RFID data for 3 minutes every 20 min from every tag and every antenna. The data includes the phase of arrival (termed here "phase") measured at 865.7 Hz, the received signal strength indication and the tag temperature. The tags were placed in pairs on fiber glass stakes 50 cm and 1 m above ground. They were spread out within the antennas reading range in a zone approximately 30 m $\times$ 30 m wide (see Figure 4.1), in such a way as to maximize the line-of-sight readability of each tag by multiple antennas. To validate the RFID localization calculations, the position of the tags was measured with a LEICA TCR805 tacheometer and a handheld target (estimated precision 4 cm), approximately once every month.

RFID Localization Scheme

TD-PD is a relative ranging technique based on phase variation $\delta\phi = \phi_1 - \phi_0$ between two measurements at different points in time. $\delta\phi$ is related to the radial distance variation $\delta r = r_1 - r_0$ between the tag and reader antenna, by the following equation:

$$\delta r = -\frac{c}{4\pi f}\delta\phi \tag{4.1}$$

where f is the frequency of the electromagnetic wave (see values above) and c is the speed of light in the propagation medium. It is important to note that Equation (4.1) is only valid for displacements smaller than $\lambda/4 \approx 8$ cm between two phase measurements because of phase ambiguity. In the present case, this condition is generally fulfilled as the incremental displacements are small compared to the wavelength (usually less than 1 cm between two successive acquisitions). Moreover, a series of phase measurements can generally be unwrapped using well-defined algorithms. In this case, Equation (4.1)

is valid for any unwrapped phase variation.

Section 4.3 presents a multidimensional localization scheme based on TD-PD.

4.3 Theoretical Model

In this section, we derive a mathematical model for phase-based RFID localization to compute the localization error of our real experiment. The main goal of this derivation is to study the origins of the localization uncertainty, mainly with respect to the system geometry and the physical measurement process.

From now on, we will consider that all phase measurements are unwrapped, and that Equation (4.1) is valid for all phase variations. Most presented tags were correctly read and no unwrapping error was detected in the monitored period. The specific case of an unwrapping error is examined separately, and does not fall within the scope of the present study.

In the following, index i describes a series of measurements starting at $i = 0$ and j describes the antenna indexing.

Localization Model

One Dimensional TD-PD

The localization method presented in this paper is based on the tag phase shift measured by each antenna at different points in time (TD-PD) [Nikitin et al., 2010]. In a homogeneous medium, the phase shift $\phi_{i,j} - \phi_{0,j}$ between the initial and the i-th (unwrapped) phase measurement, is directly proportional to the radial displacement $\delta r_{i,j}$ between the tag and antenna j (see Equation (4.1)).

Assuming an initial radial distance $r_{0,j}$, we obtain a series of radial distances $r_{i,j}$ from a measured phase series $\phi_{i,j}$:

$$r_{i,j} = r_{0,j} + \delta r_{i,j} \tag{4.2}$$

where $\delta r_{i,j}$ is obtained directly through Equation (4.1). This localization method is, hence, relative to the initial position, as it does not allow for absolute positioning without further information about the system (e.g., when $r_{0,j}$ is not known).

2D Relative Displacement Approach

Using the measurements of multiple antennas, we can expand this TD-PD method with spatial considerations. For this purpose, we need both the phase measurements and the geometrical coordinates (x_j, y_j) of each antenna. This derivation focuses on the 2D problem; the 3D case will be briefly discussed at the end.

We define the initial distance $r_{0,j}$ from the antenna j to the tag:

$$r_{0,j} = \sqrt{(x_j - x_0)^2 + (y_j - y_0)^2}$$

where (x_0, y_0) are the initial coordinates of the tag and (x_j, y_j) those of the antenna.

Applying Equation (4.2), we obtain a series of radial displacements from the phase measurements of each antenna. From these radial distance measurements, a multilateration approach [Norrdine, 2012] can be applied to estimate the most probable position $(\hat{x}_i, \hat{y}_i)$ for the tag at the ith position. Amongst various possible methods of multilateration, we use an optimization algorithm that minimizes the following cost function Cf for the i-th measurement:

$$Cf_i(x, y) = \sum_{j=1}^{N_a} \left| r_{i,j} - \sqrt{(x_j - x)^2 + (y_j - y)^2} \right| \tag{4.3}$$

$$(\hat{x}_i, \hat{y}_i) = \underset{(x,y)\in\mathbb{R}^2}{argmin}\big(Cf_i(x, y)\big)$$

where (x, y) are the test point coordinates, N_a is the number of antennas, $r_{i,j}$ is the i-th radial distance from antenna j, and $(\hat{x}_i, \hat{y}_i)$ is the most probable tag position. The minimization of this cost function was performed using the Trust-region optimization algorithm [Conn et al., 2000] implemented in the Scipy-optimize Python module.

Geometrical Localization Sensitivity

In this section, we focus on theoretical considerations regarding the localization sensitivity of the geometrical antenna-tag system to compute the value and direction of a displacement error of the tag with respect to a phase measurement error [Le Breton et al., 2017]. For a given antenna position (x_j, y_j), the absolute phase accumulated on a linear ray path (line of sight, LOS) between the antenna

and a point (x, y) is expressed as follows:

$$\phi_j(x, y) = -\frac{4\pi f}{c} \times \sqrt{(x_j - x)^2 + (y_j - y)^2}$$

Let us define $K_{\phi j}$ as the space gradient of the measured phase ϕ_j, also defined as the phase sensitivity kernel, expressed in the spatial dimension as:

$$K_{\phi j}(x, y) = \begin{bmatrix} \frac{\partial \phi_j}{\partial x} \\ \frac{\partial \phi_j}{\partial y} \end{bmatrix} = \begin{bmatrix} K^x_{\phi j} \\ K^y_{\phi j} \end{bmatrix} \tag{4.4}$$

For a system consisting of two antennas (A and B) and small phase variations, the relation between the phase variation vector $\delta\phi$ and the true tag displacement δr can then be approximated by the linear matrix system:

$$\begin{bmatrix} \delta\phi_A \\ \delta\phi_B \end{bmatrix} = \begin{bmatrix} K^x_{\phi_A} & K^y_{\phi_A} \\ K^x_{\phi_B} & K^y_{\phi_B} \end{bmatrix} \begin{bmatrix} \delta\ x \\ \delta y \end{bmatrix}$$

That we can simply rewrite :

$$\delta\phi = K\delta r \tag{4.5}$$

Equation (4.5) holds for any number of phase measurements (thus any number of antennas N_a), and any number of space dimensions M; in such cases, K will be an $M \times N_a$ matrix. It expresses the direct solution of the phase-based relative localization problem, where K represents the transformation matrix from measured phase space to localization space.

For the sake of simplicity, consider now that $N_a = M = 2$, which implies a bijective relationship between phase measurements and tag 2D relative displacement. In this case, the invertibility of the K matrix is almost always possible—the only exceptions are when the point position (x, y) coincides with that of one antenna, or when it is aligned with the two antennas. We exclude these limit cases that have no significance in our experiments. The above equation can then be reversed and gives the theoretical phase sensitivity of the tag position:

$$\delta r = K^{-1}\ \delta\phi \tag{4.6}$$

We now consider the linear transformation matrix K^{-1} to which we apply singular value decom-

position (SVD). Any real matrix can be decomposed as follows [Van Loan, 1976]:

$$K^{-1} = U\Sigma V^{\top} \tag{4.7}$$

In our model, $V^{\top}$ represents the eigenvectors in phase space, Σ the diagonal eigenvalue matrix and U the eigenvectors in localization space.

In this derivation, we assume the same variance for all phase measurements; hence, the covariance matrix C_{ϕ} is defined as follows :

$$C_{\phi} = \sigma_{\phi}^2 \cdot I_{N_a} \tag{4.8}$$

where σ_{ϕ} is the typical phase standard deviation and I_{N_a} is an identity matrix of size N_a. C_{ϕ} is, thus, a constant diagonal matrix in our model, with typical values of 0.04 rad. This phase standard deviation is both an experimentally computed value and also corresponds to the modeled approximation of Equation (4.12) (see next Section).

Considering a given phase measurement uncertainty for each antenna, we can plug any phase distribution into the transformation from Equation (4.7). The shape and orientation of the resulting spatial distribution around tag position (that we will call localization spot) is described by the localization-space covariance matrix C_r. This matrix can be expressed in the following way, depending on K^{-1} as well as the hypothetical covariance of the phase measurement matrix C_{ϕ}:

$$C_r = (K^{-1})^{\top} C_{\phi} K^{-1} = U\Sigma^2 U^{\top} \tag{4.9}$$

Extracting the eigenvalues and eigenvectors of C_r allows for a completely analytical determination of the localization spot properties (especially the direction of highest error) for a given antenna-tag geometry, as shown in Figure 4.2. With a phase error of 0.04 rad, and at the given tag position, we expect a localization random error of about 1 cm. Note that in the model, any relative increase in phase error will result in the same relative increase in localization error, as the measurement operator is linear.

The calculation presented above can be extended to a three-antenna system for a 3D localization problem, following Equations (4.1) to (4.9) with K a 3×3 matrix. In the case where $N_a > 3$, the system from Equation (4.5) is overdetermined, and a least-squares solution has to be found [Anton and Rorres,

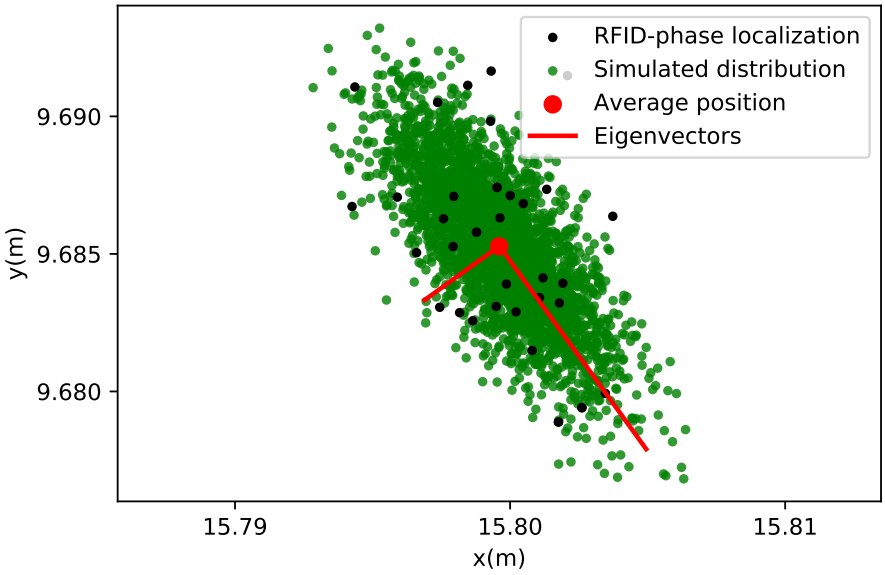

FIGURE 4.2 Localization error shape at the position of tag A (see Figure 4.1) compared with the RFID position estimation during a stable period in the Harmalière (November to December 2020). The green point distribution is computed through the K^{-1} transformation (see Equation (4.6)), using a Gaussian phase distribution with a standard deviation of 0.04 rad. The eigenvectors of the green distribution (red lines) are scaled up to encompass 97% of the data. The black points correspond to the RFID-phase localization results. The antenna positions are set as in the real experiment (see Figure 4.1).

2013, Golub and Kahan, 1965]. Using the pseudo-inverse of K, Equation (4.6) then gives:

$$\delta r = (K^\top K)^{-1} K^\top \delta\phi \tag{4.10}$$

This new system can be solved and the eigenvectors computed by considering the transformation matrix $(K^\top K)^{-1} K^\top$.

Phase Error Model : Multipath, Phase Standard Deviation and Radiation Pattern

While the previous section focuses on geometrical localization error, we will now incorporate the impact of real-scenario error sources, e.g., antenna radiation pattern and multipath. The following derivation is based on the work of [Le Breton, 2019].

Multipath Propagation Model

Multipath interference is a major challenge in RFID-localization and several solutions have been proposed to estimate, reduce or mitigate its effect on measurements [Wang et al., 2020a,Faseth et al., 2011]. To start investigating the multipath, we use a simple two-ray model, assuming that the measured signal is a superposition of the line-of-sight ($p = 1$) signal and a signal reflected on the ground ($p = 2$), as shown in Figure 4.3. The two signals propagate over different path lengths r_p and orientations, which translate in different received power values due to Friis' law:

$$P_p(r) = \left(\frac{\lambda}{4\pi r_p}\right)^2 \times P_t \cdot G_T(i_p) \cdot G_R(i_p) \quad for\ p = \{1, 2\}$$

where P_t is the power transmitted by the antenna, P_p is the received power along path p, G_r and G_t are the receiver and transmitter gain which depend on the signal orientation angle i_p and the antenna radiation pattern, λ is the carrier wavelength and r_p is the path propagation distance. We can then define the amplitude gain $A_p(i_p, r_p)$ for the line-of-sight (1) and reflected (2) signals :

$$A_1(i_1, r_1) = \frac{1}{r_1}\sqrt{G_t(i_1) \cdot G_r(i_1)}$$

$$A_2(i_2, r_2) = \frac{1}{r_2}R(i_2)\sqrt{G_t(i_2) \cdot G_r(i_2)}$$

where $R(i_2)$ is the reflection coefficient impacting the reflected ray (which depends on ground relative permittivity). The received signal voltage s_p after normalization by the initial emitted voltage can be expressed by the following phasor:

$$s_p(i_p, r_p) = A_p(i_p, r_p) \cdot \frac{\lambda}{4\pi} \cdot e^{-jkr_p} \quad for\ p = \{1, 2\} \tag{4.11}$$

where k is the wave number. The resulting signal s_{tot} arriving on the tag is the sum of the two phasors:

$$s_{tot} = s_1(i_1, r_1) + s_2(i_2, r_2)$$

After accounting for tag modulation efficiency L_t [Rembold, 2009], and due to the reciprocity of all gain values during the back-scattered propagation, the full signal phasor received by the station

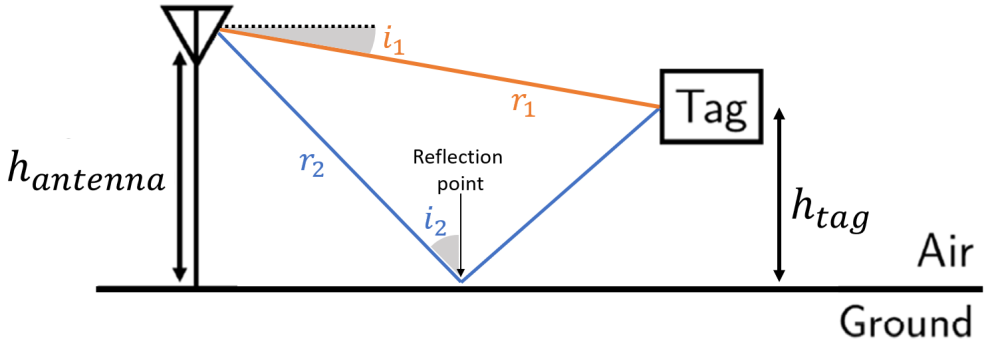

FIGURE 4.3 Schematic definition of the two-ray multipath model. The orange line represents the line-of-sight path with angle i_1 and propagation distance r_1. The blue line represents the reflected path with angle i_2 and propagation distance r_2. h_{tag} and $h_{antenna}$ are the tag and antenna heights above ground.

antenna is finally expressed as follows:

$$s_{full} = s_{tot}^2 \cdot L_t$$

As a reminder, the squared s_{tot} corresponds to the back-and-forth path of the signal.

Two Types of Phase Error

We define the phase measurement error as the difference between the ideal LOS phase and the full received phase. This error can be divided into two contributions: the phase random deviation σ_{rdm} and the systematic phase bias ϕ_b, which are both consequences of multipath interference. Let us now consider these two error contributions separately. Previous investigations [Le Breton et al., 2019] have shown a direct relationship between antenna received power P(W) and phase random deviation σ_{rdm}(rad), using the same acquisition configuration (tag, interrogator, and communication protocol):

$$\sigma_{rdm} = \frac{4\pi f}{c} \cdot 9.5 \cdot 10^{-9}/\sqrt{P} \tag{4.12}$$

where c is the light velocity and f the carrier frequency. This empirical relationship reproduces the phase error value of 0.04 rad used in the previous section. The received power greatly depends on propagation distance, but also on multipath interference, which is why σ_{rdm} is multipath-sensitive. The systematic phase bias ϕ_b is defined as the difference between the ideal LOS phase ϕ_1 and the full received phase ϕ_{full}:

$$\phi_b = arg(s_1^2) - arg(s_{full}) = \phi_1 - \phi_{full} \tag{4.13}$$

The phase bias obviously depends on multipath behaviour. In phase space, the two error contributions σ_{rdm} and ϕ_b can be interpreted, respectively, as a scaling and translation operation on an ideal phase measurement distribution. Indeed, σ_{rdm} represents the width of the measurement error distribution, and the bias ϕ_b represents the center of this distribution; compared to the LOS ideal measurement; the true measurement will thus be translated by ϕ_b and scaled to a width of σ_{rdm}. Assuming Gaussian behaviour for the measurement process, each antenna j will, hence, present a measurement distribution ϕ_j following a normal law:

$$\phi_j = \mathcal{N}(\phi_b, \sigma^2_{rdm})$$

These considerations can be applied in the phase-localization scheme presented in the previous section via a multi-antenna phase distribution.

Let us define the scaling matrix S and the translation vector T as follows:

$$S = \begin{bmatrix} \sigma_1 & 0 \\ 0 & \sigma_2 \end{bmatrix}$$

$$T = \begin{bmatrix} \phi_{b1} & \phi_{b2} \end{bmatrix}^\top$$

The entries of S originate from Equation (4.12) and the entries of T from Equation (4.13). They correspond to the values of phase random error and phase bias measured by each antenna (N_a=2 in this simple scenario). Note that the phase random deviation values σ_j are different for each antenna for geometrical reasons; each antenna is in a different location, hence, the multipath and radiation patterns do not yield the same error values. The scaling S in phase space allows for a definition of the phase covariance matrix C_ϕ :

$$C_\phi = S \cdot S^\top$$

C_ϕ can be used in the singular value decomposition to compute the displacement error eigenvectors via the displacement covariance matrix C_r (see Equation (4.9)). The localization spot dimensions are, hence, fully described by the following covariance matrix in displacement space C_r :

$$C_r = (K^{-1})^\top C_\phi K^{-1} \tag{4.14}$$

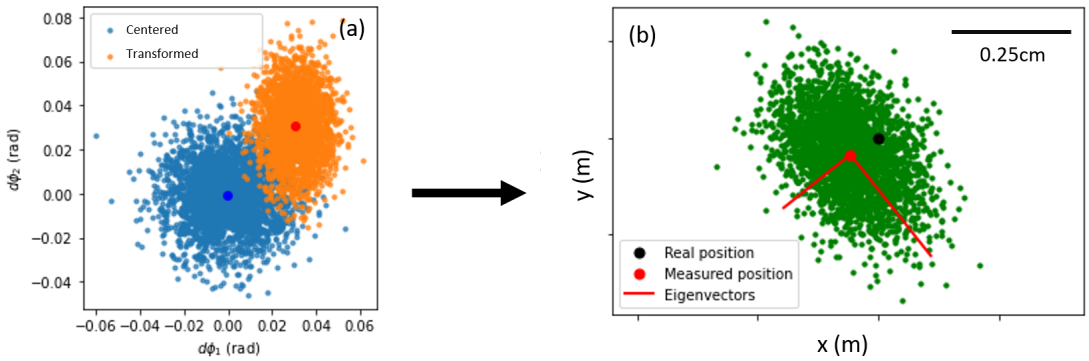

FIGURE 4.4 Schematic description of the matrix transformations in phase space towards real 2D space for a 2-antenna system. (**a**) Representation of the simulated multipath-induced phase measurement distribution (orange) compared to the previously assumed centered distribution (blue), highlighting the scaling S and translation T. The translation is illustrated by the shift between the center of the blue distribution and the center of the red distribution. (**b**) True space localization spot obtained by further transformation via the K^{-1} matrix. The antennas are not represented. The systematic bias is again illustrated by the shift between the real position (black point) and the center of the measured distribution (red point).

On the other hand, the translation T induced by the phase bias corresponds to a translation dr_b in displacement space, obtained by:

$$dr_b = K^{-1} \cdot T \tag{4.15}$$

Equations (4.14) and (4.15) represent our best attempt to model the deviation from an ideal LOS phase measurement, taking into account the various phase measurement errors, and the geometry of the system. Figure 4.4 presents a 2D schematic view of the measurement distributions from phase space to displacement space. We see that the phase distribution is scaled and translated in phase space, compared to the centered distribution that was set in Equation (4.8). In displacement space, this gives a specific localization spot with covariance C_r, translated from the true LOS measurement by vector dr_b. The specific values of C_r and dr_b are discussed in Section 4.4.

4.4 Harmalière Landslide Monitoring

In this section, we will discuss the specific case of the Harmalière landslide RFID system. After presenting the acquired data, the theoretical model will be applied to the real system geometry, then the localization results will be presented.

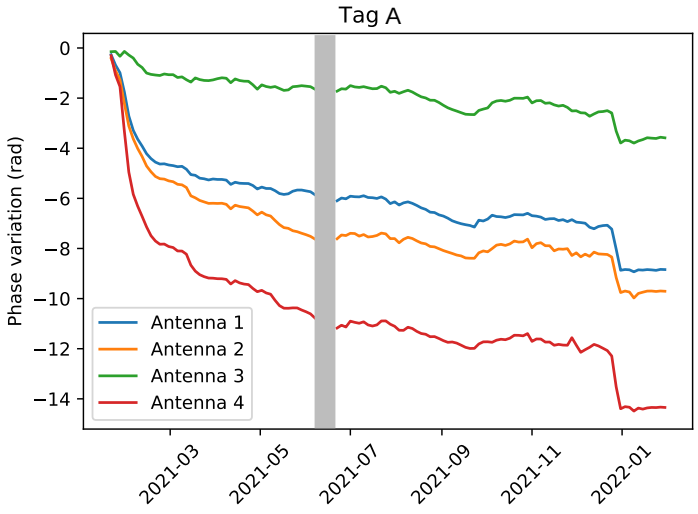

FIGURE 4.5 Unwrapped phase variation for tag A, measured by four antennas at a frequency f=865 MHz, from January 2021 to February 2022. The grey bar shows a period of missing data due to hardware failure. Data was directly available after replacement of the malfunctioning device.

Real Phase Data

Among the 32 tags installed in the field, 10 were read almost continuously by more than two antennas for 12 months (January 2021–February 2022). The rest of the tags yielded partial results that could not be used for 2D localization via the present scheme. Two main factors can explain the lack of readability of some tags, namely, the narrow horizontal directivity of the antennas (+/− 30° aperture) and signal attenuation—the furthest tags showed the lowest signal quality. Generally speaking, the tags placed 50 cm above ground showed worse results than those placed 1 m above ground, both in terms of data quality and localization accuracy. This observation corresponds to the above theoretical results (see Section 4.4 and Figure 4.7c), which tend to show that displacements close to the ground are subject to stronger multipath interference. This study will only show the tags read by at least two antennas during the whole period. The unwrapped phase measured during the January 2021–February 2022 time period is presented in Figure 4.5 for tag A. The data (70 measurements per day) were averaged over 24 h periods before applying the localization algorithm to mitigate the daily phase variations due to humidity and temperature. The missing values correspond to strong weather events that most likely depleted the battery of the acquisition system, or to hardware failures.

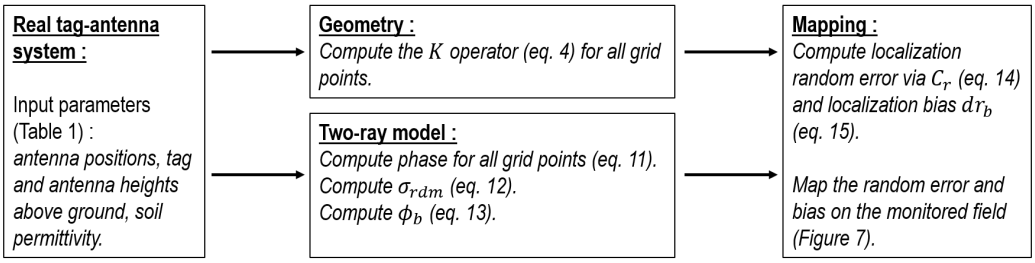

FIGURE 4.6 Schematic view of the workflow used to estimate the localization error and bias in the real-scenario Harmalière geometry.

TABLE 4.1 (Up) Geometrical parameters for the positions of the four antennas in the Harmalière setup. (Down) Values of the main variables used in the two-ray model (see Figure 4.3); the height of the station is relative to the ground at the same position.

Antenna No.	**x (m)**	**y (m)**	**z (m)**
1	0	0	0
2	0.018	−0.034	1.55
3	0.013	−2.608	0.256
4	−0.338	2.148	0.287

$h_{antenna}$ (m)	3
h_{tag} (m)	1
Ground relative permittivity	2.4

Application of the Model to a Real Geometry

Before presenting the localization results, we will first apply the previously developed model to the real system geometry. The workflow is presented in Figure 4.6, showing how the real parameters come together with the geometry and model to compute the localization error mapping.

We have set the model geometry according to Table 4.1, which corresponds to the Harmalière setup geometry. The number of antennas is now set to $N_a = 4$. The ground relative permittivity is set according to the literature for dry soils [ITU, 1992, Lytle, 1974], and the following results correspond to this dry soil scenario. In the case of a wet soil, we expect the relative permittivity to reach values around 25. In the model, this turned out generally to increase the phase error (and localization error) values by about 30%, which can represent millimeter to centimeter values depending on the context (see Section 4.4).

Random Localization Error of the Experimental Field

The previous developments (Equations (4.14) and (4.15)) have been applied to the geometry installed in the Harmalière landslide, as shown in Figure 4.7. A mapping of the random localization error (related to σ_{rdm}, Equation (4.12)) is shown in Figure 4.7a. We see that the lowest error is obtained when facing the antennas, which are oriented eastward. The plot is separated in two main areas, discriminated by the 2 cm random localization error value. This value was chosen because it reflects the target precision in our application.

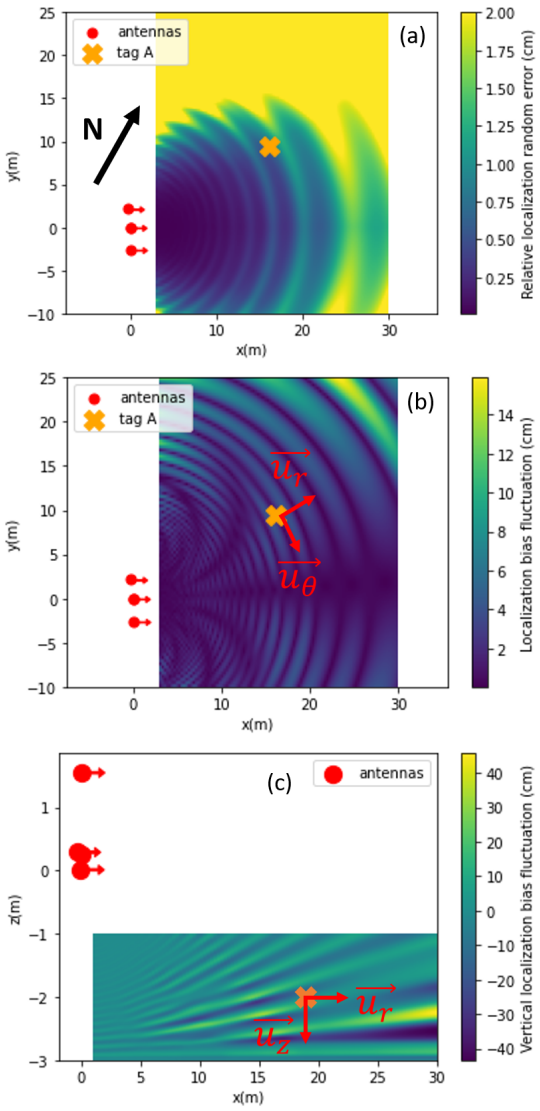

FIGURE 4.7 Mapping of the 2D localization error extracted from Equations (4.14) and (4.15), simulating the geometry of the Harmalière setup. The red dots represent the reader antennas, and the arrows show the principal antenna directions. The orange cross indicates the position of tag A. The vectors $(\vec{u_r}, \vec{u_\theta}, \vec{u_z})$ define the cylindrical coordinate system used later on. (**a**) The colormap shows the random localization error (maximum dimension of the localization spot) up to 2 cm, related to the phase random deviation σ_{rdm}. The localization bias is not shown. (**b**) Color-mapping of the systematic localization bias (related to ϕ_b) in the xOy plane shows oscillations with meter-order spatial frequency and increasing amplitude with distance from the measurement system. The random localization error is not shown. (**c**) Color-mapping of the systematic localization bias in the xOz plane, with higher oscillation amplitude and frequency. The ground is located at z= −3 m.

Systematic Localization Bias of the Experimental Field

The systematic localization bias (related to ϕ_b, Equation (4.13)) presented in Figure 4.7b,c is not to be understood as a raw localization error, but as a varying bias when moving in space; the interference between LOS and the reflected signal changes with tag position.

To better understand the effect of the multipath-induced phase bias on 3D displacement measurements, we propose to consider the typical case of a 1 m displacement along a given spatial direction, starting from the position of tag A. The symmetry of our experiment being mainly cylindrical, we consider a cylindrical coordinate system with its central axis in ($x = 0$, $y = 0$). For this displacement, we compute the localization bias fluctuation, and project it on every space direction (along $\vec{u_\theta}$, $\vec{u_r}$, $\vec{u_z}$) to obtain an amplitude value. The displacement length of 1 m was chosen both because it encompasses about one phase bias cycle, and because it corresponds to the actual displacement we measured in the real landslide scenario (see next section).

Table 4.2 reports the simulated localization bias amplitude in the three space directions, together with real error measurements that were performed on field.

- The direction that produces the least bias variation is a $\vec{u_\theta}$ displacement, which corresponds to the quasi rotational symmetry of the system.
- A horizontal displacement along $\vec{u_r}$ yields a small localization error. This confirms previous studies and demonstrates a centimeter precision for the RFID technique in the horizontal plane [Le Breton et al., 2019].
- A vertical displacement along $\vec{u_z}$ undergoes several strong bias oscillations (Figure 4.7c). The subsequent localization error is a cumulative effect of both the strong multipath interference and the small vertical aperture of the measurement system.

These results tend to show that vertical localization in the current localization scheme cannot be performed with precision. The multipath effect, along with the high system sensitivity in this direction, yield a very high localization bias. This is why we will not present Oz localization results in the following section. This model highlights the importance of the geometrical features of the system, such as antenna position and spacing, tag height and direction of displacement.

TABLE 4.2 Direction-dependent localization bias in the 3 directions (cylindrical coordinates), for a typical 1 m displacement. Each column corresponds to a different direction of displacement. Each line represents the localization bias amplitude along a certain direction, during the 1 m displacement. The *values in italic* correspond to field experiment localization bias measurements.

Dir. / **Bias**	$\vec{u_\theta}$	$\vec{u_r}$	$\vec{u_z}$
max. $\vec{u_\theta}$ bias	<1 cm	<1 cm (*1 cm*)	10 cm (*20 cm*)
max. $\vec{u_r}$ bias	1cm	1cm (*1 cm*)	2 cm (*15 cm*)
max. $\vec{u_z}$ bias	1cm	<1 cm (*5 cm*)	70 cm (*110 cm*)

Surface Displacement Monitoring Results

In this section, we present the experimental localization of the tags in the Harmalière landslide. We first focus on the 2D localization of one specific tag (tag A) in Figure 4.1, then we recapitulate on the whole setup and discuss the results.

2D Relative Displacement for One Tag

The 2D displacement of tag A, computed from the radial displacements using multilateration and data from the four antennas (see Equation (4.3)), is shown in Figure 4.8 against reference tacheometer position measurements. The xOy results are in good agreement with the reference points. Note that, for stable phase periods (for example July 2021), the localization algorithm yields very stable results with a centimeter scale variability, which is in agreement with the theoretical localization error presented in Figure 4.2. This correspondence between theory and experiment during stable periods is observed for several tags, further validating the measurement error model. Note that Figure 4.2 does not present any phase bias results, but focuses only on measurement random deviation (dimensions of the localization spot).

2D Localization for All Tags

Figure 4.9 shows an overview of the xOy displacement norm measured by the RFID-phase for all available tags during the measurement period. The total displacement is also shown for every tag in

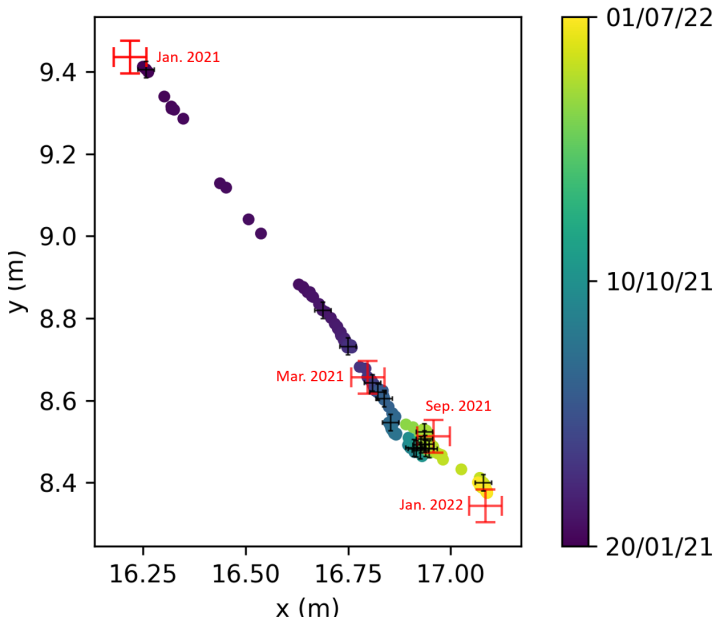

FIGURE 4.8 RFID localization in the xOy plane, using phase data for tag A (Figure 4.5). The total displacement is about 1.6 m. The color plot represents the time evolution of the RFID relative localization. The red crosses represent the reference measurements using a tacheometer, with an estimated error of about 4 cm. The tacheometer measurement of March 2021 is set as an absolute reference for relative localization. The black crosses correspond to the estimated random error bars for TD-phase localization (calculated via the model developed in Section 4.4).

Table 4.3. All RFID localization results fit with reference measurements, notably for displacements greater than 1 m. The steep displacement increase in January 2022 concerning tags 51, 4e and A, was confirmed by tacheometer measurement. This rapid and localized deformation generated cracks and a landslide retrogression of about two meters in this area. A south-east tendency is clearly validated and corresponds to the landslide main direction, as can be seen in the qualitative vector mapping in Figure 4.10, with various displacement amplitudes depending on tag location. This opens the way to 2D spatio-temporal monitoring of the landslide surface, offering the possibility to better understand the physical mechanisms at the origin of the landslide activation and propagation, and to build new early warning monitoring systems.

Discussion

In this section we briefly discuss some of the results presented in this paper, as well as future development of the RFID localization system.

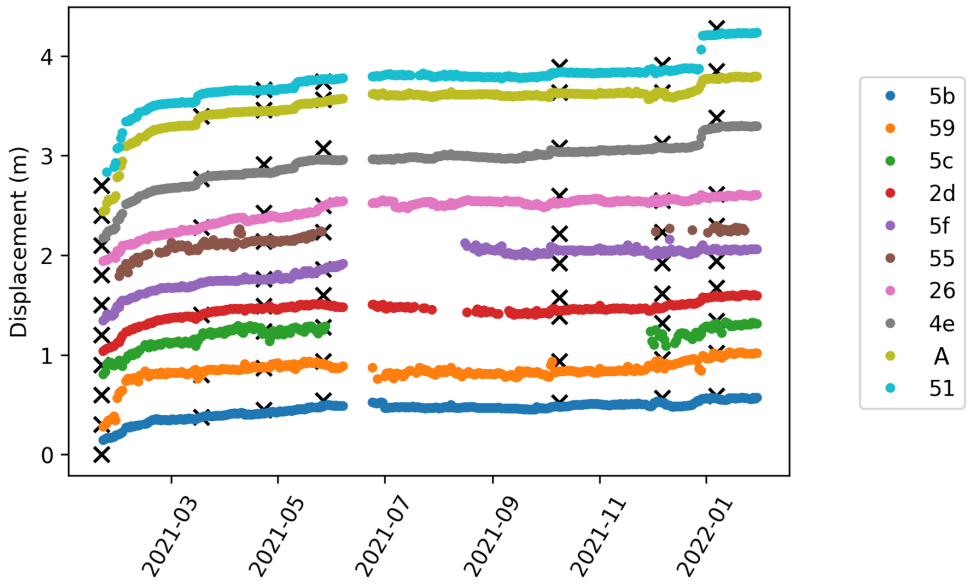

FIGURE 4.9 Cumulative 2D displacement norm for each tag, with reference measurements performed via tacheometer (black crosses). An offset was added to every plot to increase readability. The total displacement values are given in Table 4.3.

TABLE 4.3 Total 2D displacement norm for all presented tags computed from the RFID phase, from January 2021 to February 2022. The reference is computed from the tacheometry measurements, with an estimated error of ±4 cm.

Tag	**51**	**A**	**4e**	**26**	**55**	**5f**	**2d**	**5c**	**59**	**5b**
Total disp (m)	1.54	1.37	1.20	0.81	0.75	0.85	0.69	0.67	0.74	0.56
Reference (m)	1.57	1.45	1.28	0.81	0.79	0.74	0.77	0.74	0.72	0.59

Localization Error and Reference Measurements

In the context in which RFID localization was performed, absolute reference localization at a centimeter level was a complicated task. For practical reasons, reference positions taken via GPS were not sufficiently accurate to be compared to the RFID localization results. This is why tacheometry was used, which is a relative localization method. A landslide is an ever-changing environment, and using absolute references such as trees or antennas involves several sources of error. For this reason, the tacheometer uncertainty given in Table 4.3 is ±4 cm. As has been described in previous reports [Le Breton et al., 2019], RFID phase outdoor localization can outperform the reference measurements.

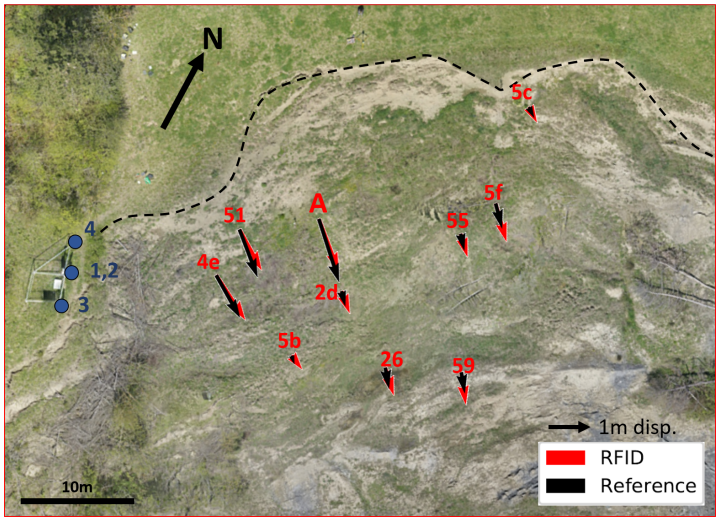

FIGURE 4.10 Vector mapping of the total 2D displacement for all available tags from January 2021 to September 2021. The scale is modified for clarity with a 1 m displacement reference (black arrow). The red arrows represent the displacement estimated from the RFID measurements, and the black arrows represent the displacement computed from reference measurements. The blue points numbered 1 to 4 correspond to the reader antennas.

Discussion on Antenna Position

The above model (Section 4.4) is a tool for optimizing the antenna positions in a given terrain to minimize localization errors originating from both multipath and geometry. We performed calculations for several geometrical cases in a plane xOy geometry, searching for the lowest random deviation in the monitored zone. As a general rule, we conclude that surrounding the field with antennas yields the best accuracy (lowest localization random deviation). For example, if four antennas are spread around the Harmalière field, the horizontal random localization error is expected to reduce to 1 mm.

Such setups are not always possible in real-environment operational situations—the experimental setup obviously has to be designed taking into account the operational constraints and priorities. In cases where a portion of the field is inaccessible, for example, the distance between antennas (system aperture) should be maximized to obtain the lowest random deviation. This guideline has limitations, such as cable length or station cost, hence the final setup will generally be a compromise between precision and station/maintenance cost. Note that other localization methods, such as angle of arrival techniques [Azzouzi et al., 2011, Faseth et al., 2011] rely on different system geometries and will not lead to the same optimal antenna disposition. The guidelines provided here only apply to a relative

displacement scheme; absolute positioning is a different matter which we do not discuss here.

Perspective for Improving Data Availability

In this investigation, the tags that yielded only partial data (i.e., less than two antenna readings, long time periods without data) were not used, although more complex data assimilation techniques could be of use [Sun and Deng, 2004, Sarkka et al., 2011b]. Exploiting both the knowledge of the landslide mechanics and the redundancy of information that the system yields could allow tag monitoring even in partial data scenarios, which are a common issue in outdoor environments. Such techniques will be implemented in future work.

4.5 Conclusions

We have derived a phase-based 2D localization error theoretical model that allows for error estimation in a scenario of two to four static interrogator antennas, taking into account the specific setup geometry. The model is based on both the sensitivity kernel of the measurement system and a two-ray propagation model (multipath). Under certain conditions, this model confirms the ability to track centimetric ground displacements. The in-plane horizontal measurements demonstrate much better accuracy than the out-of-plane vertical measurements, due to the preferential horizontal antenna distribution, and to ground-reflection multipath interference.

A set of RFID tags was placed on an active landslide and phase measurements were performed over several months to monitor the tags' displacement. The results show a clear south-east displacement of about 1 m in the horizontal plane over the monitored area. The presented method, inspired by the time-difference phase-difference scheme, has shown very good results for the monitoring of relative displacements in 2D at the centimeter scale. The monitoring of landslides using RFID technology was demonstrated to be a viable solution, with centimeter-scale accuracy over large periods of time. A further step in large scale monitoring could be to deploy a moving antenna (SAR) over greater lengths, and to implement a data assimilation approach to increase data availability.

The passing seasons are remarkably marked on the Harmalière landslide. This is very much due to the vegetation, the weather, but also the clay itself.

Chapter 5

Landslide surface deformation studied by dense RFID arrays, with multi-method investigation

5.1 Abstract

Radio-Frequency Identification (RFID) shows great potential for earth-sciences applications [Breton et al., 2021], notably in landslide surface monitoring at high spatio-temporal resolution [Le Breton et al., 2019] with meteorological robustness [Le Breton et al., 2017]. Ten 865MHz RFID tags were deployed on part of a landslide (Harmalière) and continuously monitored for 20 months by a station composed of 4 reader antennas. 2D relative localization was performed using a Phase-of-Arrival approach [Nikitin et al., 2010, Charléty et al., 2022b], and compared with optical reference measurements. The spatio-temporal accuracy of the method allowed for a thorough exploration of the landslides mechanisms during a 20-months period of activity. Laplacian clustering was applied to the RFID data and groups of tags with coherent behavior were identified, allowing a fine description of the kinematic motion of the landslide blocks and various mass transfer mechanisms. Different deformation zones were highlighted on the monitored zone. Coupled to hydrological and ambient-noise seismic observations, displacement

measurement allows for an interpretation of the seasonal behavior of the Harmalière landslide. The multi-method observations provide precious insights on the intricate mechanisms of the landslide.

5.2 Introduction

In a context of intensified climate extremes and ever-developing urbanization, landslide monitoring and early warning are nowadays a growing aspect of natural risk assessment and mitigation [Rohan et al., 2023, Dille et al., 2022]. Slope destabilization events cause thousands of casualties, and tens of billions of euros losses every year [Froude and Petley, 2018]. The increased occurrence of such natural hazards is putting at risk more and more unprepared regions [Cui et al., 2019]. In order to inform and warn local communities, Landslide Early Warning Systems (LEWS) are commonly used as risk mitigation strategies [Pecoraro et al., 2019]. These systems generally monitor surface deformation, groundwater level or precipitation. In recent years, geophysical methods have shown potential for monitoring hazardous objects, and investigating their mechanical or hydrological properties. These methods stand out as complementary compared to more classical direct-quantity measurements [Le Breton et al., 2021]. In particular, an analysis from [Larose et al., 2015] revealed clear precursory geophysical signals, from days to hours before landslide failure.

The complementarity of multi-method approaches provides both a better early warning capacity, and a deeper understanding of the various processes impacting landslide activity. In that regard, multi-method monitoring is usually seen as the most comprehensive approach, taking advantage of all possible sources of information [Casagli et al., 2023, Fall et al., 2006]. Moreover, the datasets from multi-method observation provides ideal insights in the kinematic mechanism of active landslides. Understanding the role of water, its impact on the soil mechanical properties, and the resulting surface deformation, allows for a detailed analysis of the landslide processes. Schulz *et al.* [Schulz et al., 2017] studied the long-term kinematics of a large landslide using InSAR, extensometer data, and pore-water pressure measurements, noting the presence of distinct kinematic elements within the landslide. Lacroix *et al.* [Lacroix et al., 2019] analyzed the kinematics of landslides in Peru using image correlation and identified a self-triggering mechanism. Kanungo *et al.* [Kanungo, 2019] provided a comprehensive international review of landslide monitoring and prediction instrument setups. [Delacourt et al., 2007] reviewed the satellite- and ground-based methods for landslide surface displacement mon-

itoring. Casagli et al. [Casagli et al., 2023] remind that all methods have advantages and limitations, that depend on local parameters such as the size of the investigated zone, the nature of the landslide, and the level of risk. Hence the integration of various complementary monitoring systems is often best. In this study we will focus on retrogressive, slow-moving clayey landslides, which are a vast research topic [Lacroix et al., 2020] as well as a concerning natural hazard [Mansour et al., 2011, Handwerger et al., 2019].These landslides exhibit a variety of deformation behavior, complex and intricate mass transfer mechanisms leading to retrogression that are still under investigation [Fiolleau et al., 2021]. Understanding the kinematics of landslides and monitoring their surface displacements, are crucial for assessing landslide behavior. In this study we propose to investigate both surface deformation through RFID, hydrological quantities and subsurface behavior through ambient noise variation.

Radio-Frequency Identification (RFID) technology has emerged as a valuable tool for monitoring landslide surface displacements with centimeter accuracy and oversampling in both space and time [Le Breton et al., 2022]. After validation against outdoor environmental conditions [Le Breton et al., 2017], one-dimensional RFID measurements were performed on the Pont-Bourquin landslide (Switzerland) over a 6-months period [Le Breton et al., 2019]. The centimeter accuracy of the RFID-phase tracking method was demonstrated against extensometer and total station reference measurements. Preliminary results showed the strong link between landslide hydrology and surface deformation, and a predictive displacement model based on rainfall measurements was proposed [Le Breton, 2019]. The method was recently improved with two-dimensional monitoring [Charléty et al., 2022b] as well as data processing enhancement [Charléty et al., 2023a, Charléty et al., 2023b]. The extension to 2D provides precious information on the directionality of landslide deformation, and the spatial distribution of the deformation activity. Notably the different active blocks constituting the unstable zone can be identified, along with the triggering mechanism. Combined with the spatio-temporal oversampling brought by RFID, this yields new landslide-kinematics monitoring capacities.

Since a decade, methods based on seismic ambient noise have proven their potential in monitoring slope instabilities, such as rock glaciers [Guillemot et al., 2020] and clayey landslides [Le Breton et al., 2021]. By correlating ambient noise recordings from a pair of sensors, the subsurface in-between them can be surveyed with a high temporal resolution by extracting two main observables. First, the rel-

ative change in seismic surface wave velocity (dV/V) provides a direct proxy for elastic properties (stiffness and density) [Larose et al., 2015]. Secondly, the correlation coefficient CC informs on the coherence of diffused waves propagating between sensors, thus sensitive to cracks and fluid infiltration through the surveyed volume [Thery et al., 2020, Guillemot et al., 2020]. Due to the dispersion of surface waves, these seismic observables are frequency-dependent, allowing to probe the subsurface at different depths. In the Harmalière landslide, [Fiolleau et al., 2020] already observed a decrease in CC associated with successive rainfall events. This decrease was observed from higher to lower frequencies until the failure event, suggesting a mechanism propagating at depth. dV/V also changed rapidly before the failure, although no clear trend emerged. Voisin et al. [Voisin et al., 2017] demonstrated an excellent agreement between the water table and dV/V on a deep seated landslide, due to poroelastic effects. dV/V is also sensitive to various environmental forcings, such as temperature, rainfall, atmospheric pressure [Le Breton et al., 2021], and even snowfalls [Guillemot et al., 2021]. Additionnally, microseismic events detected by seismic monitoring can be combined to become a proxy for estimating surface deformation and a precursory signal for early warning systems [Tonnellier et al., 2013, Lacroix and Helmstetter, 2011]. Compared to deformation-measuring tools, ambient noise monitoring provides information on the damaged volume, with sensitivity to in-depth activity notably due to hydrological processes. The surface to volume interaction is thus ideally investigated by the complementary surface displacement and ambient noise data.

Hydrological parameters have long been used as a landslide monitoring tool. Iverson et al. [Iverson and Major, 1987] proposed to study the rainfall and groundwater flow to understand the landslide dynamics. They concluded that landslide motion was regulated by the near-surface hydraulic gradients and by waves of pore pressure caused by intermittent rainfall. Van Asch et al [Van Asch et al., 1999] suggest that failure conditions in shallow landslides can occur when at a critical depth, the moisture content in the soil becomes close to saturation, resulting in a considerable reduction of soil strength. Deeper landslides (5–20 m depth) are triggered by positive pore pressures on the slip plane induced by a rising ground water level. Bitelli et al. [Bittelli et al., 2012] examinated the interplay between soil hydrological and mechanical properties, showing that the instrumented clayey landslide was triggered in consequence of changes in soil suction stress. Rosone et al. [Rosone et al., 2018] proposed a model to account for landslide displacement based on pore water variation. They manage to establish a quantita-

tive correlation between cumulative rainfall, pore water pressures, and the activity of the landslides in a complex soil formation. As was shown by both RFID [Le Breton et al., 2019] and ambient noise [Voisin et al., 2017], the hydrology of the unstable terrain is a critical aspect that guides landslide activity. Rainfall and water-table monitoring are thus very informative to identify and understand the surface and volume processes leading to landslide activity.

The combination of methods integrating hydrological, ambient noise and surface displacement data opens up new possibilities for probing the inner mechanisms of landslides, as well as improving early warning systems and emergency logistics aimed at securing unstable zones. This study aims to demonstrate the benefits from a multi-method approach incorporating RFID-based surface displacement, combined with seismic noise and hydrogeological observations, in order to highlight the processes involving the dynamics of a landslide. To our knowledge, this is the first usage of 2D-RFID for probing the kinematic behavior of landslides.

5.3 Materials and Methods

Presentation of the Harmalière landslide

Figure 5.1 presents an aerial view of a portion of the Harmalière landslide, located in the Trièves area, 30km South from Grenoble (France). Trièves is a sedimentary plateau formed by Quaternary clays and alluvial material deposited during the Würm period [G., 1973]. The thickness of the glaciolacustrine clays varies from 0 to 200 m [Jongmans et al., 2009]. The Harmalière landslide is southeast oriented, 400 m wide at the top, narrowing to 150 m at the toe. It develops from an altitude of 735 m (above sea level), down to the Monteynard Lake (480 m), over a distance of about 1.5 km. It can be classified as an "active very slow translationnal earth slide - earth flow". It was abruptly activated in 1981 and remained active ever since, with new peaks of activity in 2016 and 2017. It is subject to several research projects. In the recent years, [Fiolleau et al., 2019] exploited UAV-LiDAR imagery to monitor surface deformation as well as to characterize the soil type ; multi-method investigation notably seismic and hydrology was performed [Fiolleau et al., 2021] ; and [Lacroix et al., 2018] used optical satellite data to detect precursory landslide motion. Ambient noise measurements allowed [Bièvre et al., 2011] to study the paleotopography of the landslide bedrock.

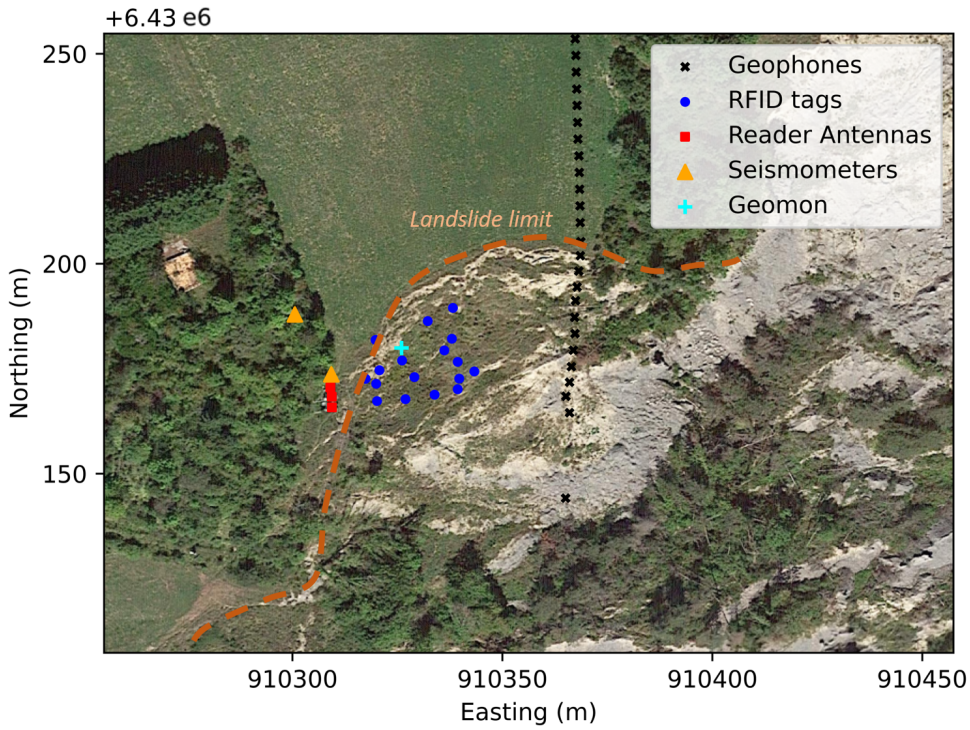

FIGURE 5.1 Description of the instrumented site on the Harmalière landslide and the different available sensors. The black crosses × represent geophones positions for the temporary seismic prospection survey. The orange triangles ▲ represent the permanent seismometers. The blue dots • show the position of the RFID tags, and the red squares ▪ are the reader antennas. The geomon is represented by a cyan cross +. The landslide scar is depicted as a brown dashed line.

RFID setup and analysis

The RFID monitoring setup is extensively described in [Charléty et al., 2022b]. The autonomous interrogation setup, consisting of four cross-polarized antennas and an RFID reader (Impinj) powered by solar/wind energy, reads the set of tags placed in the field at a rate of one measurement every 20 minutes. The Phase of Arrival [Nikitin et al., 2010] is recorded and used to recover the relative radial displacement for each tag-antenna couple. Specific concerns about phase processing in outdoors and long-term environments, are discussed elsewhere [Charléty et al., 2023b, Charléty et al., 2023a, Le Breton et al., 2017]. An inversion is then performed using the four radial distance measurements, in order to compute the 3D trajectory of the RFID tags over time, and reconstruct the landslide surface displacement. In

practice the vertical estimate presents much higher uncertainties than in the horizontal plane, notably due to multipath effect and antenna system aperture.

Along with the RFID relative displacement measurement, one permanent Geomon "low-cost" GNSS receiver (www.infrasurvey.ch) was installed on the field [Fiolleau et al., 2021], and provided absolute positioning starting from April 2021. In addition to validating the RFID displacement, the Geomon provides vertical displacements that are generally discarded in RFID [Charléty et al., 2022b]. Conversely the RFID deployment provides a dense spatialization of the landslide horizontal movements.

Velocity spectral clustering. To further synthesize the RFID results from n_{tag} tags, we propose a spectral clustering approach based on a tag distance-velocity metric. This will help identify coherent groups of tags, and hence coherent landslide sectors following the concept of kinematic elements presented elsewhere [Schulz et al., 2017]. For a given period of time, we construct an $n_{tag} \times n_{tag}$ similarity matrix, where every tag couple (i, j) has a score $s_{i,j}$:

$$s_{i,j} = \frac{Cov(v_i, v_j)}{\sigma_{v_i} \sigma_{v_j}} \times w_{i,j}$$

With v_i and v_j the computed velocity for tags i and j respectively, σ_i and σ_j the standard deviation of the velocity series. $w_{i,j}$ is a normalized distance score that is related to the distance $d_{i,j}$ between both tags and to a typical distance d_0 :

$$w_{i,j} = e^{-d_{i,j}/d_0}$$

In our scenario, d_0 was set to 15 m as a typical decay distance. This way, tags that are too far from each other will not be correlated.

In practice $s_{i,j}$ is computed as the norm of a 2D vector, with correlation coefficients along the Ox and Oy directions as coordinates. We run a spectral clustering algorithm [Von Luxburg, 2007] based on optimal discretization [Stella and Shi, 2003] implemented using a publicly available Python package [Kramer and Kramer, 2016]. Fitting the similarity matrix s provides k groups of tags with coherent velocity profiles. For this first implementation, k was empirically set to 2, as the instrumented zone showed two main sectors. Further improvements could include an automatic estimation of k, as explained in [White and Smyth, 2005]. This would be especially useful in the context of a system

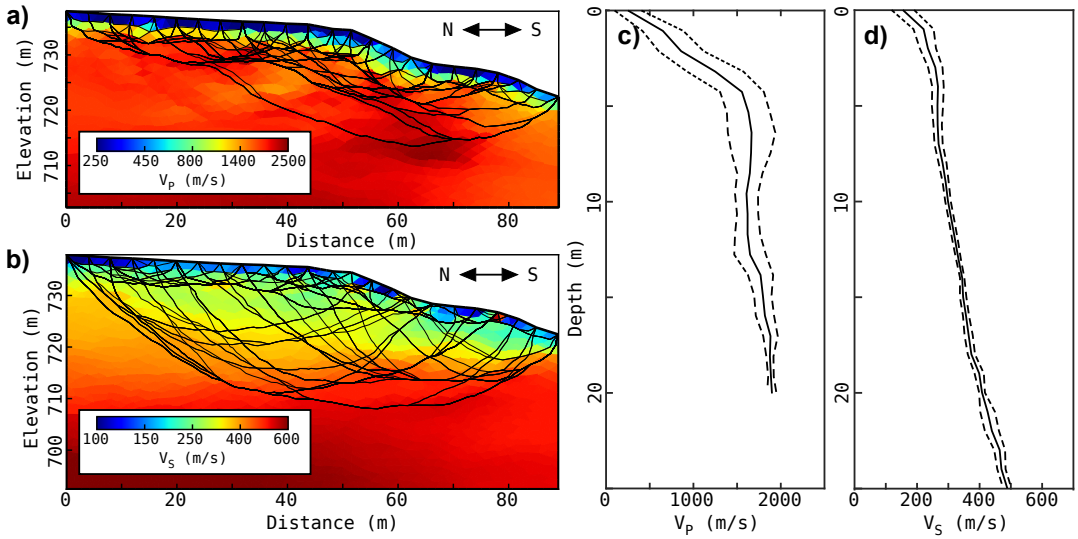

FIGURE 5.2 Left : Two-dimensional V_p (a) and V_s (b) profiles computed from the active seismic tomography experiment. Interpretation should be limited to zones crossed by seismic rays. Right: One-dimensional V_p (c) and V_s (d) profiles used for sensitivity kernel computation, with standard deviation envelope as a dotted line. *Credit : Gregory Bièvre.*

Parameter	Sensors (#)	Spacing (m)	Shots (#)	Data Points (#)	Iterations (#)	χ^2	RRMSE (%)
V_p	24	4	9	193	6	0.5	4.56
V_s	24	4	9	198	12	1.4	3.58

TABLE 5.1 Acquisition settings for the V_p and V_s profile inversion, and corresponding statistical results of the geophysical profiles. See [Bièvre et al., 2021] for more details.

up-scaling, where many more tags could be deployed.

Active Seismic tomography

A seismic profile was acquired using the same method described in [Bièvre et al., 2021], based on active compressional (P) and shear (S) waves recording using a series or vertical-horizontal geophones. The positions of the 24 geophones are shown in Figure 5.1, with a spatial sampling of 4 m. The detection of first-arrival times allowed for inversion of V_p and V_s profiles, as shown in Figure 5.2. The acquisition parameters are summarized in Table 5.1. Inversion results provide satisfactory statistical results for both χ^2 and relative root-mean-square error (RRMSE). The RRMSE informs on the fit between true measurements and forward model values produced by inversion. The χ^2 value reflects the correspondence between experimental error and model misfit.

Note that the seismic profile inversion should not be interpreted in-depth, in zones not illuminated

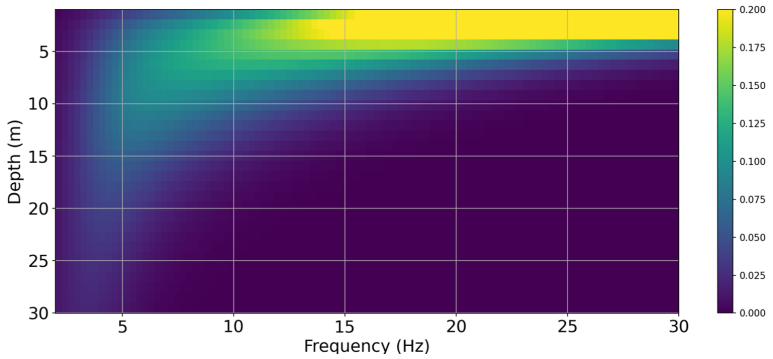

FIGURE 5.3 Sensitivity kernel (dimensionless) of the fundamental mode of Rayleigh surface waves, computed from 1-D V_p and V_s profiles, between 2 and 30 Hz. *Credit : Antoine Guillemot.*

by seismic rays. Similarly, the V_p and V_s one-dimensional profiles are computed as an iso-depth mean of the 2D-profiles, with no value below the lowest ray trajectory.

Ambient noise monitoring

We used seismic data from a pair of seismometers (see Figure 5.1) located near the landslide scar. Two Lennartz LE-3D/5s MkIII seismometers were used, with an eigenfrequency of 0.2 Hz, protected in a waterproof case. We used a CENTAUR-6 digitizer at a sampling rate of 200 Hz, connected to the same central setup as RFID measurements. After pre-processing steps (spectral whitening and clipping similar to those described in [Guillemot et al., 2020]), both relative change in velocity dV/V and its correlation coefficient CC were estimated by applying the stretching technique to cross-correlations of vertical components. We used a time window between 0.3 and 1.0 s to select only the coherent coda part of the cross-correlations, that is more sensitive to elastic changes of the medium and less sensitive to the seismic sources variability than ballistic waves. The cross-correlations were filtered at several frequency bands, but we finally selected only the 6-9 Hz frequency band that seems to provide stable and significant results. Assuming the coda part of vertical cross-correlations is mainly composed of Rayleigh waves, we deduced from their sensitivity kernel that this 6-9 Hz frequency band is most sensitive to elastic changes occurring between 1 and 10 m depth (see Figure 5.3).

Hydrological measurements

In order to measure the water table level, a piezometer was installed close to the headscarp of l'Harmalière, 300 m East from the field shown in Fig. 5.1. Additionally, rainfall and snow-height data from the La Mure station (10 km east from l'Harmalière) were used, provided by Meteo France. The meteorological data was resampled by summing over 24 h for simplicity.

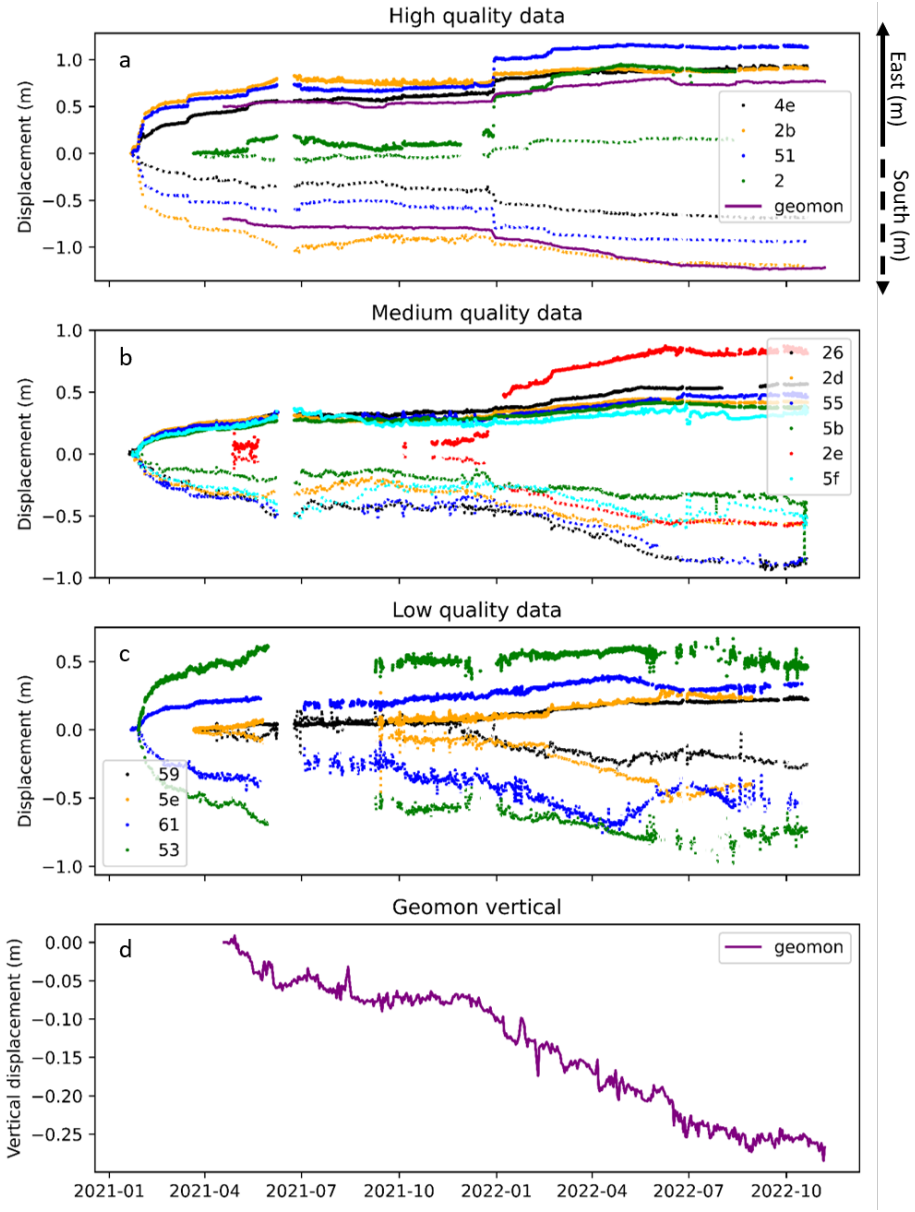

FIGURE 5.4 (a,b,c) Global displacement summary for all tags on the 2021-2022 period. Easting is in full scatter-plot, Northing in dotted line. For clarity, the three plots are arbitrarily selected based on subjective data quality assertion. (d) Vertical displacement estimated using the Geomon device.

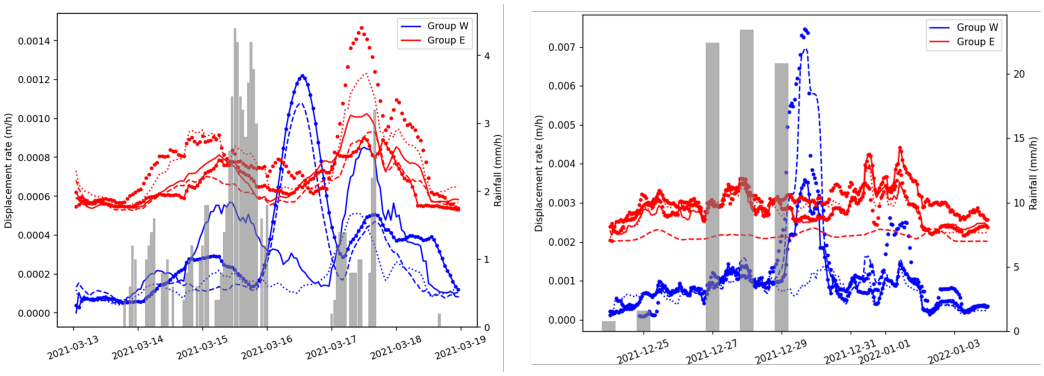

FIGURE 5.5 Velocity series for the march 2021 (left) and december 2021 (right) periods. The colors indicate the clustering groups (Figure 5.6) : W in blue, E in red. The grey bar-plot shows hourly rainfall.

5.4 Results and discussion

RFID displacement results

Figure 5.4 shows displacement results for the whole set of tags. The tags are separated by data quality in order to improve readability. The proposed coherent groups of tags will be presented later. Note that some tags are moving towards the antenna, although a majority are moving away. The high variability in data quality is mainly attributed to RF communication : tags that are further, or in RF-shadowed zones, or out of an antenna's main lobe, show lower quality data. This is related to the estimated localization error computed in [Charléty et al., 2022b], caused by multipathing, distance attenuation and antenna radiation pattern. Generally speaking, the variance is higher in the North-south direction (lower antenna system aperture) as expected from former theoretical studies [Charléty et al., 2022b, Charléty et al., 2023b]. The displacement series exhibit various activation phases, with specific tag groups sharing similar behavior. For example tags 2b, 4e and 51 share most of their displacement features. Two main activation periods stand out : January to May, both 2021 and 2022, which are linked to intense precipitation events and snowmelt. Following both these events, a slow creep occurs at rates of about 2 cm/month, with accelerations strongly correlated to rain events. The Geomon data show coherent results when compared to RFID, and provide valuable vertical displacement estimation. Downwards displacement is observed consistently over the measurement period at a rate of about 3 cm/month, with a stabilization during autumn 2021 and 2022. Figure 5.5 presents the velocity series for two selected periods in March and December 2021. The groups of tags (in

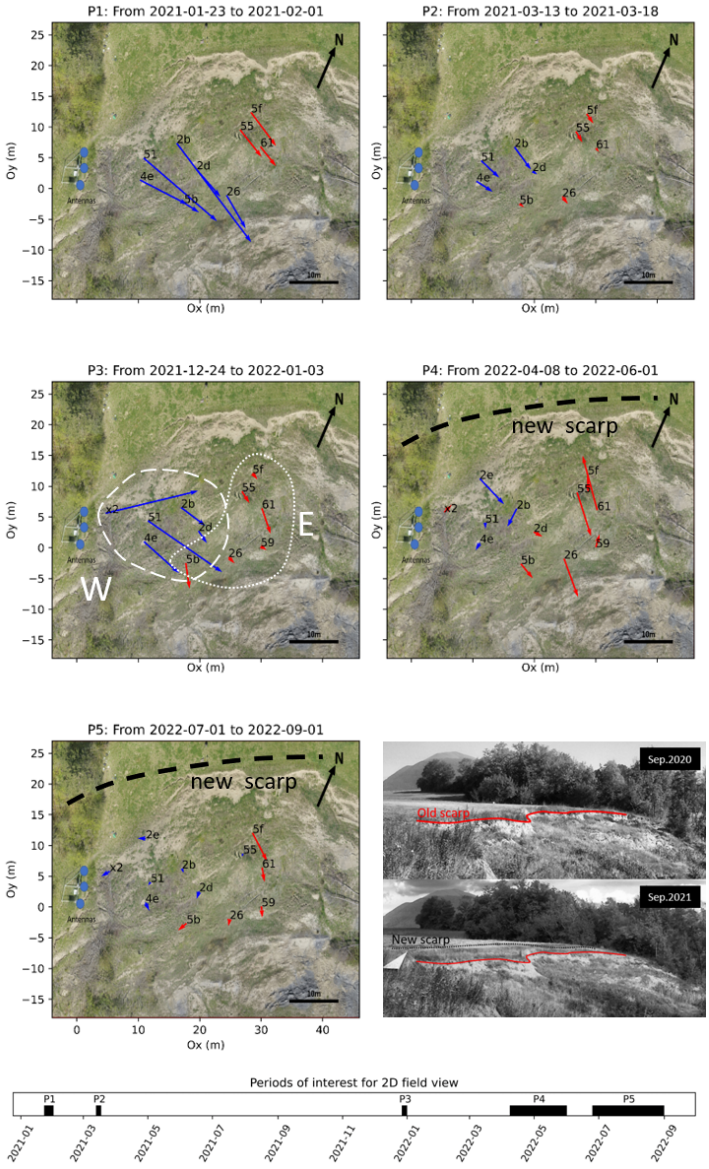

FIGURE 5.6 Displacement field for selected periods of time (P1 to P5), delimited in the bottom diagram. The vectors represent upscaled tag displacement, and the colors highlight the clustering results. Starting from April 2022, the approximate shape of the new scar is drawn in dotted line. In the last image (bottom-right), comparison of two photographs taken in September 2021 and 2022, with indication of the previous and new landslide scarp. On the December 2021 subfigure, the group attribution from Table 5.2 is illustrated.

color) were clustered based on the above-mentioned method, using the empirical number of 2 clusters. This illustrates the differential activity between groups of tags. Note that the clustering results do not

yield consistent groups over time, it is rather a matter of general tendency of certain tags to behave similarly. Two zones stand out for the majority of events : the most active western block (noted W), and the eastern lower zone (E), which is the flattest sector. In practice, zone E shows heterogeneity between the tags closest from the scarp (tags 5f, 55, 61) and the southernmost tags, notably during the 2022 scar opening. Based on clustering results, displacement series analysis and empirical judgement, we propose a broad attribution of tags to groups in table 5.2. Note that some tags belong to both groups, illustrating the complex and time-varying nature of surface deformation. This attribution is illustrated in Figure 5.6.

Concerning the March 2021 activation, the two groups show a different behavior. The successive acceleration phases are all linked to rain events. The E group shows peak velocities earlier than W. Regarding the December 2021 activation, the main deformation is represented by three tags in the W group, with peak velocities approaching 1 cm/h. On the other hand, most other tags feature a week-long slow creep. Figure 5.6 presents a series of 2D displacement fields, for time periods that were manually selected for their activity features. The clustering results are illustrated by the colored vectors. The method provides nearly-consistent clusters over time, despite the complex nature of surface deformation in this case. Nonetheless, the qualitative information provided by the clustering helps to identify specific active zones.

Multi-method observation results

Figure 5.7 summarizes multi-method observations spanning the 2021-2022 period. Concerning RFID, a synthetic cumulative displacement indicator is shown. This cumulative indicator is computed from the integration of average absolute velocities of the whole RFID group, which makes it monotonic. It can also be interpreted as the positive advancement on a curved (and averaged) trajectory, of the whole group of tags.

Hydrological information in Figure 5.7 is provided from the piezometer, precipitation and snow

Group	Tags
W	4e, 51, 2b, 5b, 2d
E	5b, 26 , 59, 61, 55, 5f, 2d

TABLE 5.2 Attribution of tags to a group showing coherent displacement over time. See Figure 5.6.

depth measurements, along with daily temperature measurements. dV/V and CC are shown as well for the $6-9$ Hz frequency band. We chose to focus on this frequency band because at these frequencies, surface waves probe a large and representative depth (Figure 5.3). The resulting dV/V are then related to depths where dynamic processes of the landslide are likely to occur. Note that the dV/V variation is relative to an averaged reference over the whole monitoring period.

Every RFID displacement is correlated to precipitation events, as well as every CC drop. In many cases, a surface activity is synchronous to CC degradation, either prior to the triggering (periods of activation 3, 5, and 7 in Fig. 5.7) or during deformation (2, 8). We observe that CC and dV/V variations are generally linked, either synchronously (1, 2, 4, and 8) or with a correlation change preceding the velocity drop (3, 5, and 6).

The dV/V series shows seasonal variations which are expected [Voisin et al., 2016], that correlate negatively with the water table variations. On a weekly time scale, the main features are variations in the range of 1-3% that can be related to shear stiffness or density changes. Most of those diminutions are synchronous to observed surface deformation. In some cases (6, 8), the dV/V drop precedes the surface velocity peak by a day or two. The seismic data from may 2021 was partly discarded, as the cross-correlation processing did not provide coherent results.

The landslide is small compared to the volume investigated by the seismic waves that constitute the coda [Guillemot et al., 2020], which integrates a variety of regions (solid ground, fractured material, high-density of tree roots, vadose and saturated zones). In such heterogeneous media, the damaged landslide surfaces represent only a fraction of the ambient noise information. Moreover the volume directly probed by the pair of sensors is only at a short distance above the landslide scar, and does not fully include the main slip surface. Hence the rather small observed variations related to landslide activity, compared to other study sites [Guillemot et al., 2020].

Figure 5.7 exhibits two types of dV/V drops. In the cases of February 2021 (event 1) and June 2022 (8), the sudden variation is quickly followed by a return to the preceding value. Conversely, other periods of degradation (2, 4, 6, and 7) are followed by a longer transient recovery. In February 2022 (7), a series of accelerations also shows that dV/V changes follow snowmelt and subsequent water table elevation (see Figure 5.9). This translates in a higher surface displacement that slows down when the water table goes back to normal, although at a higher displacement rate than previously. Concerning multiple selected accelerations (1, 3, 4, and 7), a typical scenario is observed : a (series of) precipitation

event(s) precede(s) a surface acceleration, which is closely followed by a dV/V drop. One or two days after the peak velocity, the precipitation impulse translates in a water table rise.

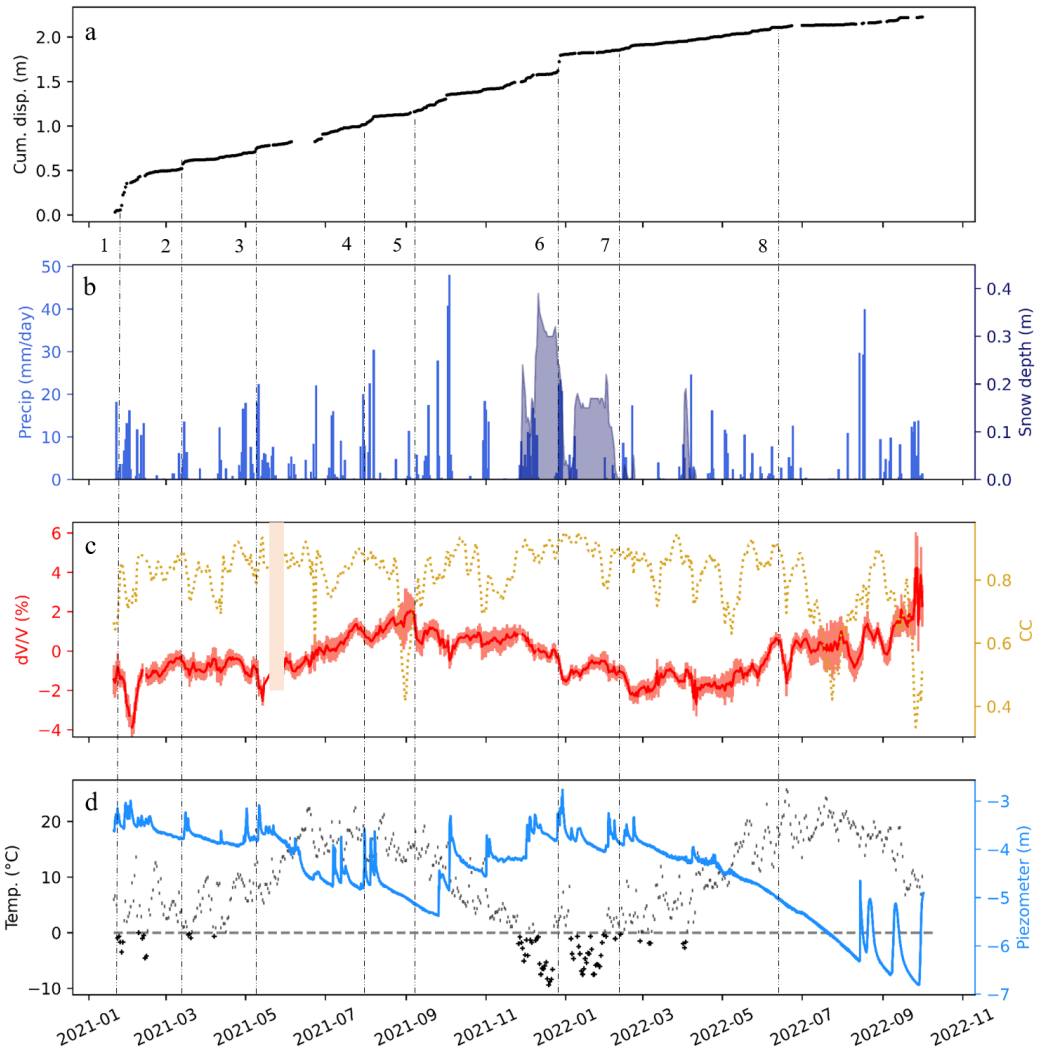

FIGURE 5.7 Multi-observable data series for the monitoring period. (a) Cumulative displacement indicator for the whole RFID field (described in section 5.4). (b) Daily precipitation and snow depth. (c) dV/V (in red) and CC (in yellow) for the 6-9Hz frequency band. (d) Daily temperatures (in black), with different markers for positive (|) and negative (+) temperatures, and water table level (in blue). Selected periods of activation are indicated by vertical dotted lines, numbered from 1 to 8.

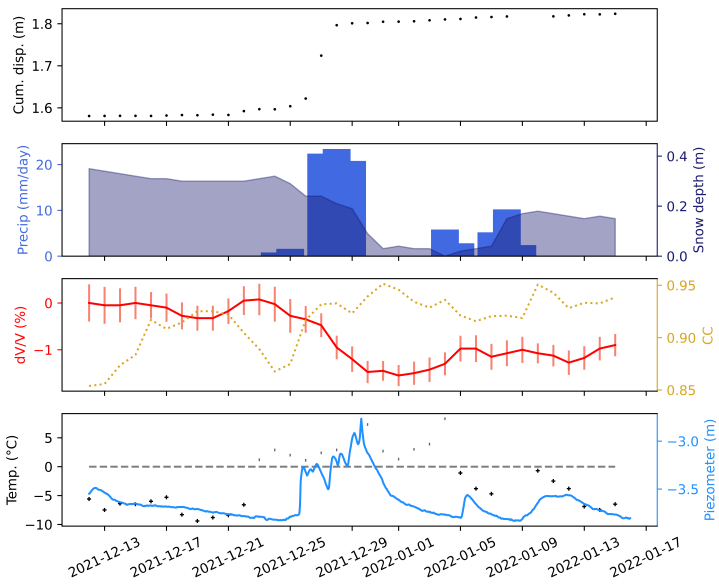

FIGURE 5.8 Same legend as Figure 5.7, zoomed in for December 2021 event (6).

Discussion

The space-time oversampling of RFID results, provides precious insights for understanding the triggering mechanisms of the landslide. We will describe the december 2021 activation event as an example (event 6 in Fig.5.7, and Fig.5.8). The RFID velocity time series focused on the December 2021 activity, suggest a cascading activation (Fig.5.5) : the E group shows notable creeping activity two days before the main event (12/27/2021), with peak velocity in the W sector.

It stands out that the most active W sector is almost never the triggering one, and generally follows a relatively small and progressive displacement of the downslope E sector. The W sector also shows the highest peak velocities, whereas the other shows a more progressive, often creeping behavior. This difference in activation behavior between zones, can be interpreted as a different stage in the landslide deformation process. Indeed, the most active sector is closest to the landslide scarp (and to stable terrain), and is located higher in terms of altitude. There is less material surrounding it, so it seems likely that any viscous damping force will be less pronounced than on the other sector [Nguyen et al., 2017, Hamasaki et al., 2017].

From May to September 2022 (event 8 in Fig.5.7) although no dramatic surface acceleration stands out, a strong change in surface behavior is observed. The main active block W changes directions, a clockwise rotational movement in the lower part of the field is observed, and a new scar appears several meters above the previous one. This is illustrated by the displacement field series from Figure 5.6 and by the photo-series comparing September 2021 to September 2022. We interpret this creeping period as triggered by the rapid top-down displacement occurring at the end of 2021 (event 6 in Fig.5.7). RFID data suggests a change in deformation mechanism during this period (see Figures 5.4 and 5.6), a slow creep followed by rotational movements and the onset of a south-west tendency. Timelapse images and field observations show profound changes in the instrumented zone, with a strong scar retrogression and a downward displacement of the area, as shown by the Geomon vertical series in Figure 5.4. The displacement data as well as the photographs, exhibit a mass transfer towards South-West, and a synchronous downwards retrogression of the field.

Figure 5.7 shows that, although every surface activity is correlated to rainfall, a mere hydrological monitoring is not sufficient to account for landslide activity in the current context. Now taking into account the geophysical quantities, we propose an interpretation of the 2022 activation. Seismic velocity has been linked to material fluidization, especially in clayey environments. Sudden drops in dV/V can be interpreted as a rigidity diminution [Larose et al., 2015], generally triggered by a water intake, leading to fluidization and surface deformation observed by RFID. After the triggering that occurred mid-winter (event 6 in Fig.5.7), the damaged sliding surface would not heal during the next months, with sustained deformation accumulating in the viscoplastic medium [Li et al., 2023, Angeli et al., 1996,Handwerger et al., 2019]. After every strong rain event in early 2022, the dV/V drop is maintained for weeks. This suggests a fluidization of the in-depth slip plane, which is associated to surface creep (see Fig.5.9 and Fig.5.7). This interpretation is also backed up by the general response of the water table to rainfall : in winter because of a lower evapo-transpiration, the water intake is stored longer in the ground, which may induce stronger variations in soil mechanical properties [Finnegan et al., 2021]. With the dry period starting in May 2022 (see piezometer in Fig.5.7), the creeping slows down and the general surface behavior changes. The material property change due to pore pressure variation, vastly documented concerning clay-rich soils, causes a change in soil rigidity due to shrink-swell behavior. This results in the rapid opening of a new landslide scarp about 3 meters above the previous one [Meisina,

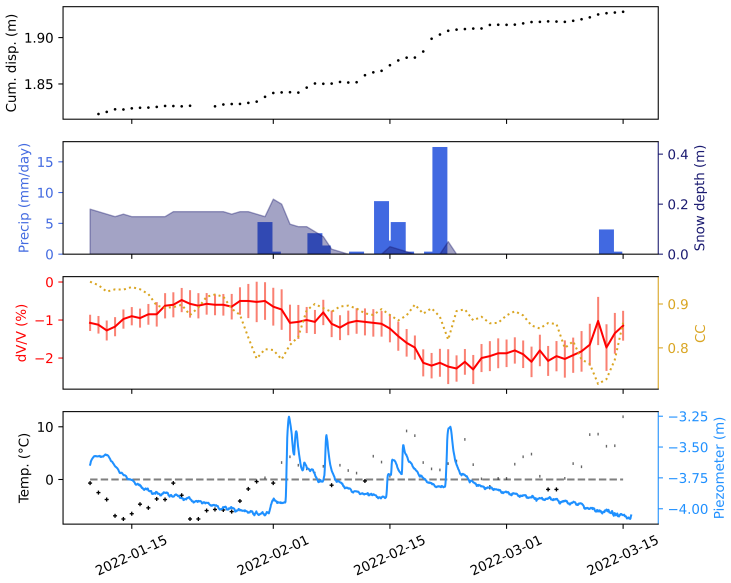

FIGURE 5.9 Same legend as Figure 5.7, zoomed in for February 2022 event (7).

2006]. The evolution of CC regarding surface displacement can be interpreted as a progressive damaging of the material during deformation. This is usually followed by global healing suggested by an increase in CC [Bontemps et al., 2020]. In the case of August-September 2021 (event 5), the correlation decrease precedes surface activity and dV/V change. Concerning the 2022 crack opening, we observe a general decrease of CC over the January-August 2022 period.

Following previous work [Grêt et al., 2006, Hillers et al., 2014], the interaction between hydrology and dV/V can be interpreted as a poro-elastic mechanism, where the shallow water layers are affected by the water table fluctuations. The increased water content elevates the bulk modulus (as well as the density), lowering the S-wave velocity and hence the surface waves velocities [Le Breton et al., 2021]. The general correspondence between dV/V, rainfall and piezometer high-frequency fluctuations in this study, tends to validate this interpretation.

The event of December 2022 (event 6 in Fig.5.7) corresponds to a critical scenario in terms of hydrology, as illustrated in Figure 5.8. Due to a sudden temperature rise and strong precipitations, the 30 cm snow depth accumulated from the previous months melted in 6 days. The corresponding water intake brought the water table to its highest level in the whole observation period. The dV/V drop

was synchronous with the rainfall event, and surface displacements onset. The month-long deformations triggered by precipitation (events 1,6, and 7) are most likely linked to the structural degradation illustrated by the dV/V drop. Nonetheless, it should be pointed that the snow depth measurement was not performed in-situ. As the snow cover evolution can be highly variable at a kilometer-scale, this indicator should be taken with precaution.

The interplay between surface deformation, hydrology and ambient noise measurements, provides a large quantity of information. In this work, the observation set was narrowed in order to produce simpler observables for comparison. Nonetheless, both ambient noise and hydrology results could be further investigated. The seismic velocity profiles (Figure 5.2) could be further analysed to describe more accurately the mechanical properties of the material, as in [Uhlemann et al., 2016] for example.

The RFID clustering method has proven useful to qualitatively estimate the main deformation zones. The identification of kinematic elements showed that some sectors were more coherent (W) than others (E). We believe that clustering can be improved in such scenarios. Notably, implementing spatio-temporal velocity clustering [Ansari et al., 2020] could allow for a more automatized detection of deformation events in both space and time dimensions. This would highlight the triggering, damping and propagation mechanisms that come into play. Moreover, a denser and wider RFID network could increase the robustness of the clustering.

5.5 Conclusion

The two years of data acquired on l'Harmalière provided fruitful insights on the landslide kinematics. Backed-up by a qualitative clustering approach and multi-method monitoring, several landslide activation phases were identified along with their sub-daily kinematics behavior. Two main activation periods were identified, triggered mid-winter and ended in summer (both 2021 and 2022). A retrogression event was analysed, and an interpretation of the multi-observable data was proposed : the damaged slip surface did not heal notably because of the high water level, and the continuous deformation induced a constraint release on the topmost landslide material, leading to crack opening and retrogressive behavior. In general, nearly all notable dV/V changes were directly correlated to

surface activity, either synchronously or with a day-scale time delay. The results suggest cascading triggering mechanisms, between interacting landslides blocks ; namely, it seems that downslope slow creep precedes headscarp activity on the instrumented site. A synchronicity between water table level, precipitation, surface acceleration (RFID) and soil stiffness variation (dV/V) was demonstrated for a majority of activations. Thanks to the 2D-RFID deformation estimation, a retrogressive behavior was identified, correlated to notable dV/V changes and a large advance of the landslide scarp. Velocity clustering results highlighted two main sectors on the instrumented site. A quantitative and automatized clustering of RFID velocity series can be foreseen in the future. Future work will further investigate hydrological data as well as ambient noise depth inversion, and the interplay between both.

5.6 Appendix

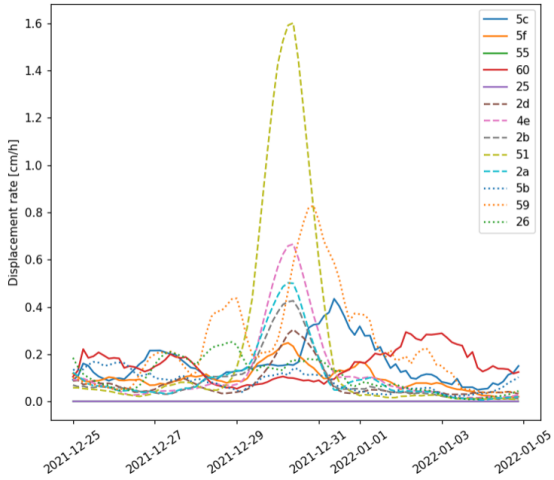

FIGURE 5.10 Velocity series for RFID tags during the december 2021 main activation (event 6 in Fig. 5.7).

Pictures from inside the landslide. Displacement in the Harmalière landslide are frequently impeded by the dense vetegation, or the clay which is dry and friable in summer, then resembling slippery quicksand in winter.

Chapter 6

Towards centimeter precision UAV-RFID localization

6.1 Abstract

Radio-Frequency Identification (RFID) shows great potential for earth-sciences applications [Le Breton et al., 2019], notably for landslide surface monitoring at a high spatio-temporal resolution with long-term robustness to meteorological events (rain, fog, snow) [Le Breton et al., 2019, Charléty et al., 2022b]. The ability to localize RFID tags using Unmanned Aerial Vehicles (UAV) in a Synthetic Aperture Radar (SAR) approach, would offer new possibilites for monitoring inaccessible terrain, even under vegetation and snow. To that end, an onboard measurement system was built that allows Global Positionning (GPS) tracking of an RFID reader antenna, in order to perform real-time SAR measurement acquisition. Three antenna tracking methods were compared. In addition, Marko-Chain Monte-Carlo (MCMC) optimization was used to estimate tag position and characterize the solution, even in non-convex cost function scenarios. Two cost functions were compared, based on different RFID-phase processing approaches. Real-time SAR-RFID localization yielded a centimeter accuracy in the horizontal plane, with lower resolution in the vertical direction. The Post-Processed Kinematics algorithm proved to best fit antenna tracking. The unwrapped-phase based cost function provided more convex solutions, at the cost of a lower accuracy compared to the complex-phase cost function.

MCMC is computationally efficient in SAR-RFID optimization, with enhanced results concerning the shape and orientation of the main localization errors.

6.2 Introduction

In the recent years, the use of Unmanned Aerial Vehicle (UAV) as a means of remote sensing has been a growing research topic [Mohd Noor et al., 2018, Hugenholtz et al., 2012]. In Earth Sciences and Environmental Remote Sensing, UAVs provide a relatively cheap solution to investigate unreachable or dangerous places for humans. Compared to satellite-based remote sensing, UAV's allow for a more local and flexible investigation, especially in terms of acquisition frequency. Compared to heavier local devices (fixed Lidar, total station, etc), they represent a lighter solution free to investigate both wide areas and specific objects. With the Internet-of-Things (IoT) paradigm, new sensing systems are appearing in which the role of UAVs is of importance, notably in telecommunication [Feng et al., 2018] and agriculture [Boursianis et al., 2022]. Radio-Frequency Identification (RFID), which is an important domain in IoT [Jia et al., 2012], has acquired rising interest in the Earth Science community [Le Breton et al., 2019] for a variety of applications such as pebble tracking, soil moisture sensing, snow depth estimation [Le Breton et al., 2023b], or landslide displacement monitoring. The combination of UAV and RFID technologies provides great possibilities notably in the domains of logistics and retail [Motroni and Nepa,], but also in environmental sensing [Cassel et al., 2020, Piégay et al., 2020] and notably ground surface displacement sparse monitoring [Ilinca et al., 2022].

Landslides are complex natural hazards, under investigation since decades. Monitoring is essential both to study landslide dynamics and to create early warning system. Surface displacement is commonly monitored and predicted using a wide variety of technical devices, in order to warn the affected communities when necessary [Chae et al., 2017]. Aerial remote sensing solutions include Interferometric Synthetic Aperture Radar (InSAR) and airborne imagery. Stable in-situ methods rely on total stations, Lidar devices, GNSS or extensometer, and recently RFID landslide monitoring was demonstrated [Le Breton et al., 2017] and improved [Charléty et al., 2022a, Charléty et al., 2023a] with a system of fixed antennas in both 1D and 2D localization schemes [Le Breton et al., 2019, Charléty et al., 2022b].

Most methods suffer from specific outdoor conditions, such as steep slopes, rain and fog, snow,

vegetation or wandering animals. The above-cited approaches can hardly measure accurate displacements under vegetated cover, even less in the case of snow as its surface movement (snow creep) does not match ground motion. In this context, RFID shows interesting features that allow measurements without a free line-of-sight between readers and tags, with a manageable sensitivity to vegetation and snow [Le Breton et al., 2023a]. Although the interactions between RFID systems and snow or vegetation have been partly studied [Le Breton et al., 2017, Le Breton et al., 2023b], tag localization in these media has not yet been demonstrated.

As of now, RFID measurement systems installed on landslides have always been fixed stations [Le Breton et al., 2019, Charléty et al., 2022b]. We foresee the development of UAV-RFID localization as a promising method, that could greatly enhance the size of RFID-monitored sites, ensuring a vegetation- and snow-ready measurement technique [Le Breton et al., 2022].

This paper proposes to investigate the intricate challenges of UAV-RFID landslide monitoring, and monitoring under vegetation or snow cover : can we monitor surface displacement through snow and vegetation using UAV-RFID, and with which performance ? First we introduce the subject in an operational manner (Sec. 6.3), reviewing the various sources of error and the corresponding literature. The performed experiments are then described in the Materials and Methods (Sec. 6.4). Next, specific aspects concerning RFID data inversion are covered (Sec. 6.5). Lastly the localization results are presented and discussed (Sec. 6.6).

6.3 Operational review for outdoor localization

UAV-aided RFID localization using phase-of-arrival measurement, is a challenge that puts several devices and measurements into play. In that sense, it is a complex problem that implies many sources of error and offers a variety of choices at every step of the process. Table 6.1 proposes a summary of all the measurement chain, to the best of our knowledge, and the corresponding literature works. This table was constructed in an operational perspective, in order to help decipher and reduce individual error sources.

First the localization of the drone and the antenna attached to it, can be performed in multiple ways. Using a single GNSS receiver, Precise Point Positionning (PPP) can provide centimeter accuracy after post-processing [Alkan et al., 2020]. This method often requires dual-frequency measurement and

is best suited for immobile antenna positioning [Monico et al., 2019]. Differential methods using base and rover GNSS receivers, such a Real Time Kinematic (RTK) or Post Processed Kinematics (PPK), only require mono-frequency measurements to reach centimeter accuracy. The latter proved to be more accurate than RTK because of the better integration of correction and calibration data [Remzi et al., 2020]. Nonetheless the loss of a fixed-integer position can occur, leading to the absence of usable data points. To prevent this, Suzuki *et al.* [Suzuki et al., 2016] used the redundancy of multiple GNSS receivers mounted on the same drone. Another solution would be to track the antenna using a total station [Janos et al., 2022]. Although this would yield the best accuracy (even used as a reference compared to GNSS), it would also negate many advantages of the approach : heavy ground-based devices, and need for line-of-sight.

When performing measurements with a flying antenna, the geometrical relation between the GNSS rover position and the antenna position (so-called "lever-arm effect") can vary because of tilt [Daakir et al., 2016]. This is even accentuated in outdoor scenarios, and when the drone flies at high speed or follows an erratic trajectory because of the wind. The use of an embedded inertial measurement unit (IMU) for correction can therefore be necessary. In the present scenario, all experiments where performed at low velocity (a few cm/s at most) on a stable support, so that no inertial correction was required.

Variations in the phase center position are also prone to appear, notably with varying reader angle as studied in [Li et al., 2021] or due to a metallic surrounding. In extreme angle geometries, this can lead to a 1.2rad phase offset (3 cm with the present UHF devices). The presence of the metallic drone structure is generally accounted for by setting the phase center 10 cm above its physical center [Buffi et al., 2018]. The combination with antenna tracking error (drone position + tilt) then produces non-negligible uncertainties, which motivates the exploration of phase-differential methods that can reduce the impact of phase center bias, by focusing on the local phase variation.

In every RFID-SAR scenario, the shape of the trajectory has a notable impact on the localization performance. A general rule states that the longer the trajectory in one direction, the better the localization accuracy. The shape of the trajectory can generate secondary peaks in the inversion process, as studied elsewhere using simulation [Bernardini et al., 2020a]. In scenarios where the antenna overlooks tags placed on the ground, the trajectory should have maximal vertical and horizontal extension. Measurements from multiple antennas are also used to increase the size of the SAR without actually in-

creasing the antenna trajectory [Bernardini et al., 2020b].The spatial sampling frequency should follow Shanon's criterion, which imposes a limit on the drone flying speed in the case of real-time measurements. During the measurement process, usual phase measurement errors are expected, with a notable relationship to RSSI values [Le Breton et al., 2017]. Moreover, in the case of rough terrain or presence of water (humid vegetation, snow, soil moisture), multipath interference may generate measurement biases that can hardly be simulated nor canceled.

Another critical aspect of this multi-measurement setup is the time synchronization of RFID, GNSS an potentially IMU data. At a flying speed of 1 m/s a time delay of 10 ms can lead to a 1 cm space offset between UAV position and corresponding RFID measurement, added to the relatively poor stability of the RFID reader in time. To overcome this issue, trigger events have been used for initial synchronization [Buffi et al., 2018]. Added to this difficulty, is the fact that GPS measurements are under-sampled compared to RFID.

Once the measurement is performed, the inversion problem poses yet another set of issues. RFID phase data is usually taken in its complex form and the cost function is defined by the correlation score between measured and synthetic vector [Buffi et al., 2018]. Other methods rely on segmented phase unwrapping, which tends to reduce the localization ambiguity [Tzitzis et al., 2021, Li et al., 2021]. Lastly, the optimization algorithm is a crucial choice in terms of computational cost. A grid-search approach can be used for exhaustive characterization [Bernardini et al., 2020a], but in real use cases other methods were explored : Particle Swarm Optimization (PSO) was lately used for complex-phase, non-convex cost functions [Bernardini et al., 2020b], and simpler gradient methods were applied to unwrapped-phase convex cases [Tzitzis et al., 2021]. In general it is more efficient to exploit all available observables such as RSSI and phase, in order to reduce the search window and then perform a more costly inversion [Li et al., 2021].

6.4 Materials, methods and workflow

Experimental test structure, embedded system

An experimental setup was built to simulate the embedded system on a flying drone, with all devices mounted on a fiber glass structure (see Figure 6.2). This structure, inspired by [García-Fernández et al., 2020], allowed for a 1D-SAR trajectory of length 1.6 m without actually flying a UAV.

Error source	Comment / solution	Error estimate	Literature
Reader Positioning			
Localization approach	PPK/RTK/PPP.	1-5 cm	[Bisnath et al., 2004, Remzi et al., 2020, Suzuki et al., 2016], this paper
Loss of fixed-integer solution	Related to sky view / multipath environment. IMU can help.	Data loss	[Suzuki et al., 2016, Jackson et al., 2018]
Sky view	DOP, satellite clock errors. Implies a time-varying bias.	1-10 cm	[Maciuk, 2018, Cledat et al., 2020]
Reader Antenna Position ing			
Lever-arm effect	Requires IMU.	1-10 cm	[Daakir et al., 2016, Gautam et al., 2019, Zhong et al., 2016, Angelino et al., 2012, You et al., 2020]
Time sync between GPS and RFID measurement	Trigger event, or NTP sync.		[Buffi et al., 2018, Eling et al., 2015, Hasan et al., 2018], this paper
GPS/RFID subsampling	Interpolation using IMU or other methods.		[Ch'ng et al., 2019]
Phase meas.			
Antenna phase center variation	Angle (antenna directivity) and environment dependent.	1-10 cm	[Li et al., 2021, Buffi et al., 2018]
Random phase error	Depends on antenna and signal strength.	1 cm	[Le Breton et al., 2017, Charléty et al., 2022b]
Propagation phase error	Multi-path interference, media-dependent delay.	1-20 cm	[Charléty et al., 2022b, Lu et al., 2016, Wang et al., 2020a, Casati et al., 2017], this paper
Doppler phase shift	Depends on UAV velocity.		[Tesch et al., 2015, Azarfar et al., 2021]
Inversion problem			
Shape of trajectory	Secondary peaks could appear. SAR length should be maximized in all directions.		[Bernardini et al., 2020a, Bernardini et al., 2020b]
Density of points	Shanon criterion should be respected, even with trajectories distant in time.	1-10 cm	[Bernardini et al., 2020a, Shannon, 1949]
Choice of cost function	Wrapped/unwrapped phase, differential, RSSI.		[Buffi et al., 2018, Bernardini et al., 2020b, Ma et al., 2020, Tzitzis et al., 2019, Tzitzis et al., 2021], this paper
Inversion algorithm	Computation time, accuracy, precision estimation.		[Bernardini et al., 2020a, Bernardini et al., 2020b, Tzitzis et al., 2019], this paper

TABLE 6.1 Errors sources for UAV-RFID localization.

A receiver provided rover GNSS signal connected to a local base with short baseline (<10 m). RFID measurements were performed with a reader connected to a circular polarized RFID antenna, using a carrier frequency of 867 MHz and at a sampling frequency of 20 Hz. Internet and wireless connection was provided by a 4G+ modem. Time synchronization was performed by using a supplementary GNSS dongle [Hasan et al., 2018] through a local NTP server to which the RFID reader was synchronized. This way a millisecond-order delay was insured between all measurements. All the devices were connected to a Raspberry Pi (Rpi), that launched and stored the various measurements. This measurement system was then moved on a rail structure made of fiber glass, guiding the system on a 1D trajectory. The height and orientation of the structure varied in the different experiments. Lastly, a mini-prism was mounted on the system to perform tacheometry reference measurements [Bláha et al., 2012]. Figure 6.1 presents a general scheme summarizing the measurement setup, as well as the construction of the SAR data.

Data pipeline to produce the SAR

The Synthetic Aperture Radar is a composite vector, combining both reader position and corresponding phase measurement. This section describes the construction of this SAR vector from raw measurements.

First we will discuss the SAR trajectory tracking. In this study PPK and RTK were used for reader tracking, along with tacheometry for reference measurement. For PPK, the raw observation files measured from the base and rover were post-processed using RTKLib [Takasu and Yasuda, 2009] to obtain a 5Hz-sampled position series. For RTK, the pyUBX [pyu,] python module was used. In any case, when the fixed-integer solution was lost (leading to a floating point solution), the data was discarded.

The SAR vector consists of both 3D position and 1D phase measurements, in a $4 \times N_r$ shape, where N_r is the total number of readings. Due to different sampling frequencies an interpolation of the antenna position is required. A spline interpolation was applied for continuous measurements that respect the Shannon criteria, although IMU-based interpolation could yield better results. When the criteria was not met, no interpolation was performed. In real-time acquisition scenarios, i.e. when the antenna position changes between every RFID measurement, high acceleration periods were discarded because the tilt, vibrations or elastic deformation could disrupt the geometrical relationships between the different system devices.

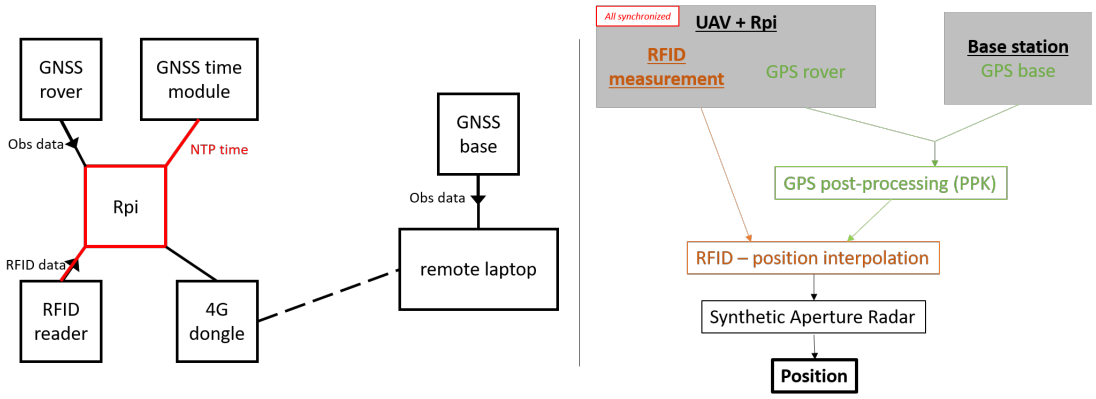

FIGURE 6.1 (Left) Schematic of the SAR embedded measurement system. (Right) Workflow for data processing, from raw measurement to SAR inversion.

Step-by-step 1D-SAR experiments

The following experiments were performed using the fiber glass structure fixed on the ground (see Figure 6.2). During experiments the system was moved manually step by step, with a 10 s step measurement duration. This allowed for a stable configuration at each point. The spatial increment between measurements was 3 cm. Pointwise tacheometer references were taken using a total station and the mini-prism. The 1D-localization experiments were performed using the fiber glass structure, in a variety of propagation media.

- Vegetation : Two different vegetation types were tested : blocks of hay (30 cm thick) and layers of bark (20 cm thick), with different moisture contents. The materials were super-imposed in various geometries over the tags before the SAR measurement, as represented in Figure 6.2. The moisture content was estimated by drying the material and weighing it.
- Snow : In freezing conditions, a tag was placed below a 28 cm thick homogeneous dry snow layer, with an average density of 0.54. The homogeneity of the snow was verified with snow density measurements at various depths, and the snow temperature profile was measured as well. This confirmed dry snow conditions (negative temperature on the whole profile). The structure was placed to perform 1D measurements both with and without the snow layer.

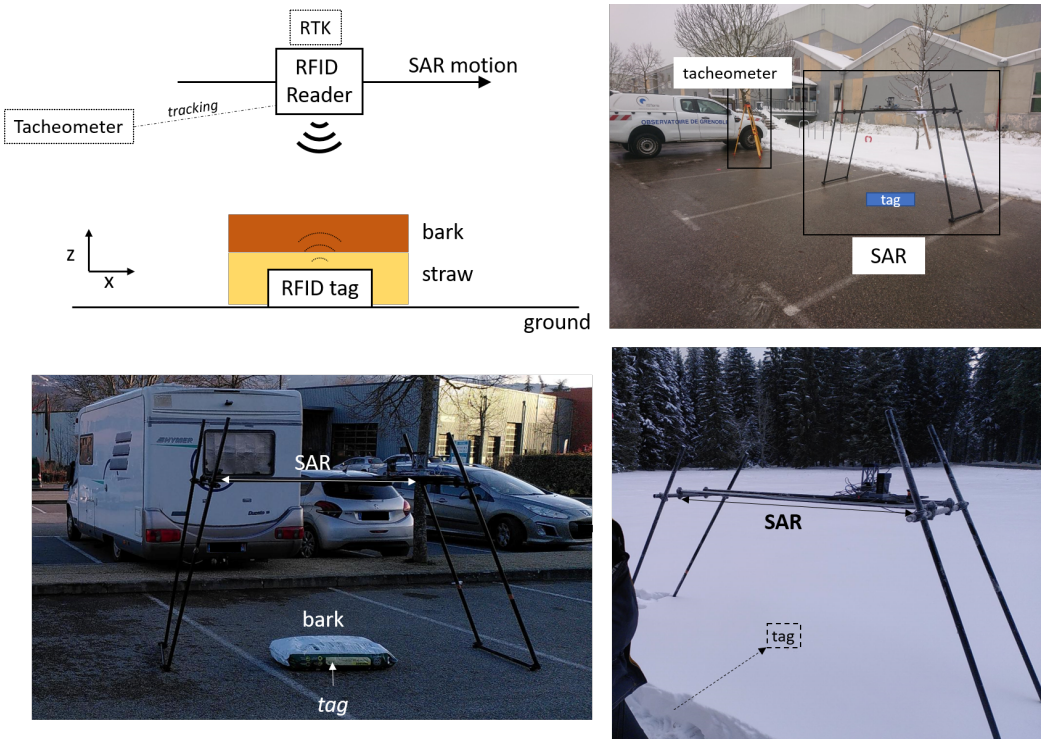

FIGURE 6.2 Summary of the 1D experiments. (Top left) Schematic of the typical 1D measurements. (Top Right) Experiment in air. (Bottom Left) Vegetation experiment. (Bottom Right) Snow experiment.

Real-time 3D-SAR experiments

A set of experiments was performed with continuous movement and real-time sampling. The fiber-glass structure was handheld to perform 3D trajectories, during synchronized measurement from GNSS and RFID. The antenna velocity was low (a few cm/s) and kept a steady orientation, as was confirmed by inertial measurements. The real-time measurement campaigns were performed in clear sky conditions.

6.5 From SAR to tag position : inversion methods

In this section, the methods used to estimate the tag position from the SAR tracking and phase measurements are discussed. First, two cost functions are compared ; then a heuristic is proposed to reduce the inversion search space ; finally, we discuss the importance of the vertical antenna tracking error on the final localization result.

Choice of cost function

In this section, two different cost functions are presented for SAR inversion in order to compare them : complex phasor correlation and guided unwrapping.

C_1 : Complex phasor correlation Most phase-based SAR-RFID localization works [Buffi et al., 2018] use the following scheme in order to localize an RFID tag with a moving antenna. Let s_i be the complex phase value measured at time i. In this work we do not consider the signal amplitude, as the localization only exploits phase values. Each phase measurement ϕ can be expessed as :

$$\phi_i(p_{ant}, p_{tag}) = -4\pi r_i/\lambda + \phi_0 + \phi_{bias} \tag{6.1}$$

Where λ is the carrier wavelength, r_i is the distance between antenna and tag phase center positions p_{ant} and p_{tag}, ϕ_0 is an unknown phase offset due to phase propagation in the reader, cable and reading antenna, and ϕ_{bias} is a bias due to multipath or antenna phase center variation. Note that ϕ_0 is supposed constant, and ϕ_{bias} is not modeled in this work. As it is only a second order quantity, we will discard ϕ_{bias} in the following. We will nonetheless discuss it later. The complex phasor s_i is defined as follows :

$$s_i = e^{-j\phi_i} = e^{-j(-4\pi r_i/\lambda} + \phi_0) \tag{6.2}$$

In the following we only consider the phase variation and not the absolute phase value, in order to remove the constant ϕ_0. Usually this is done by subtracting the first measurement :

$$\Delta s_i = \frac{s_i}{s_0} \tag{6.3}$$

and reducing the measurement vector $\mathbf{y}$ to a normalized phasor sequence :

$$\mathbf{y}(p_{ant}, p_{tag}) = [1,\ \Delta s_1\ ...\ \Delta s_n]$$

Inversion is performed by producing a synthetic measurement vector $\mathbf{a}$ based on a hypothetical tag position p'_{tag} and the estimated antenna trajectory :

$$\mathbf{a}(p_{ant}, p'_{tag}) = [1,\ \Delta s'_1\ ...\ \Delta s'_n]$$

The best match between the measured and synthetic vectors is then found through the normalized correlation product :

$$C_1(p'_{tag}) = \frac{|\mathbf{a}^H \mathbf{y}|}{\|\mathbf{a}\|\ \|\mathbf{y}\|}$$

With H the Hermitian operator.

C_2 : Guided phase unwrapping Phase unwrapping is a crucial aspect of phase-based RFID localization, usually associated to cost-function convexity and more constrained localization solutions. The complex trajectory of outdoor UAV flights and on-board data acquisition, add to the difficulty of ad-hoc phase unwrapping. Additionally, rough terrain and humidity generate unpredictable multipath interference, and loss of data points can lead to phase decoherence.

We propose a simple algorithm derived from fixed-antenna RFID monitoring [Charléty et al., 2023a] in order to perform unwrapping based on a model. To keep track of phase coherence, we utilize the synthetic unwrapped-phase vector for every test point $\mathbf{b}$ built through Eq.6.1 as a reference for unwrapping the measured wrapped phases $\mathbf{y}$:

$$\mathbf{y}_g = U(\mathbf{y} - \mathbf{b}) + \mathbf{b} \tag{6.4}$$

With U an unwrapping operator as discussed in [Li et al., 2021, Sarkka et al., 2011a], the choice of which is not the subject of this work. In the present case we used the complex smoothing unwrapping approach, presented in [Charléty et al., 2023a]. Note that the knowledge of ϕ_0 remains unnecessary as we can still normalize both vectors to the first measurement. The guided output $\mathbf{y}_g$ is thus unwrapped to correspond to the test point phase series $\mathbf{b}$, especially after long data gaps. The proposed cost function is the same as C_1, in order to obtain comparable cost functions.

$$C_2(p'_{tag}) = \frac{|\mathbf{b}^H \mathbf{y}_g|}{\|\mathbf{b}\|\ \|\mathbf{y}_g\|}$$

We have herein presented two cost functions for SAR inversion. The two next sections will discuss the inversion approach, first reducing the search space, then using MCMC to characterize the cost function.

Pre-localization heuristic

In order to reduce computational cost, it is necessary to have a relatively small search zone. Additionally it is important to use a robust convergence algorithm, to prevent incorrect localization results due to secondary peaks. Final inversion is generally performed using only phase measurements, but pre-localization can be performed using more classical RSSI-based algorithms [Ni et al., 2003, Han and Cho, 2010]. Even though the latter show accuracy on the order of $0.5 - 1$m, it reduces the search window and the computational cost in a cubic manner. In this work we use the RSSI maximum as the center horizontal of the search space, which is a cube of variable size depending on the experiment.

Inversion algorithm

In this section, the choice of the optimization method is discussed, which is an important matter as well. Firstly because the cost function is generally non-convex, and gradient-based algorithms do not converge towards a stable solution. Secondly because an exhaustive search (so-called gridsearch) implies a high computational cost, especially in the case of a 3D search in a meter-wide window. For both research purposes and real-world applications, using an efficient algorithm to find the tag location is thus crucial.

In a real-world outdoors scenario, with uncertain antenna height due to rough terrain, and unstable trajectories due to wind and obstacles, typical inversion methods do not provide stable minima. As was studied elsewhere [Bernardini et al., 2020a], the shape of the cost function greatly depends on the SAR trajectory, with secondary peaks often appearing.

This paper proposes to use a Markov-Chain Monte Carlo (MCMC) optimization, which is suited for global optimum research of non-convex cost-functions [Gilks et al., 1995]. Moreover MCMC constructs a covariance matrix in the parameter space, providing useful information about the main directions of error. This paper will not go into detail concerning this method, only stating that MCMC builds a Markov Chain that approximates the probability distribution of a given function, here C_1 or C_2. One classical way of building this Markov Chain is the Metropolis-Hastings algorithm, which we use

here. The ergodic property of this random walk algorithm, tends to approximate the cost function as a probability density distribution. The general MCMC approach is inspired by [Serripierri et al., 2022, Moreau et al., 2014]. First a simulated annealing (SA) algorithm is run to obtain a starting position [Du et al., 2016] and an estimate of the measurement variance, then classical MCMC [Chib and Greenberg, 1995] is run for cost-function mapping. Using the correct parameters, the output distribution represents the cost-function.

Sensibility to antenna position uncertainty

In the SAR-RFID scenario, there is a doubled negative effect from the system sensitivity in the vertical direction. It is widely documented that GPS solutions show a higher uncertainty in the vertical direction than in the horizontal one [Zandbergen and Barbeau, 2011]. Moreover, the direct model for phase measurement is especially sensitive to a vertical displacement of the reader antenna, because the UAV flies above the RFID tag [Bandini et al., 2022].

Let us derive a simple model to explain the vertical sensitivity of the system. Figure 6.2 describes the system. As derived elsewhere [Charléty et al., 2022b], the phase variation $d\phi_m$ in the direct model at first order is expressed as :

$$d\phi_m = \frac{1}{\sqrt{x^2 + z^2}} \begin{bmatrix} x \\ z \end{bmatrix} \begin{bmatrix} dx_r + \epsilon_x & dz_r + \epsilon_z \end{bmatrix} \tag{6.5}$$

Where x and z are the antenna-tag distance coordinates, dx_r and dz_r are the true position variations, ϵ_x and ϵ_z are the antenna localisation errors. The GPS device that we use yields values of $\epsilon_x \approx 1$ cm and $\epsilon_z \approx 3$ cm, confirmed by the literature [Janos and Kuras, 2021]. In usual UAV trajectories, the z coordinate is usually less prone to vary (if not set to a constant) than the horizontal coordinates. In the present step-by-step scenario, the true variation dz_r between consecutive measurements is of mm order. This implies that the modeled height variation $dz_r + \epsilon_z$ is mostly driven by the vertical error ϵ_z. In addition, the fact that $z > x$ in the general case of a drone flying over the tag, yields a higher sensitivity in the z direction. For these reasons it is important to mitigate the antenna vertical position error.

We have covered various aspects of SAR inversion, notably the choice of the cost function and the importance of the vertical tracking error. Next section will present and discuss the results.

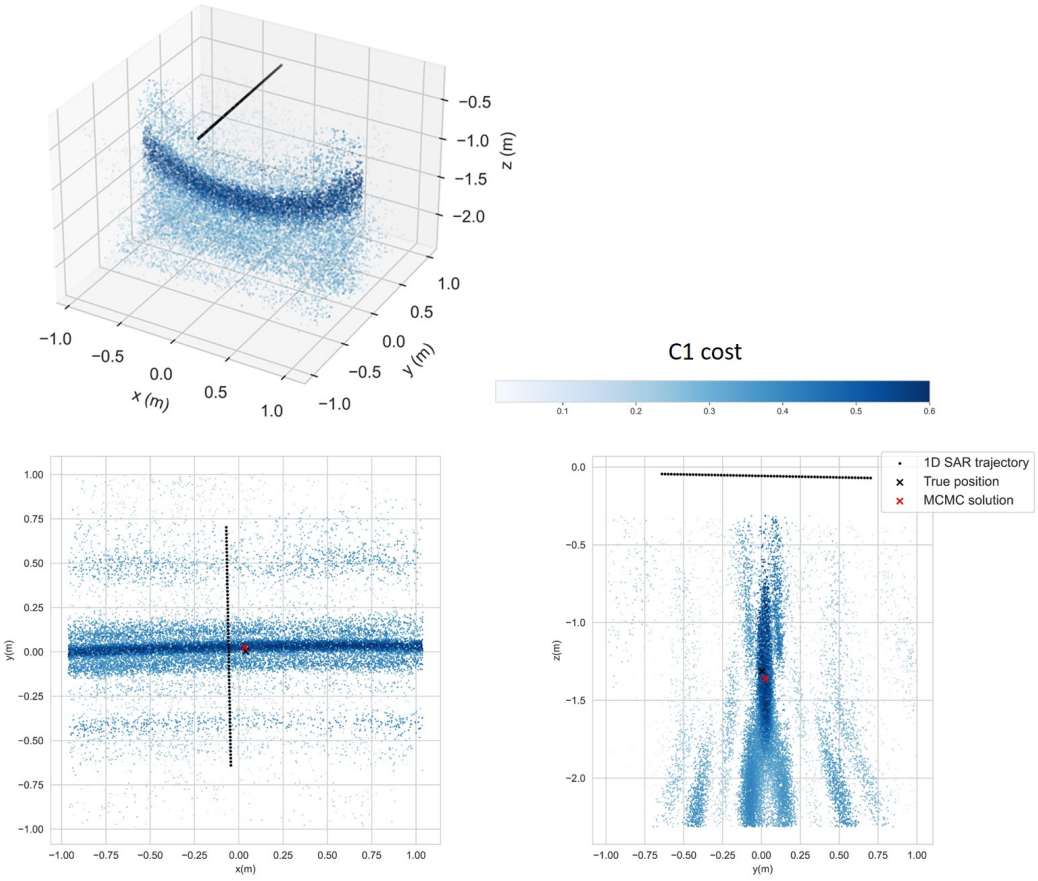

FIGURE 6.3 Qualitative results for the localization of a tag using a 1D SAR and tacheometry for antenna tracking. (Top) 3D view of the MCMC distribution (180 000 points out of 800 000 candidates). (Bottom) xOy and yOz projections of the MCMC distribution. The colors represent the corresponding cost using C1. The true and estimated position are shown as crosses.

6.6 Results and discussion

Before analysing the localization results, we first validate the MCMC method in comparison to a grid-search algorithm. Then the various antenna tracking methods, and 1D localization under different media are compared. The two cost functions C_1 and C_2 are discussed, and finally 3D real-time localization is presented. In this next section, all MCMC results are presented in a statistical manner. After performing the MCMC run with a given number of candidates (typically 100 000), the distribution is plotted as a histogram with sub-centimeter resolution, or as a 3D scatter-plot.

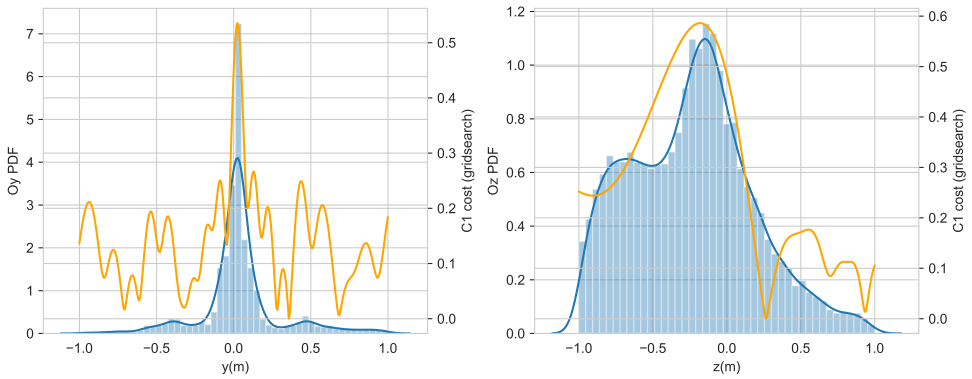

FIGURE 6.4 In blue, histogram of the MCMC distribution projected on the Oy (right) and Oz (left) axes. In orange, gridsearch estimation of the cost function along a line, centered on the estimated position.

Validation of MCMC localization with 1D SAR

Figure 6.3 presents qualitative MCMC results for a 1D-SAR experiment performed in air. The multivariate plots highlight the 3D shape of the cost function, which resembles a torus centered around the SAR axis. When projected onto Oy and Oz, the MCMC distribution indicates the presence of minor secondary peaks, although not generating localization ambiguities. An exhaustive gridsearch was computed along the main SAR directions, centered around the MCMC solution. The comparison between gridsearch and MCMC in Figure 6.4, shows coherent maxima. The difference in cost function shape is due to the different search spaces represented by both 3D-MCMC and 1D-gridsearch : the first represents accumulated results along the whole 3D search space, whereas the second only shows the cost function along a 1D-line. Figure 6.4 shows that MCMC succeeds in accurately mapping a non-convex function for SAR-RFID phase inversion, with a lower computation time and better (virtually unlimited) resolution than a gridsearch algorithm. Moreover the MCMC output is directly exploitable for a statistical evaluation of the inversion (see below).

Tag localization using different antenna tracking methods

Table 6.2 shows results for 1D-localization using different antenna tracking methods. The tacheometer is the most accurate method, as could be expected from the devices' reported performance [Bláha et al., 2012]. RTK and PPK yield a similar accuracy in the horizontal plane. The artificial vertical stabilization of the SAR trajectory tends to improve the vertical localization results.

Localization scheme	**Tacheo**	**RTK**		**PPK**
	1D	1D	Stable Z	3D
ϵ_y (m)	< 0.01	0.015	0.01	0.02
ϵ_z (m)	0.026	0.08	0.04	0.03

TABLE 6.2 Summary of localization results using a fiber glass stable structure, and the autonomous measurement system. The 1D experiments were performed step-by-step, while the 3D experiment was real-time.

Vertical stabilization for RTK The higher vertical error for both PPK and RTK is partly induced by the poor accuracy of both methods in this direction. The reported RMS of the U-blox F9P is 3 cm in the vertical direction [Robustelli et al., 2023], which was also verified *in situ* during the testing phase. This Oz instability produces poor inversion results as stated previously. An artificial stabilization of the vertical coordinate was tested : a 3-point rolling average was applied on the RTK vertical coordinate, increasing the Oz localization accuracy by a factor 2 (see Table 6.2). This smoothing showed satisfactory results in a controlled and stabilized experiment. We believe more research should be performed in order to generalize it to real-time acquisitions. Indeed as the behavior of the SAR phase does provide information about the Oz antenna movements. A Kalman filtering approach could for example be applied in a SLAM approach, that would take into account the vertical error of the antenna as well a data fusion from IMU or Lidar devices [Gupta and Fernando, 2022].

Tag localization under vegetation and snow

The drying experiment revealed a 50% moisture content for bark, against 2% for hay. Figure 6.5 shows localization results for the vegetation experiments, illustrated by MCMC histograms. Hay does not show any significant effect on the radiowave time of flight, thus on the localization cost function, even when two blocks of hay are used (1m depth of material over RFID tag). As shown in Table 6.3, the localization error stays within centimeter margins. On the contrary, the effect of bark is more notable. The shape of the solution is not changed dramatically but the error isl higher in both Oz and Oy directions. In the case of a bark/hay superposition, with the moist bark above hay, the localization results are strongly disturbed. The cost function is modified especially in the Oz direction, where a clear secondary peak appears. In both directions, the peak is widened and shows a higher deviation. This disturbance is most likely due to multipath effects, as was confirmed by comparison of phase

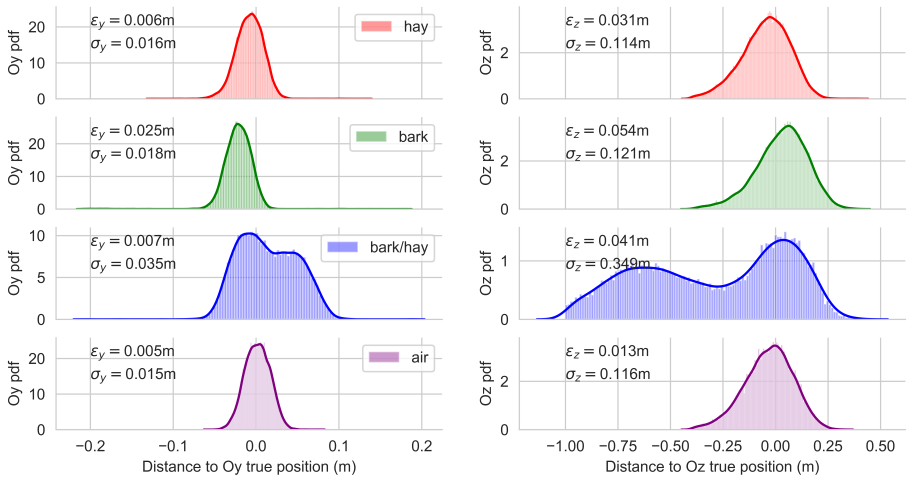

FIGURE 6.5 MCMC results for the 1D vegetation experiments, with ϵ_y and ϵ_z the localization error along Oy and Oz, σ_y and σ_z the respective standard deviation of the MCMC distribution. All results were computed using C_1.

Medium	Air	Hay	Bark	Bark/Hay	Snow C_1	Snow C_2
ϵ_y (m)	< 0.01	< 0.01	0.03	0.01	0.05	0.06
ϵ_z (m)	0.01	0.03	0.05	0.04	0.14	0.25

TABLE 6.3 Localization results for various propagation media : error ϵ_y along the 1D-SAR direction, and ϵ_z along the radial direction (or vertical).

measurements.

The localization results under snow are presented in Table 6.3 and Figure 6.6, with typical errors about 3 cm. Using the same cost function as in the vegetation experiment (C_1), we note that the snow induces a strong secondary peak approximately one wavelength away from the main one ($\lambda \approx$ 16 cm). Focusing on the main peak, a 5 cm horizontal error is still obtained, and 12 cm error in the vertical direction. The localization in air from Figure 6.6 shows a higher error than in the vegetation experiments, although it remains in the standard deviation limits. The cost functions will be compared below.

Interpretation The sensitivity to the bark material can be explained by its higher moisture content, as well as its mesoscale material structure, that present a high number of air/wood interfaces (RF diffraction and diffusion). As could be expected from the mostly horizontal trajectory, the verti-

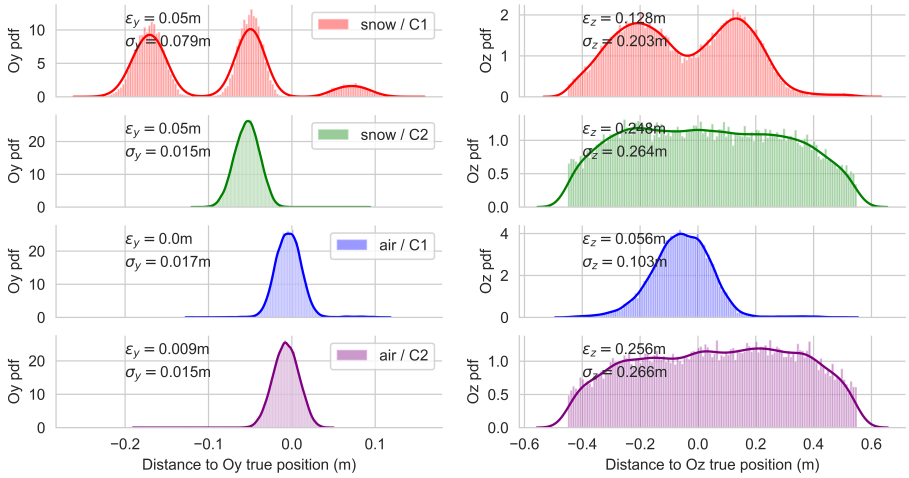

FIGURE 6.6 MCMC results for the 1D snow experiments, with a comparison between C_1 and C_2 results.

cal direction is more sensitive to perturbations of the medium. Moreover, one specificity of the bark material was its asymmetry : one side of the bark layer was thicker, which deported the measurement bias towards a specific direction. Translated in real scenario, this highlights that non-homogeneous and moist material can strongly disturb both measurement accuracy and precision [Le Breton et al., 2017, Pichorim et al., 2018], especially if they are elevated above ground (wet leaves for example). This is why the snow experiment was performed with dry and fresh snow : although it caused a considerable phase shift, the relative homogeneity and symmetry of the medium preserved the coherence of the measurement. Nonetheless, the overall 1D results show that the effect of snow on localization are the highest compared to the tested vegetation. Besides, the snow might artificially lower the position of the tag, because of the longer optical path in snow than in air. Due to the vertical ambiguity of the results it is not possible to conclude on this aspect.

Comparison of cost functions

Figure 6.6 also presents MCMC results using cost functions C_1 and C_2, for the snow experiment. C_1 produces an ambiguous inversion result with multiple peaks in the presence of the snow layer. This is most likely due to the multipath interference and phase delay introduced by the snow. On the contrary,

C_2 generates a stable peak in the Oy direction. This can be explained qualitatively, by stating that the guided-unwrap approach accumulates information along the whole SAR. Indeed, a correct phase unwrap is new information for inversion and it reduces the ambiguity. We interpret C_2 as a way of averaging the ambiguities that C_1 highlights. Conversely C_2 produces a much broader vertical peak, lowering the accuracy of the Oz localization. In this direction, C_1 thus seems like a more accurate solution.

The smoothing nature of the C_2 function translates in a less pronounced minimum and a decreased MCMC process temperature, which implies a higher number of candidate rejection. In order to obtain a given number of points in the distribution, C_2 hence needs more MCMC iterations. Moreover as C_2 implies more operations (unwrapping is a significant burden), its computation time is higher than C_1. This is balanced by the convexity which makes gradient-descent possible using C_2.

Limitations of the unwrapping approach C_2 : Note that the C_2 algorithm is based on the assumption that ϕ_m and ϕ_t behave in a similar way, and is built to estimate the resemblance of the two series in a real-data scenario. If the two series have nothing in common, the algorithm will produce non-realistic over-fitting results that should be discarded. This method proves to be more stable than standard phase unwrapping, and the added information allows for a better convergence when searching for most probable tag position.

Although phase unwrapping shows considerable advantages, it is much more sensitive to perturbations. Notably when the space sampling frequency changes (UAV speed variation) and in strong weather scenarios (wind/rain/vegetation), the stability of any unwrapping algorithm is challenged [Charléty et al., 2022a]. Most unwrapping algorithms have been developed and tested indoors [Tripicchio et al., 2021, Tzitzis et al., 2019], where the faced challenges are different (more multipath, simpler environment). There still remains a need for outdoor validation of such algorithms.

3D real-time localization results

Figure 6.7 presents MCMC results for a 3D-SAR real-time experiment using the C2 function. The localization results are provided in Table 6.4, with aperture length L, error ϵ between reference position

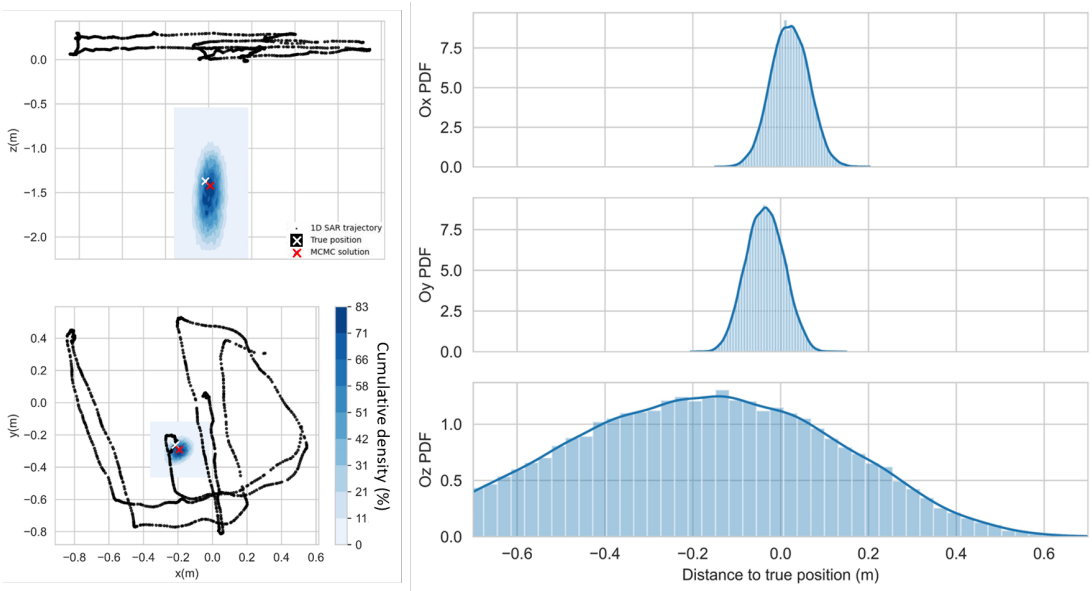

FIGURE 6.7 MCMC localization results for a tag with a 3D trajectory. (Left) 3D densities in xOy and xOz planes. (Right) MCMC density projected on every axis.

and MCMC distribution average, and distribution standard deviation σ. Note that the MCMC solution error is consistently comparable to the standard deviation score (interpreted as an "error bar"). The relatively short vertical aperture results in a higher deviation than in the horizontal plane. This partly explains the higher error, along with the higher vertical sensitivity of the system (see Section 6.5).

Direction	Aperture length (m)	Localization error (m)	Standard deviation (m)
X	1.6	0.02	0.015
Y	1.2	0.02	0.015
Z	0.25	0.08	0.1

TABLE 6.4 Summary of the 3D-SAR localization results.

Discussion on main error directions

In the context of a mainly horizontal trajectory, the xOy and Oz estimations are often discriminated because they don't rely on the exact same inversion approach. Namely, the SAR horizontal aperture can provide a high precision in the xOy plane, whereas additional information is often needed for Oz, such as Lidar, IMU or other altitude measurement devices. Figure 6.7 shows qualitatively that MCMC space parameters are correlated, which challenges this horizontal/vertical separation. The

Experiment	Air	Hay	Bark	Bark/Hay	Snow	3D
yOz corr.coef	0.15	0.26	0.22	0.34	0.3	0.41

TABLE 6.5 Correlation coefficient between Oy et Oz parameters in the MCMC distribution, for various localization experiments.

strong correlation that can appear between vertical and horizontal parameters is an additional source of error. It is expected that the main error directions are not aligned with the XYZ inversion frame, and MCMC allows for a detailed analysis of these directions. Table 6.5 presents correlation coefficients between Oy and Oz parameters, in the yOz plane (or perpendicular to 1D trajectory, when applicable). Note that the highest 1D scores are reached in the most RF-sensitive media (heterogeneous and high permittivity : bark/hay and snow), indicating that multipath-rich environments also reshape the cost function's main directions. The higher correlation in the 3D case is also an effect of the trajectory, which is not symmetrical nor uniformly sampled. This highlights the necessity to identify eigenvectors of the MCMC distribution and compare them to the usual horizontal-vertical directions.

6.7 Conclusion and perspectives

This paper presents various advances aiming towards centimeter localization with SAR-RFID devices, in outdoor conditions. The numerous sources of error of the method, and the corresponding hardware and software choices, were listed in an operational manner. The feasibility of localization under vegetation and snow cover was demonstrated, and limitations concerning moisture content and medium homogeneity were highlighted. Localization errors under vegetation do not exceed 5 cm in the vertical direction, and 1 cm in the horizontal plane. Under snow, the vertical localization error was about 10 cm, and 4 cm in the horizontal plane. Two cost functions were compared for SAR inversion, highlighting that phase unwrapping resolves solution ambiguities, but lowers the vertical precision. Three antenna tracking methods were compared, namely tacheometry / RTK / PPK and showed that PPK was best adapted for landslide monitoring purposes. An optimization algorithm based on Markov-Chain Monte Carlo was employed for inversion, providing both high accuracy and estimation of parameter covariance. Real-time measurements performed with a handheld SAR-RFID structure, demonstrated centimeter accuracy and precision in the horizontal plane. As expected the vertical accuracy of SAR-RFID is the lowest and most sensitive to multipath interference from the propagation environment. Various

solutions to this issue could be for example : a diversified trajectory lowering the sensitivity to vertical direction, or the use of a lidar or accelerometer to provide a more stable vertical position.

The overall SAR-RFID system suggests interesting perspectives of improvement, notably concerning better antenna positioning using for example GPS-IMU fusion, and of course real UAV monitoring on landslides. As a side-use, this method can also be used for material sensing by exploiting the RF disturbance of snow or vegetation. SAR-RFID approach is promising for landslide surface monitoring. More experiments are needed in vegetated and snowy environments, especially in humid scenarios. UAV measurements showed that research efforts should be dedicated to estimate and correct the lever-arm effect from GNSS rover to antenna center.

The cultivated field above the landslide is affected every year by the headscarp progression. On the bottom picture, the wheat that was sown before the scarp retrogression could not be harvested.

Chapter 7

Conclusion

In this conclusive section, we will summarize the key results of this research work, then discuss the current limitations of the approach, and finally propose perspectives for future research work.

7.1 Key findings and conclusions

Signal processing approaches were developed in order to enhance the RFID data, exploiting redundancies and tag group behavior (Chapter 2). Fusion operators were implemented to merge multi-frequency, multi-antenna and multi-tag phase data, with data availability increasing from 3% to 38% depending on the site. A guided-unwrapping approach was used to better unwrap partially-read tags, which reduced the number of unwrapping errors by more than 50% on the studied site.

In parallel to deterministic processing, a stochastic Kalman smoothing approach was developed (Chapter 3). Based on a simple position-velocity model, the smoother produced accurate results with improved features compared to the previous deterministic approaches. Namely, implicit phase unwrapping was demonstrated based on the velocity continuity hypothesis, and inter-tag coupling was introduced in order to complete partial data. Additionally, the Kalman covariance matrix is a promising indicator of the localization quality, and can be exploited to discriminate true displacements from multipath-induced artifacts.

Following the prior validation of 1D monitoring capabilities in an outdoor environment [Le Breton et al., 2019] using RFID tags, we demonstrated 2D monitoring at a centimeter level (Chapter 4). The study of the sensitivity of 3D localization highlighted the importance of the reader antenna system aperture, as well as the higher sensitivity in the vertical direction. In the current scenarios, centimeter accuracy can be expected in the horizontal plane. 2D monitoring presents notable advantages compared to 1D. Namely, a lower sensitivity to fast displacement because of higher ambiguity zones, hence an increased robustness to fast displacement ; the possibility to identify changes in direction of movement ; the potential resolution of rotational movements by exploiting multi-tag information. All these advantage open new application perspectives.

The two years of data acquired on the Harmalière landslide provided fruitful insights on landslide kinematics (Chapter 5). Supported by a clustering approach and multi-method monitoring, several landslide activation phases were identified along with sub-daily kinematics behavior. The results suggest a cascading triggering mechanism, between interacting landslides blocks. The synchronicity between surface creep (deduced from RFID) and soil properties variation (from dV/V) was pointed. This synchronicity was interpreted in light of the hydrological data. Although every surface acceleration was linked to hydrological events (rainfall, high water table), the hydrological inputs do not entirely dictate the landslide activity. By providing insights on the damaged volume below the surface, and on its potential healing, the dV/V series allowed a finer understanding of the inner landslide mechanisms. In general, most notable dV/V changes were directly correlated to surface activity. Thanks to the 2D-RFID estimation of tag displacement, a retrogressive behavior was identified, correlated to strong dV/V changes and a large advance of the landslide scarp. Multi-method monitoring using notably RFID and dV/V, hence proved its interest on this applied case.

Synthetic Aperture Radar was applied to outdoor tag localization (Chapter 6), with the objective of localizing and tracking tags using UAVs with a centimeter accuracy. A set of field experiments highlighted the challenging aspects of such methods, both technically and theoretically. Laboratory experiments demonstrated centimeter accuracy with snow and vegetation cover, and a novel optimization method was applied based on Markov-Chain Monte-Carlo. This method is especially fit for the SAR-RFID problem, because it allows global minimization of non-convex functions, and it provides a

covariance matrix in the parameter space. Real-time measurements performed on a handheld structure demonstrated centimeter resolution in the horizontal plane.

This thesis showed the possibility to localize and track RFID tags on a landslide surface. Through a variety of approaches and measurement systems, we have shown the growing potential of RFID landslide monitoring. Thanks to 2D/3D localization, a fine understanding of landslide kinematics can be reached. The data fusion and Kalman smoothing approaches bring RFID monitoring towards improved data robustness. This opens the way to go beyond observation, towards hazard securing and early warning systems. The potential of UAV-RFID localization was demonstrated as well, with promising applications in large landslides monitoring under vegetation and snow cover. Considering the above, we can conclude that RFID landslide monitoring proved its potential, and was further developed towards more robust, more accurate and more wide-scale methods.

7.2 Current limitations of the approach

Besides the promises of RFID landslide monitoring, we shall point out the limitations and lines of improvement that are currently identified.

As of now, the tag read range is a key issue for system upscaling : the ability to track tags further than 100 m via fixed antennas, or to localize them with UAV under 30 m-high trees, would be extremely beneficial for the method. Currently the range of applications is limited by the relatively low read range of RFID systems.

Another remaining challenge of outdoor RFID systems is data robustness or enhancement. Although RFID provides valuable all-weather, long-term and low-cost access to surface displacement, the noisy and variable-quality datasets (compared to more stable measurements such as extensometer or total station) pose specific issues. This high variability challenges the data-processing methods that were developed, such as phase unwrapping or data fusion algorithms. It has been an ongoing challenge to implement robust (deterministic) algorithms, and there is now a need for stochastic methods to take advantage of the varying measurement accuracy. Several improvements have already been brought herein (Chapter 2 and 3) and elsewhere [Tsanousa et al., 2022, Wan et al., 2022], opening promising perspectives for the future.

Most approaches presented in this work only consider relative ranging, which is of limited interest compared to absolute ranging. This is related to the relative nature of Phase Difference of Arrival (PDoA) measurements. Although this is an important drawback of the method, we will discuss ways of bypassing it in the next section.

Concerning the RF measurement itself, multipath interference is another major issue for any RFID measurement. This has been thoroughly tackled in indoors scenarios, where multipath can be simulated thanks to flat surfaces and predictable evolution in the interference patterns. But in outdoors scenario, with complex topography and the presence of vegetation or snow, multipath interference is virtually impossible to simulate. Ideal cases can be studied, such as a flat ground surface with a homogeneous snow layer (Chapter 4), but the general case does not yet seem computable.

7.3 Perspectives and future work

Future of RFID landslide monitoring

This work showed the potential of RFID landslide monitoring, both in terms of data processing improvement and of geomorphological interpretation. This section will discuss a few development perspectives that can be foreseen, in the continuity of this work.

First, as the main advantage of the method is the cost-per-point, increasing the number of tags on the observation site would be a simple but effective improvement. This is one of the main arguments for developing RFID in environmental monitoring, as it provides space-time oversampling with virtually no limit on the number of tags : it becomes possible to densely map the true displacement field of a landslide on a dense grid, under vegetation and snow, at a relatively low cost.

Then, related to the previous point, as the range of RFID tags is a strong limitation nowadays, improving it is a key challenge for developing the method. Other works have already shown interesting results, notably exploiting the quantum tunnelling effect on 5.8 GHz semi-passive tags and reaching up to a 1-kilometer read range [Amato et al., 2018].

We should also point out the numerous environmental sensing capabilities of RFID tags, apart from solely propagation-based remote sensing. Tags equipped with moisture sensors have already been used for landslide monitoring [Pichorim et al., 2018]. Along with temperature [Amin and Karmakar, 2011], pressure [Brinker and Zoughi, 2022], pH [Potyrailo et al., 2011] or strain sensing [Occhiuzzi et al., 2011], RFID offers a vast set of quantities to monitor. Combined with the many advantages described in this work, environmental sensing with RFID will surely continue to foster earth science monitoring in the future.

Next the subject of noisy and redundant data remains widely unexplored for our application. Although notable improvements have already been demonstrated notably in this work [Le Breton et al., 2017,Charléty et al., 2022a,Charléty et al., 2023b], we still lack a systematic approach for RFID localization that would be adaptive to the data context. Taking inspiration from the GPS techniques [Drawil et al., 2012], we could develop data quality indices associated to corresponding ranging methods, with comprehensive phase ambiguity resolution. To that end, Kalman data fusion algorithms seem promising for optimally merging different ranging methods (relative and absolute) featuring variable accuracies [Gan and Harris, 2001]. As an example, absolute RFID ranging has been recently improved thanks to the increased ETSI band [Mathieu, 2023]. Such fusion architectures are analysed by [Sasiadek and Hartana, 2000]. or [Gao and Harris, 2002], and [Loffeld et al., 2007] applied fusion for 2D phase unwrapping. Using these approaches, optimal use of the RFID data could be reached with an absolute ranging objective.

Connected to the previous points, the clustering methods described in Chapter 5 have shown interesting although limited results. The relatively low number of tags in l'Harmalière, along with the variable noise levels and the clustering method itself, could be responsible for such results. We believe that with an increased number of tags and more adapted clustering methods, some kinematic landslide features could be detected automatically : triggering mechanism, retrogression, and general changes in behavior. The redundancy of our dataset is important and it has not yet been fully exploited.

Finally we shall discuss the future development of UAV-RFID landslide monitoring. UAV's have already shown great potential for earth-science applications [Antoine et al., 2020], including landslide

mapping and characterization [Niethammer et al., 2012, Rossi et al., 2018]. As shown in Chapter 6, one of the the main current barriers for improvement is the antenna's accurate positioning (linked to both GNSS accuracy and lever-arm effect), along with GNSS-RFID measurement synchronization. Presently, the GNSS accuracy issue is a quite active topic in environmental monitoring [Gilliot et al., 2022, Remzi et al., 2020, Tomaštík et al., 2019], and many improvements can be expected in the future. Concerning RFID landslide monitoring, several challenges have been tackled both hardware (measurement accuracy, synchronization) and theoretical (inversion methods). A few steps remain before proper in-flight localization can be performed, notably the validation of the lever-arm effect correction, and ideally the implementation of IMU-GNSS fusion for higher position accuracy [Gautam et al., 2019, You et al., 2020]. Moreover, the systematic implementation of additional on-board systems such as Lidar devices, could greatly enhance the quality and stability of UAV-RFID data acquisition [Opromolla et al., 2016, Qian et al., 2021]. In the future we anticipate the rise of UAV-flight automation for the daily monitoring of large geo-hazards. Indeed, as was observed during the numerous measurement campaigns of this work, the level of human effort needed for manual UAV-flight is high, and it even brings new sources of error in harsh environmental contexts. Such ideas about automation have already been discussed [Kingston et al., 2016, Gomez and Purdie, 2016], leading to the development of search-algorithms [Ivić et al., 2020] that could inspire UAV-RFID monitoring.

Low-cost sensors for environmental monitoring

Although my work was focused on RFID sensors specifically, it belongs to a global dynamic that goes beyond both RFID or landslides. Low-cost sensors applied to environmental monitoring have attracted research interest since more than a decade, for a variety of applications including weather monitoring [Strigaro et al., 2019], water resource management [Paul and Buytaert, 2018], soil moisture [Placidi et al., 2020], or pollution monitoring [Kumar and Gurjar, 2019]. The Internet of Things paradigm, along with easier access to data and diminished sensors cost, offers new perspectives for environmental measurements. As stated by [Mao et al., 2019], "while there are some trade-offs with regard to robustness, calibration requirements and accuracy of low cost sensors when compared to high–end commercial sensors, the potential for greatly increased spatial coverage will facilitate new insights into environmental process dynamics" ; this statement perfectly fits the present work. Thanks to the readiness and accessibility of low-cost off-the-shelf sensors, open-science and participative research are

expected to "make knowledge creation and governance more multidirectional, decentralized, diverse, and inclusive" [Paul and Buytaert, 2018]. As an example, water table level and discharge measurement systems usually necessitate complex maintenance that confines them to large institutions or government entities : low-cost hydrological sensors could hence be considered as a means to complement institutionalized data collection.

The benefits of such low-cost devices could be even greater in low-income countries, especially in regions where conventional observation systems are insufficient. As explained by [Strigaro et al., 2019] concerning weather monitoring, this could help address the low resilience and adaptation capacity of low-income economies, enabling "monitoring local phenomena in real-time and through dense (in time and space) observations". These sensors are very attractive due to their near real-time availability with a high spatio-temporal resolution and, therefore, potentially able to fill the long-standing gap in detecting local activities that go unnoticed in various geographic locations.

The main issue to address with this kind of sensors is the data quality issue, as explained in Chapter 2 and 3. If decisions are to be taken based on these sensor networks, data should be most reliable and accurate. At a higher level, the absence of standards for data and metadata concerning these sensors is also a crucial point [Strigaro et al., 2019].

Remote sensing and environmental monitoring

Although this work mainly focused on direct RF models, rarely taking the propagation environment into account, interactions between RF and the medium actually provide vast quantities of information. This is the basis of remote sensing, including satellite-based observation of vegetation [Xue et al., 2017], RFID for snow depth estimation [Le Breton et al., 2023b] or vegetation depth [Le Breton et al., 2023a], and other numerous methods [Weiss et al., 2020, Li et al., 2020]. Among the broad applications of remote sensing to environmental monitoring, one that particularly attracted my attention are the so-called "opportunistic measurements". Using the intensive communication flux of either the Internet [Casado et al., 2005], telephony [Nemati et al., 2017], or any other information propagation medium as a means of probing it, stands out as a surprising, innovative and low-cost approach. At the frontier between Radio-Frequencies, signal processing and low-cost sensing, the example of Commercial Microwave Links

is eloquent in this regard. Several works have described the possibility to estimate rainfall through the radio-link signal attenuation of telephony networks [Chwala and Kunstmann, 2019], which allows the production of rainfall maps at scales from city [Djibo et al., 2023, Turko et al., 2021] to country [Graf et al., 2020]. In this kind of application, the issues concerning antenna sensitivity to environmental changes, multipath phenomena, and inversion of noisy data, relate closely to the RFID monitoring scenario presented in this work.

Bibliography

[pyu,] Mayer Analytics. pyUBX https://github.com/mayeranalytics/pyUBX.

[PyU,] Python. numpy unwrap.
https://numpy.org/doc/stable/reference /generated/numpy.unwrap.html
Accessed: 2022-11-16.

[Abugabah et al., 2020] Abugabah, A., Nizamuddin, N., and Abuqabbeh, A. (2020). A review of challenges and barriers implementing rfid technology in the healthcare sector. *Procedia Computer Science*, 170:1003–1010.

[Ajourlou et al., 2019] Ajourlou, P., Samiei Esfahany, S., and Safari, A. (2019). A new strategy for phase unwrapping in insar time series over areas with high deformation rate: Case study on the southern tehran subsidence. *International Archives of the Photogrammetry, Remote Sensing & Spatial Information Sciences*.

[Alam et al., 2017] Alam, F., Mehmood, R., Katib, I., Albogami, N. N., and Albeshri, A. (2017). Data fusion and iot for smart ubiquitous environments: A survey. *Ieee Access*, 5:9533–9554.

[Alkan et al., 2020] Alkan, R. M., Erol, S., Ozulu, I. M., and Ilci, V. (2020). Accuracy comparison of post-processed ppp and real-time absolute positioning techniques. *Geomatics, Natural Hazards and Risk*, 11(1):178–190.

[Amato et al., 2018] Amato, F., Torun, H. M., and Durgin, G. D. (2018). Rfid backscattering in long-range scenarios. *IEEE Transactions on Wireless Communications*, 17(4):2718–2725.

[Amin and Karmakar, 2011] Amin, E. M. and Karmakar, N. (2011). Development of a chipless rfid temperature sensor using cascaded spiral resonators. In *SENSORS, 2011 IEEE*, pages 554–557. IEEE.

[Angeli et al., 1996] Angeli, M.-G., Gasparetto, P., Menotti, R. M., Pasuto, A., and Silvano, S. (1996). A visco-plastic model for slope analysis applied to a mudslide in cortina d'ampezzo, italy. *Quarterly Journal of Engineering Geology*, 29(3):233–240.

[Angelino et al., 2012] Angelino, C. V., Baraniello, V. R., and Cicala, L. (2012). Uav position and attitude estimation using imu, gnss and camera. In *2012 15th International Conference on Information Fusion*, pages 735–742. IEEE.

[Ansari et al., 2020] Ansari, M. Y., Ahmad, A., Khan, S. S., Bhushan, G., and Mainuddin (2020). Spatiotemporal clustering: a review. *Artificial Intelligence Review*, 53:2381–2423.

[Antoine et al., 2020] Antoine, R., Lopez, T., Tanguy, M., Lissak, C., Gailler, L., Labazuy, P., and Fauchard, C. (2020). Geoscientists in the sky: Unmanned aerial vehicles responding to geohazards. *Surveys in Geophysics*, 41:1285–1321.

[Anton and Rorres, 2013] Anton, H. and Rorres, C. (2013). *Elementary linear algebra: applications version*. John Wiley & Sons.

[Arnitz et al., 2010] Arnitz, D., Mühlmann, U., and Witrisal, K. (2010). Uwb ranging in passive uhf rfid: Proof of concept. *Electronics letters*, 46(20):1401–1402.

[Arnold, 1973] Arnold, L. (1973). *Stochastic differential equations, Theory and Applications*. Wiley Interscience.

[Arthaber et al., 2015] Arthaber, H., Faseth, T., and Galler, F. (2015). Spread-spectrum based ranging of passive uhf epc rfid tags. *IEEE Communications Letters*, 19(10):1734–1737.

[Aryal et al., 2012] Aryal, A., Brooks, B. A., Reid, M. E., Bawden, G. W., and Pawlak, G. R. (2012). Displacement fields from point cloud data: Application of particle imaging velocimetry to landslide geodesy. *Journal of Geophysical Research: Earth Surface*, 117(F1).

[Azarfar et al., 2021] Azarfar, A., Barbot, N., and Perret, E. (2021). Chipless rfid based on micro-doppler effect. *IEEE Transactions on Microwave Theory and Techniques*, 70(1):766–778.

[Azzouzi et al., 2011] Azzouzi, S., Cremer, M., Dettmar, U., Kronberger, R., and Knie, T. (2011). New measurement results for the localization of uhf rfid transponders using an angle of arrival (aoa) approach. In *2011 IEEE International Conference on RFID*, pages 91–97. IEEE.

[Balaji et al., 2020] Balaji, R., Malathi, R., Priya, M., and Kannammal, K. (2020). A comprehensive nomenclature of rfid localization. In *2020 International Conference on Computer Communication and Informatics (ICCCI)*, pages 1–9. IEEE.

[Bandini et al., 2022] Bandini, G., Motroni, A., Buffi, A., Marracci, M., and Tellini, B. (2022). On the effect of position uncertainty of the uhf-rfid reader trajectory in sar-based localization via uav. In *2022 IEEE International Symposium on Measurements & Networking (M&N)*, pages 1–6. IEEE.

[Banerjee et al., 1997] Banerjee, P., Bose, A., and Mathur, B. (1997). A study on gps pdop and its impact on position error.

[Bekkali et al., 2007] Bekkali, A., Sanson, H., and Matsumoto, M. (2007). Rfid indoor positioning based on probabilistic rfid map and kalman filtering. In *Third IEEE International Conference on Wireless and Mobile Computing, Networking and Communications (WiMob 2007)*, pages 21–21. IEEE.

[Beniston et al., 2018] Beniston, M., Farinotti, D., Stoffel, M., Andreassen, L. M., Coppola, E., Eckert, N., Fantini, A., Giacona, F., Hauck, C., Huss, M., et al. (2018). The european mountain cryosphere: a review of its current state, trends, and future challenges. *The Cryosphere*, 12(2):759–794.

[Benoit et al., 2015] Benoit, L., Briole, P., Martin, O., Thom, C., Malet, J.-P., and Ulrich, P. (2015). Monitoring landslide displacements with the geocube wireless network of low-cost gps. *Engineering Geology*, 195:111–121.

[Bernardie et al., 2015] Bernardie, S., Desramaut, N., Malet, J.-P., Gourlay, M., and Grandjean, G. (2015). Prediction of changes in landslide rates induced by rainfall. *Landslides*, 12:481–494.

[Bernardini et al., 2020a] Bernardini, F., Buffi, A., Fontanelli, D., Macii, D., Magnago, V., Marracci, M., Motroni, A., Nepa, P., and Tellini, B. (2020a). Robot-based indoor positioning of uhf-rfid tags: The sar method with multiple trajectories. *IEEE Transactions on Instrumentation and Measurement*, 70:1–15.

[Bernardini et al., 2020b] Bernardini, F., Buffi, A., Motroni, A., Nepa, P., Tellini, B., Tripicchio, P., and Unetti, M. (2020b). Particle swarm optimization in sar-based method enabling real-time 3d positioning of uhf-rfid tags. *IEEE Journal of Radio Frequency Identification*, 4(4):300–313.

[Bièvre et al., 2021] Bièvre, G., Jongmans, D., Lebourg, T., and Carrière, S. (2021). Electrical resistivity monitoring of an earthslide with electrodes located outside the unstable zone (pont-bourquin landslide, swiss alps). *Near Surface Geophysics*, 19(2):225–239.

[Bièvre et al., 2011] Bièvre, G., Kniess, U., Jongmans, D., Pathier, E., Schwartz, S., van Westen, C. J., Villemin, T., and Zumbo, V. (2011). Paleotopographic control of landslides in lacustrine deposits (trièves plateau, french western alps). *Geomorphology*, 125(1):214–224.

[Bisnath et al., 2004] Bisnath, S., Wells, D., Santos, M., and Cove, K. (2004). Initial results from a long baseline, kinematic, differential gps carrier phase experiment in a marine environment. In *PLANS 2004. Position Location and Navigation Symposium (IEEE Cat. No. 04CH37556)*, pages 625–631. IEEE.

[Bittelli et al., 2012] Bittelli, M., Valentino, R., Salvatorelli, F., and Pisa, P. R. (2012). Monitoring soil-water and displacement conditions leading to landslide occurrence in partially saturated clays. *Geomorphology*, 173:161–173.

[Bláha et al., 2012] Bláha, M., Eisenbeiss, H., Grimm, D., and Limpach, P. (2012). Direct georeferencing of uavs. *The International Archives of the Photogrammetry, Remote Sensing and Spatial Information Sciences*, 38:131–136.

[Bogaard et al., 2007] Bogaard, T., Guglielmi, Y., Marc, V., Emblanch, C., Bertrand, C., and Mudry, J. (2007). Hydrogeochemistry in landslide research: a review. *Bulletin de la Société Géologique de France*, 178(2):113–126.

[Bontemps et al., 2020] Bontemps, N., Lacroix, P., Larose, E., Jara, J., and Taipe, E. (2020). Rain and small earthquakes maintain a slow-moving landslide in a persistent critical state. *Nature Communications*, 11(1):780.

[Boursianis et al., 2022] Boursianis, A. D., Papadopoulou, M. S., Diamantoulakis, P., Liopa-Tsakalidi, A., Barouchas, P., Salahas, G., Karagiannidis, G., Wan, S., and Goudos, S. K. (2022). Internet of things (iot) and agricultural unmanned aerial vehicles (uavs) in smart farming: A comprehensive review. *Internet of Things*, 18:100187.

[Breton et al., 2021] Breton, M. L., Liébault, F., Baillet, L., Charléty, A., Éric Larose, and Tedjini, S. (2021). Dense and longdterm monitoring of earth surface processes with passive rfid – a review.

[Brinker and Zoughi, 2022] Brinker, K. and Zoughi, R. (2022). Tunable chipless rfid pressure sensor utilizing additive manufacturing. In *2022 IEEE International Instrumentation and Measurement Technology Conference (I2MTC)*, pages 1–6. IEEE.

[Buffi et al., 2018] Buffi, A., Motroni, A., Nepa, P., Tellini, B., and Cioni, R. (2018). A sar-based measurement method for passive-tag positioning with a flying uhf-rfid reader. *IEEE Transactions on Instrumentation and Measurement*, 68(3):845–853.

[Buffi et al., 2017] Buffi, A., Nepa, P., and Cioni, R. (2017). Sarfid on drone: Drone-based uhf-rfid tag localization. In *2017 IEEE International Conference on RFID Technology & Application (RFID-TA)*, pages 40–44. IEEE.

[Buffi et al., 2014] Buffi, A., Nepa, P., and Lombardini, F. (2014). A phase-based technique for localization of uhf-rfid tags moving on a conveyor belt: Performance analysis and test-case measurements. *IEEE Sensors Journal*, 15(1):387–396.

[Cai et al., 2022] Cai, J., Liu, G., Jia, H., Zhang, B., Wu, R., Fu, Y., Xiang, W., Mao, W., Wang, X., and Zhang, R. (2022). A new algorithm for landslide dynamic monitoring with high temporal resolution by kalman filter integration of multiplatform time-series insar processing. *International Journal of Applied Earth Observation and Geoinformation*, 110:102812.

[Calvello et al., 2016] Calvello, M., Papa, M. N., Pratschke, J., and Nacchia Crescenzo, M. (2016). Landslide risk perception: a case study in southern italy. *Landslides*, 13:349–360.

[Carlà et al., 2019] Carlà, T., Tofani, V., Lombardi, L., Raspini, F., Bianchini, S., Bertolo, D., Thuegaz, P., and Casagli, N. (2019). Combination of gnss, satellite insar, and gbinsar remote sensing monitoring to improve the understanding of a large landslide in high alpine environment. *Geomorphology*, 335:62–75.

[Carrel et al.,] Carrel, M., Gassner, J., Stähly, S., and Wahlen, S. Interferometric radar monitoring of the spitze stei landslide under challenging conditions.

[Carrière et al., 2018] Carrière, S. R., Bièvre, G., Jongmans, D., Chambon, G., Bellot, H., and Lebourg, T. (2018). Measurement of geophysical parameters on clay samples at the solid–fluid transition. *Near Surface Geophysics*, 16(1):23–37.

[Casado et al., 2005] Casado, M., Garfinkel, T., Cui, W., Paxson, V., and Savage, S. (2005). Opportunistic measurement: Extracting insight from spurious traffic. In *Proc. 4th ACM Workshop on Hot Topics in Networks (Hotnets-IV)*.

[Casagli et al., 2017] Casagli, N., Frodella, W., Morelli, S., Tofani, V., Ciampalini, A., Intrieri, E., Raspini, F., Rossi, G., Tanteri, L., and Lu, P. (2017). Spaceborne, uav and ground-based remote sensing techniques for landslide mapping, monitoring and early warning. *Geoenvironmental Disasters*, 4:1–23.

[Casagli et al., 2023] Casagli, N., Intrieri, E., Tofani, V., Gigli, G., and Raspini, F. (2023). Landslide detection, monitoring and prediction with remote-sensing techniques. *Nature Reviews Earth & Environment*, 4(1):51–64.

[Casati et al., 2017] Casati, G., Longhi, M., Latini, D., Carbone, F., Amendola, S., Del Frate, F., Schiavon, G., and Marrocco, G. (2017). The interrogation footprint of rfid-uav: Electromagnetic modeling and experimentations. *IEEE Journal of Radio Frequency Identification*, 1(2):155–162.

[Cassel et al., 2017] Cassel, M., Dépret, T., and Piégay, H. (2017). Assessment of a new solution for tracking pebbles in rivers based on active rfid. *Earth Surface Processes and Landforms*, 42(13):1938–1951.

[Cassel et al., 2020] Cassel, M., Piégay, H., Fantino, G., Lejot, J., Bultingaire, L., Michel, K., and Perret, F. (2020). Comparison of ground-based and uav a-uhf artificial tracer mobility monitoring methods on a braided river. *Earth Surface Processes and Landforms*, 45(5):1123–1140.

[Causes, 2001] Causes, L. (2001). Landslide types and processes. *US Geological Survey: Reston, VA, USA*.

[Chae et al., 2017] Chae, B.-G., Park, H.-J., Catani, F., Simoni, A., and Berti, M. (2017). Landslide prediction, monitoring and early warning: a concise review of state-of-the-art. *Geosciences Journal*, 21:1033–1070.

[Charléty et al., 2022a] Charléty, A., Le Breton, M., Baillet, L., and Larose, E. (2022a). Long-term monitoring of soil surface deformation with rfid. In *2022 IEEE 12th International Conference on RFID Technology and Applications (RFID-TA)*, pages 101–104. IEEE.

[Charléty et al., 2023a] Charléty, A., Le Breton, M., Baillet, L., and Larose, E. (2023a). Rfid landslide monitoring: long-term outdoor signal processing and phase unwrapping. *IEEE Journal of Radio Frequency Identification*.

[Charléty et al., 2022b] Charléty, A., Le Breton, M., Larose, E., and Baillet, L. (2022b). 2d phase-based rfid localization for on-site landslide monitoring. *Remote Sensing*, 14(15):3577.

[Charléty et al., 2023b] Charléty, A., Michel, O. J., and Le Breton, M. (2023b). Kalman smoothing for better rfid landslide monitoring. In *EUSIPCO 2023*.

[Charléty et al., 2023] Charléty, A., Breton, M. L., Baillet, L., and Larose, E. (2023). RFID landslide monitoring : long-term outdoor signal processing and phase unwrapping.

[Chatzistefanou et al., 2021] Chatzistefanou, A. R., Tzitzis, A., Megalou, S., Sergiadis, G., and Dimitriou, A. G. (2021). Trajectory-tracking of uhf rfid tags, exploiting phase measurements collected from fixed antennas. *IEEE Journal of Radio Frequency Identification*, 5(2):191–206.

[Chawla and Ha, 2007] Chawla, V. and Ha, D. S. (2007). An overview of passive rfid. *IEEE Communications Magazine*, 45(9):11–17.

[Chib and Greenberg, 1995] Chib, S. and Greenberg, E. (1995). Understanding the metropolis-hastings algorithm. *The american statistician*, 49(4):327–335.

[Cho et al., 2005] Cho, C., Choo, H., and Park, I. (2005). Broadband rfid tag antenna with quasi-isotropic radiation pattern. *Electronics Letters*, 41(20):1091–1092.

[Chwala and Kunstmann, 2019] Chwala, C. and Kunstmann, H. (2019). Commercial microwave link networks for rainfall observation: Assessment of the current status and future challenges. *Wiley Interdisciplinary Reviews: Water*, 6(2):e1337.

[Ch'ng et al., 2019] Ch'ng, S.-F., Khosravian, A., Doan, A.-D., and Chin, T.-J. (2019). Outlier-robust manifold pre-integration for ins/gps fusion. In *2019 IEEE/RSJ International Conference on Intelligent Robots and Systems (IROS)*, pages 7489–7496. IEEE.

[Cledat et al., 2020] Cledat, E., Jospin, L. V., Cucci, D. A., and Skaloud, J. (2020). Mapping quality prediction for rtk/ppk-equipped micro-drones operating in complex natural environment. *ISPRS Journal of Photogrammetry and Remote Sensing*, 167:24–38.

[Colesanti and Wasowski, 2006] Colesanti, C. and Wasowski, J. (2006). Investigating landslides with space-borne synthetic aperture radar (sar) interferometry. *Engineering geology*, 88(3-4):173–199.

[Conn et al., 2000] Conn, A. R., Gould, N. I., and Toint, P. L. (2000). *Trust region methods*. SIAM.

[Corominas et al., 2000] Corominas, J., Moya, J., Lloret, A., Gili, J., Angeli, M., Pasuto, A., and Silvano, S. (2000). Measurement of landslide displacements using a wire extensometer. *Engineering Geology*, 55(3):149–166.

[Crowley and Demazeau, 1993] Crowley, J. L. and Demazeau, Y. (1993). Principles and techniques for sensor data fusion. *Signal processing*, 32(1-2):5–27.

[Cui et al., 2019] Cui, Y., Cheng, D., Choi, C. E., Jin, W., Lei, Y., and Kargel, J. S. (2019). The cost of rapid and haphazard urbanization: lessons learned from the freetown landslide disaster. *Landslides*, 16:1167–1176.

[Daakir et al., 2016] Daakir, M., Pierrot-Deseilligny, M., Bosser, P., Pichard, F., Thom, C., and Rabot, Y. (2016). Study of lever-arm effect using embedded photogrammetry and on-board gps receiver on uav for metrological mapping purpose and proposal of a free ground measurements calibration procedure. *The International Archives of the Photogrammetry, Remote Sensing and Spatial Information Sciences*, 40:65–70.

[Dai et al., 2002] Dai, F., Lee, C. F., and Ngai, Y. Y. (2002). Landslide risk assessment and management: an overview. *Engineering geology*, 64(1):65–87.

[Delacourt et al., 2007] Delacourt, C., Allemand, P., Berthier, E., Raucoules, D., Casson, B., Grandjean, P., Pambrun, C., and Varel, E. (2007). Remote-sensing techniques for analysing landslide kinematics: a review. *Bulletin de la Société Géologique de France*, 178(2):89–100.

[Dematteis et al., 2022] Dematteis, N., Wrzesniak, A., Allasia, P., Bertolo, D., and Giordan, D. (2022). Integration of robotic total station and digital image correlation to assess the three-dimensional surface kinematics of a landslide. *Engineering Geology*, 303:106655.

[Deng et al., 2020] Deng, F., Zuo, P., Wen, K., and Wu, X. (2020). Novel soil environment monitoring system based on rfid sensor and lora. *Computers and Electronics in Agriculture*, 169:105169.

[DiGiampaolo and Martinelli, 2020] DiGiampaolo, E. and Martinelli, F. (2020). A multiple baseline approach to face multipath. *IEEE Journal of Radio Frequency Identification*, 4(4):314–321.

[Dille et al., 2022] Dille, A., Dewitte, O., Handwerger, A. L., d'Oreye, N., Derauw, D., Ganza Bamulezi, G., Ilombe Mawe, G., Michellier, C., Moeyersons, J., Monsieurs, E., et al. (2022). Accel-

eration of a large deep-seated tropical landslide due to urbanization feedbacks. *Nature Geoscience*, 15(12):1048–1055.

[Dini et al., 2021] Dini, B., Bennett, G. L., Franco, A. M., Whitworth, M. R., Cook, K. L., Senn, A., and Reynolds, J. M. (2021). Development of smart boulders to monitor mass movements via the internet of things: a pilot study in nepal. *Earth Surface Dynamics*, 9(2):295–315.

[Dini et al., 2020] Dini, B., Manconi, A., Loew, S., and Chophel, J. (2020). The punatsangchhu-i dam landslide illuminated by insar multitemporal analyses. *Scientific reports*, 10(1):8304.

[Djibo et al., 2023] Djibo, M., Chwala, C., Graf, M., Polz, J., Kunstmann, H., and Zougmoré, F. (2023). High-resolution rainfall maps from commercial microwave links for a data-scarce region in west africa. *Journal of Hydrometeorology*, 24(10):1847–1861.

[Dong et al., 2020] Dong, M., Wu, H., Hu, H., Azzam, R., Zhang, L., Zheng, Z., and Gong, X. (2020). Deformation prediction of unstable slopes based on real-time monitoring and deepar model. *Sensors*, 21(1):14.

[Drawil et al., 2012] Drawil, N. M., Amar, H. M., and Basir, O. A. (2012). Gps localization accuracy classification: A context-based approach. *IEEE Transactions on Intelligent Transportation Systems*, 14(1):262–273.

[Du et al., 2016] Du, K.-L., Swamy, M., Du, K.-L., and Swamy, M. (2016). Simulated annealing. *Search and Optimization by Metaheuristics: Techniques and Algorithms Inspired by Nature*, pages 29–36.

[Dubois et al., 2016] Dubois, L., Dauphin, S., and Rul, G. (2016). Le glissement du chambon: évolution du phénomène et gestion de crise.

[Eling et al., 2015] Eling, C., Wieland, M., Hess, C., Klingbeil, L., and Kuhlmann, H. (2015). Development and evaluation of a uav based mapping system for remote sensing and surveying applications. *The International Archives of the Photogrammetry, Remote Sensing and Spatial Information Sciences*, 40:233–239.

[Eom et al., 2011] Eom, K. H., Lee, S. J., Kyung, Y. S., Lee, C. W., Kim, M. C., and Jung, K. K. (2011). Improved kalman filter method for measurement noise reduction in multi sensor rfid systems. *Sensors*, 11(11):10266–10282.

[Falco et al., 2017] Falco, G., Pini, M., and Marucco, G. (2017). Loose and tight gnss/ins integrations: Comparison of performance assessed in real urban scenarios. *Sensors*, 17(2):255.

[Fall et al., 2006] Fall, M., Azzam, R., and Noubactep, C. (2006). A multi-method approach to study the stability of natural slopes and landslide susceptibility mapping. *Engineering geology*, 82(4):241–263.

[Fano, 2020] Fano, W. G. (2020). Introductory chapter: Causal models of electrical permittivity and magnetic permeability. In *Electromagnetic Field Radiation in Matter*. IntechOpen.

[Faseth et al., 2011] Faseth, T., Winkler, M., Arthaber, H., and Magerl, G. (2011). The influence of multipath propagation on phase-based narrowband positioning principles in uhf rfid. In *2011 IEEE-APS Topical Conference on Antennas and Propagation in Wireless Communications*, pages 1144–1147. IEEE.

[Feng et al., 2021] Feng, L., Intrieri, E., Pazzi, V., Gigli, G., and Tucci, G. (2021). A framework for temporal and spatial rockfall early warning using micro-seismic monitoring. *Landslides*, 18:1059–1070.

[Feng et al., 2018] Feng, W., Wang, J., Chen, Y., Wang, X., Ge, N., and Lu, J. (2018). Uav-aided mimo communications for 5g internet of things. *IEEE Internet of Things Journal*, 6(2):1731–1740.

[Feng et al., 2008] Feng, Y., Wang, J., et al. (2008). Gps rtk performance characteristics and analysis. *Positioning*, 1(13).

[Finnegan et al., 2021] Finnegan, N. J., Perkins, J. P., Nereson, A. L., and Handwerger, A. L. (2021). Unsaturated flow processes and the onset of seasonal deformation in slow-moving landslides. *Journal of Geophysical Research: Earth Surface*, 126(5):e2020JF005758.

[Fiolleau et al., 2019] Fiolleau, S., Borgniet, L., Jongmans, D., Bièvre, G., and Chambon, G. (2019). Using uav's imagery and lidar to accurately monitor harmalière (france) landslide evolution. In *Geophysical Research Abstracts*, volume 21.

[Fiolleau et al., 2020] Fiolleau, S., Jongmans, D., Bièvre, G., Chambon, G., Baillet, L., and Vial, B. (2020). Seismic characterization of a clay-block rupture in harmalière landslide, french western alps. *Geophysical Journal International*, 221(3):1777–1788.

[Fiolleau et al., 2021] Fiolleau, S., Jongmans, D., Bièvre, G., Chambon, G., Lacroix, P., Helmstetter, A., Wathelet, M., and Demierre, M. (2021). Multi-method investigation of mass transfer mechanisms in a retrogressive clayey landslide (harmalière, french alps). *Landslides*, 18:1981–2000.

[Fleisch, 2008] Fleisch, D. (2008). *A student's guide to Maxwell's equations*. Cambridge University Press.

[Fletcher et al., 2005] Fletcher, R., Marti, U. P., and Redemske, R. (2005). Study of uhf rfid signal propagation through complex media. In *2005 IEEE Antennas and Propagation Society International Symposium*, volume 1, pages 747–750. IEEE.

[Froude and Petley, 2018] Froude, M. J. and Petley, D. N. (2018). Global fatal landslide occurrence from 2004 to 2016. *Natural Hazards and Earth System Sciences*, 18(8):2161–2181.

[G., 1973] G., M. (1973). La transfluence durance-isère essai de synthèse du quaternaire du bassin du drac'(alpes françaises). *Géologie Alpine*, 49:57–118.

[Gan and Harris, 2001] Gan, Q. and Harris, C. J. (2001). Comparison of two measurement fusion methods for kalman-filter-based multisensor data fusion. *IEEE Transactions on Aerospace and Electronic systems*, 37(1):273–279.

[Gao and Harris, 2002] Gao, J. and Harris, C. J. (2002). Some remarks on kalman filters for the multisensor fusion. *Information Fusion*, 3(3):191–201.

[Gao et al., 2021] Gao, Y., Gao, Y., Liu, B., and Jiang, Y. (2021). Enhanced fault detection and exclusion based on kalman filter with colored measurement noise and application to rtk. *GPS Solutions*, 25:1–13.

[García et al., 2010] García, A., Hördt, A., and Fabian, M. (2010). Landslide monitoring with high resolution tilt measurements at the dollendorfer hardt landslide, germany. *Geomorphology*, 120(1-2):16–25.

[García-Fernández et al., 2020] García-Fernández, M., Álvarez López, Y., De Mitri, A., Castrillo Martínez, D., Álvarez-Narciandi, G., and Las-Heras Andrés, F. (2020). Portable and easily-deployable air-launched gpr scanner. *Remote Sensing*, 12(11):1833.

[Gareis et al., 2020] Gareis, M., Fenske, P., Carlowitz, C., and Vossiek, M. (2020). Particle filter-based sar approach and trajectory optimization for real-time 3d uhf-rfid tag localization. In *2020 IEEE International Conference on RFID (RFID)*, pages 1–8. IEEE.

[Gariano and Guzzetti, 2016] Gariano, S. L. and Guzzetti, F. (2016). Landslides in a changing climate. *Earth-Science Reviews*, 162:227–252.

[Gautam et al., 2019] Gautam, D., Lucieer, A., Watson, C., and McCoull, C. (2019). Lever-arm and boresight correction, and field of view determination of a spectroradiometer mounted on an unmanned aircraft system. *ISPRS Journal of Photogrammetry and Remote Sensing*, 155:25–36.

[Giannelos et al., 2021] Giannelos, E., Andrianakis, E., Skyvalakis, K., Dimitriou, A. G., and Bletsas, A. (2021). Robust rfid localization in multipath with phase-based particle filtering and a mobile robot. *IEEE Journal of Radio Frequency Identification*, 5(3):302–310.

[Gili et al., 2000] Gili, J. A., Corominas, J., and Rius, J. (2000). Using global positioning system techniques in landslide monitoring. *Engineering geology*, 55(3):167–192.

[Gilks et al., 1995] Gilks, W. R., Richardson, S., and Spiegelhalter, D. (1995). *Markov chain Monte Carlo in practice*. CRC press.

[Gilliot et al., 2022] Gilliot, J.-M., Hadjar, D., and Michelin, J. (2022). Potential of ultra-high-resolution uav images with centimeter gnss positioning for plant scale crop monitoring. *Remote Sensing*, 14(10):2391.

[Gobiet et al., 2014] Gobiet, A., Kotlarski, S., Beniston, M., Heinrich, G., Rajczak, J., and Stoffel, M. (2014). 21st century climate change in the european alps—a review. *Science of the total environment*, 493:1138–1151.

[Golub and Kahan, 1965] Golub, G. and Kahan, W. (1965). Calculating the singular values and pseudo-inverse of a matrix. *Journal of the Society for Industrial and Applied Mathematics, Series B: Numerical Analysis*, 2(2):205–224.

[Gomez and Purdie, 2016] Gomez, C. and Purdie, H. (2016). Uav-based photogrammetry and geocomputing for hazards and disaster risk monitoring–a review. *Geoenvironmental Disasters*, 3:1–11.

[Graf et al., 2020] Graf, M., Chwala, C., Polz, J., and Kunstmann, H. (2020). Rainfall estimation from a german-wide commercial microwave link network: optimized processing and validation for 1 year of data. *Hydrology and Earth System Sciences*, 24(6):2931–2950.

[Grêt et al., 2006] Grêt, A., Snieder, R., and Scales, J. (2006). Time-lapse monitoring of rock properties with coda wave interferometry. *Journal of Geophysical Research: Solid Earth*, 111(B3).

[Griffin and Durgin, 2009] Griffin, J. D. and Durgin, G. D. (2009). Complete link budgets for backscatter-radio and rfid systems. *IEEE Antennas and Propagation Magazine*, 51(2):11–25.

[Guillemot et al., 2020] Guillemot, A., Helmstetter, A., Larose, É., Baillet, L., Garambois, S., Mayoraz, R., and Delaloye, R. (2020). Seismic monitoring in the gugla rock glacier (switzerland): ambient noise correlation, microseismicity and modelling. *Geophysical Journal International*, 221(3):1719–1735.

[Guillemot et al., 2021] Guillemot, A., van Herwijnen, A., Larose, E., Mayer, S., and Baillet, L. (2021). Effect of snowfall on changes in relative seismic velocity measured by ambient noise correlation. *The Cryosphere*, 15(12):5805–5817.

[Gupta and Fernando, 2022] Gupta, A. and Fernando, X. (2022). Simultaneous localization and mapping (slam) and data fusion in unmanned aerial vehicles: Recent advances and challenges. *Drones*, 6(4):85.

[Guzzetti et al., 2020] Guzzetti, F., Gariano, S. L., Peruccacci, S., Brunetti, M. T., Marchesini, I., Rossi, M., and Melillo, M. (2020). Geographical landslide early warning systems. *Earth-Science Reviews*, 200:102973.

[Guzzetti et al., 2007] Guzzetti, F., Peruccacci, S., Rossi, M., and Stark, C. P. (2007). Rainfall thresholds for the initiation of landslides in central and southern europe. *Meteorology and atmospheric physics*, 98(3):239–267.

[Gylland et al., 2013] Gylland, A. S., Rueslåtten, H., Jostad, H. P., and Nordal, S. (2013). Microstructural observations of shear zones in sensitive clay. *Engineering Geology*, 163:75–88.

[Hamasaki et al., 2017] Hamasaki, E., Marui, H., and Furuya, G. (2017). Simulation model to predict landslide speed using velocity-dependent viscous damping. In *Advancing Culture of Living with Landslides: Volume 2 Advances in Landslide Science*, pages 579–586. Springer.

[Han and Cho, 2010] Han, K. and Cho, S. H. (2010). Advanced landmarc with adaptive k-nearest algorithm for rfid location system. In *2010 2nd IEEE InternationalConference on Network Infrastructure and Digital Content*, pages 595–598. IEEE.

[Handwerger et al., 2019] Handwerger, A. L., Huang, M.-H., Fielding, E. J., Booth, A. M., and Bürgmann, R. (2019). A shift from drought to extreme rainfall drives a stable landslide to catastrophic failure. *Scientific reports*, 9(1):1569.

[Haque et al., 2016] Haque, U., Blum, P., Da Silva, P. F., Andersen, P., Pilz, J., Chalov, S. R., Malet, J.-P., Auflič, M. J., Andres, N., Poyiadji, E., et al. (2016). Fatal landslides in europe. *Landslides*, 13:1545–1554.

[Haque et al., 2019] Haque, U., Da Silva, P. F., Devoli, G., Pilz, J., Zhao, B., Khaloua, A., Wilopo, W., Andersen, P., Lu, P., Lee, J., et al. (2019). The human cost of global warming: Deadly landslides and their triggers (1995–2014). *Science of the Total Environment*, 682:673–684.

[Hasan et al., 2018] Hasan, K. F., Feng, Y., and Tian, Y.-C. (2018). Gnss time synchronization in vehicular ad-hoc networks: Benefits and feasibility. *IEEE Transactions on Intelligent Transportation Systems*, 19(12):3915–3924.

[Havenith et al., 2003] Havenith, H.-B., Strom, A., Jongmans, D., Abdrakhmatov, A., Delvaux, D., and Tréfois, P. (2003). Seismic triggering of landslides, part a: Field evidence from the northern tien shan. *Natural hazards and earth system sciences*, 3(1/2):135–149.

[Helmstetter and Garambois, 2010] Helmstetter, A. and Garambois, S. (2010). Seismic monitoring of séchilienne rockslide (french alps): Analysis of seismic signals and their correlation with rainfalls. *Journal of Geophysical Research: Earth Surface*, 115(F3).

[Henriques Abreu et al., 2014] Henriques Abreu, P., Xavier, J., Castro Silva, D., Reis, L. P., and Petry, M. (2014). Using kalman filters to reduce noise from rfid location system. *The Scientific World Journal*, 2014.

[Hibert et al., 2012] Hibert, C., Grandjean, G., Bitri, A., Travelletti, J., and Malet, J.-P. (2012). Characterizing landslides through geophysical data fusion: Example of the la valette landslide (france). *Engineering Geology*, 128:23–29.

[Hillers et al., 2014] Hillers, G., Campillo, M., and Ma, K.-F. (2014). Seismic velocity variations at tcdp are controlled by mjo driven precipitation pattern and high fluid discharge properties. *Earth and Planetary Science Letters*, 391:121–127.

[Hoffman and Bester, 2020] Hoffman, A. J. and Bester, N.-P. (2020). Rss and phase kalman filter fusion for improved velocity estimation in the presence of real-world factors. *IEEE Journal of Radio Frequency Identification*, 5(1):75–93.

[Huang, 2021] Huang, Y. (2021). *Antennas: from theory to practice*. John Wiley & Sons.

[Hugenholtz et al., 2012] Hugenholtz, C. H., Moorman, B. J., Riddell, K., and Whitehead, K. (2012). Small unmanned aircraft systems for remote sensing and earth science research. *Eos, Transactions American Geophysical Union*, 93(25):236–236.

[Huggel et al., 2012] Huggel, C., Clague, J. J., and Korup, O. (2012). Is climate change responsible for changing landslide activity in high mountains? *Earth Surface Processes and Landforms*, 37(1):77–91.

[Huiting et al., 2013] Huiting, J., Flisijn, H., Kokkeler, A. B., and Smit, G. J. (2013). Exploiting phase measurements of epc gen2 rfid tags. In *2013 IEEE International Conference on RFID-Technologies and Applications (RFID-TA)*, pages 1–6. IEEE.

[Hungr et al., 2014] Hungr, O., Leroueil, S., and Picarelli, L. (2014). The varnes classification of landslide types, an update. *Landslides*, 11:167–194.

[Ilinca et al., 2022] Ilinca, V., Șandric, I., Chițu, Z., Irimia, R., and Gheuca, I. (2022). Uav applications to assess short-term dynamics of slow-moving landslides under dense forest cover. *Landslides*, 19(7):1717–1734.

[Intrieri et al., 2019] Intrieri, E., Carlà, T., and Gigli, G. (2019). Forecasting the time of failure of landslides at slope-scale: A literature review. *Earth-science reviews*, 193:333–349.

[Intrieri et al., 2018] Intrieri, E., Gigli, G., Gracchi, T., Nocentini, M., Lombardi, L., Mugnai, F., Frodella, W., Bertolini, G., Carnevale, E., Favalli, M., et al. (2018). Application of an ultra-wide band sensor-free wireless network for ground monitoring. *Engineering Geology*, 238:1–14.

[Intrieri et al., 2012] Intrieri, E., Gigli, G., Mugnai, F., Fanti, R., and Casagli, N. (2012). Design and implementation of a landslide early warning system. *Engineering Geology*, 147:124–136.

[ITU, 1992] ITU, R. (1992). Electrical characteristics of the surface of the earth. *ITU-R P. 523-7*.

[Iverson and Major, 1987] Iverson, R. M. and Major, J. J. (1987). Rainfall, ground-water flow, and seasonal movement at minor creek landslide, northwestern california: Physical interpretation of empirical relations. *Geological Society of America Bulletin*, 99(4):579–594.

[Ivić et al., 2020] Ivić, S., Crnković, B., Arbabi, H., Loire, S., Clary, P., and Mezić, I. (2020). Search strategy in a complex and dynamic environment: The mh370 case. *Scientific reports*, 10(1):19640.

[Jaboyedoff et al., 2012] Jaboyedoff, M., Oppikofer, T., Abellán, A., Derron, M.-H., Loye, A., Metzger, R., and Pedrazzini, A. (2012). Use of lidar in landslide investigations: a review. *Natural hazards*, 61(1):5–28.

[Jackson et al., 2018] Jackson, J., Davis, B., and Gebre-Egziabher, D. (2018). A performance assessment of low-cost rtk gnss receivers. In *2018 IEEE/ION Position, Location and Navigation Symposium (PLANS)*, pages 642–649. IEEE.

[Janos and Kuras, 2021] Janos, D. and Kuras, P. (2021). Evaluation of low-cost gnss receiver under demanding conditions in rtk network mode. *Sensors*, 21(16):5552.

[Janos et al., 2022] Janos, D., Kuras, P., and Ortyl, Ł. (2022). Evaluation of low-cost rtk gnss receiver in motion under demanding conditions. *Measurement*, 201:111647.

[Jazwinski, 2008] Jazwinski, A. (2008). *Stochastic Processes and Filtering Theory*. Dover.

[Jeong et al., 2019] Jeong, S., Ko, J., and Kim, J. (2019). The effectiveness of a wireless sensor network system for landslide monitoring. *IEEE Access*, 8:8073–8086.

[Jia et al., 2012] Jia, X., Feng, Q., Fan, T., and Lei, Q. (2012). Rfid technology and its applications in internet of things (iot). In *2012 2nd international conference on consumer electronics, communications and networks (CECNet)*, pages 1282–1285. IEEE.

[Jin et al., 2006] Jin, G.-y., Lu, X.-y., and Park, M.-S. (2006). An indoor localization mechanism using active rfid tag. In *IEEE International Conference on Sensor Networks, Ubiquitous, and Trustworthy Computing (SUTC'06)*, volume 1, pages 4–pp. IEEE.

[Jongmans et al., 2009] Jongmans, D., Bièvre, G., Renalier, F., Schwartz, S., Beaurez, N., and Orengo, Y. (2009). Geophysical investigation of a large landslide in glaciolacustrine clays in the trièves area (french alps). *Engineering geology*, 109(1-2):45–56.

[Kanungo, 2019] Kanungo, D. (2019). Ground based real time monitoring system using wireless instrumentation for landslide prediction. *Landslides: Theory, Practice and Modelling*, pages 105–120.

[Kingston et al., 2016] Kingston, D., Rasmussen, S., and Humphrey, L. (2016). Automated uav tasks for search and surveillance. In *2016 IEEE Conference on Control Applications (CCA)*, pages 1–8. IEEE.

[Klair et al., 2010] Klair, D. K., Chin, K.-W., and Raad, R. (2010). A survey and tutorial of rfid anti-collision protocols. *IEEE Communications surveys & tutorials*, 12(3):400–421.

[Kos et al., 2010] Kos, T., Markezic, I., and Pokrajcic, J. (2010). Effects of multipath reception on gps positioning performance. In *Proceedings ELMAR-2010*, pages 399–402. IEEE.

[Kramer and Kramer, 2016] Kramer, O. and Kramer, O. (2016). Scikit-learn. *Machine learning for evolution strategies*, pages 45–53.

[Krishnamurthi et al., 2020] Krishnamurthi, R., Kumar, A., Gopinathan, D., Nayyar, A., and Qureshi, B. (2020). An overview of iot sensor data processing, fusion, and analysis techniques. *Sensors*, 20(21):6076.

[Kumar and Gurjar, 2019] Kumar, A. and Gurjar, B. R. (2019). Low-cost sensors for air quality monitoring in developing countries–a critical view. *Asian Journal of Water, Environment and Pollution*, 16(2):65–70.

[Lacasse et al., 2009] Lacasse, S., Nadim, F., Lacasse, S., and Nadim, F. (2009). Landslide risk assessment and mitigation strategy. *Landslides–disaster risk reduction*, pages 31–61.

[Lacroix et al., 2019] Lacroix, P., Araujo, G., Hollingsworth, J., and Taipe, E. (2019). Self-entrainment motion of a slow-moving landslide inferred from landsat-8 time series. *Journal of Geophysical Research: Earth Surface*, 124(5):1201–1216.

[Lacroix et al., 2018] Lacroix, P., Bièvre, G., Pathier, E., Kniess, U., and Jongmans, D. (2018). Use of sentinel-2 images for the detection of precursory motions before landslide failures. *Remote Sensing of Environment*, 215:507–516.

[Lacroix et al., 2020] Lacroix, P., Handwerger, A. L., and Bièvre, G. (2020). Life and death of slow-moving landslides. *Nature Reviews Earth & Environment*, 1(8):404–419.

[Lacroix and Helmstetter, 2011] Lacroix, P. and Helmstetter, A. (2011). Location of seismic signals associated with microearthquakes and rockfalls on the séchilienne landslide, french alps. *Bulletin of the Seismological Society of America*, 101(1):341–353.

[Landaluce et al., 2020] Landaluce, H., Arjona, L., Perallos, A., Falcone, F., Angulo, I., and Muralter, F. (2020). A review of iot sensing applications and challenges using rfid and wireless sensor networks. *Sensors*, 20(9):2495.

[Langley et al., 2017] Langley, R. B., Teunissen, P. J., and Montenbruck, O. (2017). Introduction to gnss. *Springer handbook of global navigation satellite systems*, pages 3–23.

[Larose et al., 2015] Larose, E., Carrière, S., Voisin, C., Bottelin, P., Baillet, L., Guéguen, P., Walter, F., Jongmans, D., Guillier, B., Garambois, S., et al. (2015). Environmental seismology: What can we learn on earth surface processes with ambient noise? *Journal of Applied Geophysics*, 116:62–74.

[Lazaro et al., 2009] Lazaro, A., Girbau, D., and Salinas, D. (2009). Radio link budgets for uhf rfid on multipath environments. *IEEE transactions on antennas and propagation*, 57(4):1241–1251.

[Le Breton, 2019] Le Breton, M. (2019). *Suivi temporel d'un glissement de terrain à l'aide d'étiquettes RFID passives, couplé à l'observation de pluviométrie et de bruit sismique ambiant.* PhD thesis, Université Grenoble Alpes (ComUE).

[Le Breton et al., 2023a] Le Breton, M., Baillet, L., and Larose, E. (2023a). Tomography of the quantity of grass using rfid propagation-based sensing. In *2023 IEEE 13th International Conference on RFID Technology and Applications (RFID-TA)*, pages 142–145. IEEE.

[Le Breton et al., 2017] Le Breton, M., Baillet, L., Larose, E., Rey, E., Benech, P., Jongmans, D., and Guyoton, F. (2017). Outdoor uhf rfid: Phase stabilization for real-world applications. *IEEE Journal of Radio Frequency Identification*, 1(4):279–290.

[Le Breton et al., 2019] Le Breton, M., Baillet, L., Larose, E., Rey, E., Benech, P., Jongmans, D., Guyoton, F., and Jaboyedoff, M. (2019). Passive radio-frequency identification ranging, a dense and weather-robust technique for landslide displacement monitoring. *Engineering geology*, 250:1–10.

[Le Breton et al., 2021] Le Breton, M., Bontemps, N., Guillemot, A., Baillet, L., and Larose, É. (2021). Landslide monitoring using seismic ambient noise correlation: challenges and applications. *Earth-Science Reviews*, 216:103518.

[Le Breton et al., 2023b] Le Breton, M., Larose, É., Baillet, L., Lejeune, Y., and van Herwijnen, A. (2023b). Monitoring snow water equivalent using the phase of rfid signals. *The Cryosphere*, 17(8):3137–3156.

[Le Breton et al., 2022] Le Breton, M., Liébault, F., Baillet, L., Charléty, A., Larose, É., and Tedjini, S. (2022). Dense and long-term monitoring of earth surface processes with passive rfid—a review. *Earth-Science Reviews*, page 104225.

[Li et al., 2019a] Li, C., Mo, L., and Zhang, D. (2019a). Review on uhf rfid localization methods. *IEEE Journal of Radio Frequency Identification*, 3(4):205–215.

[Li et al., 2019b] Li, C., Tanghe, E., Plets, D., Suanet, P., Hoebeke, J., De Poorter, E., and Joseph, W. (2019b). Repos: Relative position estimation of uhf-rfid tags for item-level localization. In *2019 IEEE International Conference on RFID Technology and Applications (RFID-TA)*, pages 357–361. IEEE.

[Li et al., 2021] Li, C., Tanghe, E., Suanet, P., Plets, D., Hoebeke, J., De Poorter, E., and Joseph, W. (2021). Reloc 2.0: Uhf-rfid relative localization for drone-based inventory management. *IEEE Transactions on Instrumentation and Measurement*, 70:1–13.

[Li et al., 2022] Li, C., Tanghe, E., Suanet, P., Plets, D., Hoebeke, J., Martens, L., De Poorter, E., and Joseph, W. (2022). Deep learning enables robust drone-based uhf-rfid localization in warehouses. In *2022 3rd URSI Atlantic and Asia Pacific Radio Science Meeting (AT-AP-RASC)*, pages 1–4. IEEE.

[Li et al., 2020] Li, J., Pei, Y., Zhao, S., Xiao, R., Sang, X., and Zhang, C. (2020). A review of remote sensing for environmental monitoring in china. *Remote Sensing*, 12(7):1130.

[Li et al., 2023] Li, X., Handwerger, A. L., and Buscarnera, G. (2023). Viscoplastic modelling of rainfall-driven slow-moving landslides: application to california coast ranges. *Landslides*, pages 1–13.

[Li et al., 2009] Li, X., Zhang, Y., and Amin, M. G. (2009). Multifrequency-based range estimation of rfid tags. In *2009 IEEE International Conference on RFID*, pages 147–154. IEEE.

[Li et al., 2017] Li, Y., Huang, J., Jiang, S.-H., Huang, F., and Chang, Z. (2017). A web-based gps system for displacement monitoring and failure mechanism analysis of reservoir landslide. *Scientific reports*, 7(1):1–13.

[Liu et al., 2019] Liu, T., Shang, Z., Wu, J., Zhou, D., and Yan, S. (2019). Improved branch-cut phase unwrapping strategy based on dynamic adjacent table. *The Journal of Engineering*, 2019(19):5805–5809.

[Lobkis and Weaver, 2001] Lobkis, O. I. and Weaver, R. L. (2001). On the emergence of the green's function in the correlations of a diffuse field. *The Journal of the Acoustical Society of America*, 110(6):3011–3017.

[Loffeld et al., 2007] Loffeld, O., Nies, H., Knedlik, S., and Yu, W. (2007). Phase unwrapping for sar interferometry—a data fusion approach by kalman filtering. *IEEE Transactions on Geoscience and Remote Sensing*, 46(1):47–58.

[Lu and Zeng, 2020] Lu, F. and Zeng, H. (2020). Application of kalman filter model in the landslide deformation forecast. *Scientific Reports*, 10(1):1–12.

[Lu et al., 2016] Lu, S., Xu, C., and Zhong, R. Y. (2016). An active rfid tag-enabled locating approach with multipath effect elimination in agv. *IEEE Transactions on Automation Science and Engineering*, 13(3):1333–1342.

[Lunga and Dias, 2022] Lunga, D. and Dias, P. (2022). Advancing data fusion in earth sciences. In *IGARSS 2022-2022 IEEE International Geoscience and Remote Sensing Symposium*, pages 5077–5080. IEEE.

[Lytle, 1974] Lytle, R. J. (1974). Measurement of earth medium electrical characteristics: Techniques, results, and applications. *IEEE Transactions on Geoscience Electronics*, 12(3):81–101.

[Ma et al., 2020] Ma, Y., Liu, H., Zhang, Y., and Jiang, Y. (2020). The influence of the nonideal phase offset on sar-based localization in passive uhf rfid. *IEEE Transactions on Antennas and Propagation*, 68(8):6346–6354.

[Ma et al., 2017] Ma, Y., Selby, N., and Adib, F. (2017). Minding the billions: Ultra-wideband localization for deployed rfid tags. In *Proceedings of the 23rd annual international conference on mobile computing and networking*, pages 248–260.

[Ma et al., 2018] Ma, Y., Wang, B., Pei, S., Zhang, Y., Zhang, S., and Yu, J. (2018). An indoor localization method based on aoa and pdoa using virtual stations in multipath and nlos environments for passive uhf rfid. *IEEE Access*, 6:31772–31782.

[Maciuk, 2018] Maciuk, K. (2018). Gps-only, glonass-only and combined gps+ glonass absolute positioning under different sky view conditions. *Tehnički vjesnik*, 25(3):933–939.

[Magnago et al., 2019] Magnago, V., Palopoli, L., Buffi, A., Tellini, B., Motroni, A., Nepa, P., Macii, D., and Fontanelli, D. (2019). Ranging-free uhf-rfid robot positioning through phase measurements of passive tags. *IEEE Transactions on Instrumentation and Measurement*, 69(5):2408–2418.

[Mainsant et al., 2012] Mainsant, G., Larose, E., Brönnimann, C., Jongmans, D., Michoud, C., and Jaboyedoff, M. (2012). Ambient seismic noise monitoring of a clay landslide: Toward failure prediction. *Journal of Geophysical Research: Earth Surface*, 117(F1).

[Mansour et al., 2011] Mansour, M. F., Morgenstern, N. R., and Martin, C. D. (2011). Expected damage from displacement of slow-moving slides. *Landslides*, 8:117–131.

[Mao et al., 2019] Mao, F., Khamis, K., Krause, S., Clark, J., and Hannah, D. M. (2019). Low-cost environmental sensor networks: Recent advances and future directions. *Frontiers in Earth Science*, 7:221.

[Martinelli, 2015] Martinelli, F. (2015). A robot localization system combining rssi and phase shift in uhf-rfid signals. *IEEE Transactions on Control Systems Technology*, 23(5):1782–1796.

[Mathieu, 2023] Mathieu, L. B. (2023). Increased ranging accuracy of rfid tags in etsi regions using 53mhz wide dual bands. In *2023 IEEE 13th International Conference on RFID Technology and Applications (RFID-TA)*, pages 197–200. IEEE.

[Matsuura et al., 2008] Matsuura, S., Asano, S., and Okamoto, T. (2008). Relationship between rain and/or meltwater, pore-water pressure and displacement of a reactivated landslide. *Engineering Geology*, 101(1-2):49–59.

[Megalou et al., 2022] Megalou, S., Chatzistefanou, A. R., Tzitzis, A., Malama, A., Yioultsis, T., and Dimitriou, A. G. (2022). Hyperbolic positioning and tracking of moving uhf-rfid tags by exploiting neural networks. In *2022 16th European Conference on Antennas and Propagation (EuCAP)*, pages 01–05. IEEE.

[Meisina, 2006] Meisina, C. (2006). Characterisation of weathered clayey soils responsible for shallow landslides. *Natural Hazards and Earth System Sciences*, 6(5):825–838.

[Miesen et al., 2011a] Miesen, R., Ebelt, R., Kirsch, F., Schäfer, T., Li, G., Wang, H., and Vossiek, M. (2011a). Where is the tag? *IEEE Microwave Magazine*, 12(7):S49–S63.

[Miesen et al., 2011b] Miesen, R., Kirsch, F., and Vossiek, M. (2011b). Holographic localization of passive uhf rfid transponders. In *2011 IEEE international conference on RFID*, pages 32–37. IEEE.

[Miesen et al., 2013] Miesen, R., Kirsch, F., and Vossiek, M. (2013). Uhf rfid localization based on synthetic apertures. *IEEE Transactions on Automation Science and Engineering*, 10(3):807–815.

[Mohd Noor et al., 2018] Mohd Noor, N., Abdullah, A., and Hashim, M. (2018). Remote sensing uav/drones and its applications for urban areas: A review. In *IOP conference series: Earth and environmental science*, volume 169, page 012003. IOP Publishing.

[Monico et al., 2019] Monico, J. F. G., Marques, H. A., Tsuchiya, Í., Oyama, R. T., Queiroz, W. R. S. d., Souza, M. C. d., and Wentz, J. P. (2019). Real time ppp applied to airplane fligtht tests. *Boletim de Ciências Geodésicas*, 25.

[Monserrat et al., 2014] Monserrat, O., Crosetto, M., and Luzi, G. (2014). A review of ground-based sar interferometry for deformation measurement. *ISPRS Journal of Photogrammetry and Remote Sensing*, 93:40–48.

[Moreau et al., 2014] Moreau, L., Hunter, A. J., Velichko, A., and Wilcox, P. D. (2014). 3-d reconstruction of sub-wavelength scatterers from the measurement of scattered fields in elastic waveguides. *IEEE transactions on ultrasonics, ferroelectrics, and frequency control*, 61(11):1864–1879.

[Motroni et al., 2021] Motroni, A., Buffi, A., and Nepa, P. (2021). A survey on indoor vehicle localization through rfid technology. *IEEE Access*, 9:17921–17942.

[Motroni and Nepa,] Motroni, A. and Nepa, P. Uav-based 3d localization of passive uhf-rfid tags empowering outdoor stock management.

[Motroni et al., 2018] Motroni, A., Nepa, P., Magnago, V., Buffi, A., Tellini, B., Fontanelli, D., and Macii, D. (2018). Sar-based indoor localization of uhf-rfid tags via mobile robot. In *2018 International Conference on Indoor Positioning and Indoor Navigation (IPIN)*, pages 1–8. IEEE.

[Mucchi et al., 2018] Mucchi, L., Jayousi, S., Martinelli, A., Caputo, S., Intrieri, E., Gigli, G., Gracchi, T., Mugnai, F., Favalli, M., Fornaciai, A., et al. (2018). A flexible wireless sensor network based on ultra-wide band technology for ground instability monitoring. *Sensors*, 18(9):2948.

[Nemati et al., 2017] Nemati, E., Batteate, C., and Jerrett, M. (2017). Opportunistic environmental sensing with smartphones: a critical review of current literature and applications. *Current environmental health reports*, 4:306–318.

[Nguyen et al., 2017] Nguyen, C. T., Nguyen, C. T., Bui, H. H., Nguyen, G. D., and Fukagawa, R. (2017). A new sph-based approach to simulation of granular flows using viscous damping and stress regularisation. *Landslides*, 14:69–81.

[Ni et al., 2003] Ni, L. M., Liu, Y., Lau, Y. C., and Patil, A. P. (2003). Landmarc: Indoor location sensing using active rfid. In *Proceedings of the First IEEE International Conference on Pervasive Computing and Communications, 2003.(PerCom 2003).*, pages 407–415. IEEE.

[Niethammer et al., 2012] Niethammer, U., James, M., Rothmund, S., Travelletti, J., and Joswig, M. (2012). Uav-based remote sensing of the super-sauze landslide: Evaluation and results. *Engineering Geology*, 128:2–11.

[Nikitin et al., 2010] Nikitin, P. V., Martinez, R., Ramamurthy, S., Leland, H., Spiess, G., and Rao, K. (2010). Phase based spatial identification of uhf rfid tags. In *2010 IEEE International Conference on RFID (IEEE RFID 2010)*, pages 102–109. IEEE.

[Nikitin and Rao, 2008] Nikitin, P. V. and Rao, K. S. (2008). Antennas and propagation in uhf rfid systems. In *2008 IEEE international conference on RFID*, pages 277–288. IEEE.

[Norrdine, 2012] Norrdine, A. (2012). An algebraic solution to the multilateration problem. In *Proceedings of the 15th international conference on indoor positioning and indoor navigation, Sydney, Australia*, volume 1315.

[Nunes-Silva et al., 2019] Nunes-Silva, P., Hrncir, M., Guimarães, J., Arruda, H., Costa, L., Pessin, G., Siqueira, J., De Souza, P., and Imperatriz-Fonseca, V. (2019). Applications of rfid technology on the study of bees. *Insectes sociaux*, 66(1):15–24.

[Occhiuzzi et al., 2011] Occhiuzzi, C., Paggi, C., and Marrocco, G. (2011). Passive rfid strain-sensor based on meander-line antennas. *IEEE Transactions on Antennas and Propagation*, 59(12):4836–4840.

[Opromolla et al., 2016] Opromolla, R., Fasano, G., Rufino, G., Grassi, M., and Savvaris, A. (2016). Lidar-inertial integration for uav localization and mapping in complex environments. In *2016 International Conference on Unmanned Aircraft Systems (ICUAS)*, pages 649–656. IEEE.

[Parr et al., 2013] Parr, A., Miesen, R., and Vossiek, M. (2013). Inverse sar approach for localization of moving rfid tags. In *2013 IEEE International Conference on RFID (RFID)*, pages 104–109. IEEE.

[Paul and Buytaert, 2018] Paul, J. D. and Buytaert, W. (2018). Citizen science and low-cost sensors for integrated water resources management. In *Advances in Chemical Pollution, Environmental Management and Protection*, volume 3, pages 1–33. Elsevier.

[Pecoraro et al., 2019] Pecoraro, G., Calvello, M., and Piciullo, L. (2019). Monitoring strategies for local landslide early warning systems. *Landslides*, 16:213–231.

[Pelka et al., 2014] Pelka, M., Bollmeyer, C., and Hellbrück, H. (2014). Accurate radio distance estimation by phase measurements with multiple frequencies. In *2014 International Conference on Indoor Positioning and Indoor Navigation (IPIN)*, pages 142–151. IEEE.

[Peng et al., 2021] Peng, C., Jiang, H., and Qu, L. (2021). Deep convolutional neural network for passive rfid tag localization via joint rssi and pdoa fingerprint features. *IEEE Access*, 9:15441–15451.

[Pichorim et al., 2018] Pichorim, S. F., Gomes, N. J., and Batchelor, J. C. (2018). Two solutions of soil moisture sensing with rfid for landslide monitoring. *Sensors*, 18(2):452.

[Piégay et al., 2020] Piégay, H., Arnaud, F., Belletti, B., Bertrand, M., Bizzi, S., Carbonneau, P., Dufour, S., Liébault, F., Ruiz-Villanueva, V., and Slater, L. (2020). Remotely sensed rivers in the anthropocene: State of the art and prospects. *Earth Surface Processes and Landforms*, 45(1):157–188.

[Placidi et al., 2020] Placidi, P., Gasperini, L., Grassi, A., Cecconi, M., and Scorzoni, A. (2020). Characterization of low-cost capacitive soil moisture sensors for iot networks. *Sensors*, 20(12):3585.

[Pörtner et al., 2022] Pörtner, H.-O., Roberts, D. C., Adams, H., Adler, C., Aldunce, P., Ali, E., Begum, R. A., Betts, R., Kerr, R. B., Biesbroek, R., et al. (2022). *Climate change 2022: Impacts, adaptation and vulnerability*. IPCC Geneva, Switzerland:.

[Potyrailo et al., 2011] Potyrailo, R. A., Surman, C., Sivavec, T., and Wortley, T. (2011). Passive multivariable rfid ph sensors. In *2011 IEEE International Conference on RFID-Technologies and Applications*, pages 533–536. IEEE.

[Povalac and Sebesta, 2011] Povalac, A. and Sebesta, J. (2011). Phase difference of arrival distance estimation for rfid tags in frequency domain. In *2011 IEEE International Conference on RFID-Technologies and Applications*, pages 188–193. IEEE.

[Qian et al., 2021] Qian, J., Chen, K., Chen, Q., Yang, Y., Zhang, J., and Chen, S. (2021). Robust visual-lidar simultaneous localization and mapping system for uav. *IEEE Geoscience and Remote Sensing Letters*, 19:1–5.

[Qiu et al., 2017] Qiu, L., Liang, X., and Huang, Z. (2017). Patl: A rfid tag localization based on phased array antenna. *Scientific Reports*, 7(1):1–12.

[Qiu et al., 2020] Qiu, Z., Jiao, M., Jiang, T., and Zhou, L. (2020). Dam structure deformation monitoring by gb-insar approach. *IEEE Access*, 8:123287–123296.

[Ramakrishnan and Deavours, 2006] Ramakrishnan, K. M. and Deavours, D. D. (2006). Performance benchmarks for passive uhf rfid tags. In *13th GI/ITG Conference-Measuring, Modelling and Evaluation of Computer and Communication Systems*, pages 1–18. VDE.

[Ramesh, 2009] Ramesh, M. V. (2009). Real-time wireless sensor network for landslide detection. In *2009 Third International Conference on Sensor Technologies and Applications*, pages 405–409. IEEE.

[Ramesh, 2014] Ramesh, M. V. (2014). Design, development, and deployment of a wireless sensor network for detection of landslides. *Ad Hoc Networks*, 13:2–18.

[Rayhana et al., 2021] Rayhana, R., Xiao, G., and Liu, Z. (2021). Rfid sensing technologies for smart agriculture. *IEEE Instrumentation & Measurement Magazine*, 24(3):50–60.

[Rembold, 2009] Rembold, B. (2009). Optimum modulation efficiency and sideband backscatter power response of rfid-tags. *Frequenz*, 63(1-2):9–13.

[Remzi et al., 2020] Remzi, E., Alkan, E., and AYDIN, A. (2020). A comparative analysis of uav-rtk and uav-ppk methods in mapping different surface types. *European Journal of Forest Engineering*, 7(1):12–25.

[Robustelli et al., 2023] Robustelli, U., Cutugno, M., and Pugliano, G. (2023). Low-cost gnss and ppp-rtk: Investigating the capabilities of the u-blox zed-f9p module. *Sensors*, 23(13):6074.

[Rohan et al., 2023] Rohan, T., Shelef, E., Mirus, B., and Coleman, T. (2023). Prolonged influence of urbanization on landslide susceptibility. *Landslides*, pages 1–15.

[Rohmat Rose et al., 2020] Rohmat Rose, N. D., Low, T. J., and Ahmad, M. (2020). 3d trilateration localization using rssi in indoor environment. *International Journal of Advanced Computer Science and Applications*, 11(2):385–391.

[Rosone et al., 2018] Rosone, M., Ziccarelli, M., Ferrari, A., and Farulla, C. A. (2018). On the re-activation of a large landslide induced by rainfall in highly fissured clays. *Engineering Geology*, 235:20–38.

[Rossi et al., 2018] Rossi, G., Tanteri, L., Tofani, V., Vannocci, P., Moretti, S., and Casagli, N. (2018). Multitemporal uav surveys for landslide mapping and characterization. *Landslides*, 15:1045–1052.

[Sarkka et al., 2011a] Sarkka, S., Viikari, V. V., Huusko, M., and Jaakkola, K. (2011a). Phase-based uhf rfid tracking with nonlinear kalman filtering and smoothing. *IEEE Sensors Journal*, 12(5):904–910.

[Sarkka et al., 2011b] Sarkka, S., Viikari, V. V., Huusko, M., and Jaakkola, K. (2011b). Phase-based uhf rfid tracking with nonlinear kalman filtering and smoothing. *IEEE Sensors Journal*, 12(5):904–910.

[Sasiadek and Hartana, 2000] Sasiadek, J. and Hartana, P. (2000). Sensor data fusion using kalman filter. In *Proceedings of the Third International Conference on Information Fusion*, volume 2, pages WED5–19. IEEE.

[Scaioni et al., 2014] Scaioni, M., Longoni, L., Melillo, V., and Papini, M. (2014). Remote sensing for landslide investigations: An overview of recent achievements and perspectives. *Remote Sensing*, 6(10):9600–9652.

[Schäbitz et al., 2018] Schäbitz, M., Janssen, C., Wenk, H.-R., Wirth, R., Schuck, B., Wetzel, H.-U., Meng, X., and Dresen, G. (2018). Microstructures in landslides in northwest china–implications for creeping displacements? *Journal of Structural Geology*, 106:70–85.

[Scherhäufl et al., 2014] Scherhäufl, M., Pichler, M., and Stelzer, A. (2014). Uhf rfid localization based on phase evaluation of passive tag arrays. *IEEE Transactions on Instrumentation and Measurement*, 64(4):913–922.

[Scherhäufl et al., 2015] Scherhäufl, M., Pichler, M., and Stelzer, A. (2015). Uhf rfid localization based on evaluation of backscattered tag signals. *IEEE Transactions on Instrumentation and Measurement*, 64(11):2889–2899.

[Schneider et al., 2014] Schneider, J. M., Turowski, J. M., Rickenmann, D., Hegglin, R., Arrigo, S., Mao, L., and Kirchner, J. W. (2014). Scaling relationships between bed load volumes, transport distances, and stream power in steep mountain channels. *Journal of Geophysical Research: Earth Surface*, 119(3):533–549.

[Schneiderbauer and Ehrlich, 2004] Schneiderbauer, S. and Ehrlich, D. (2004). Risk, hazard and people's vulnerability to natural hazards. *A review of definitions, concepts and data. European Commission Joint Research Centre. EUR*, 21410:40.

[Schneiderbauer et al., 2021] Schneiderbauer, S., Pisa, P. F., Delves, J. L., Pedoth, L., Rufat, S., Erschbamer, M., Thaler, T., Carnelli, F., and Granados-Chahin, S. (2021). Risk perception of climate change and natural hazards in global mountain regions: A critical review. *Science of the total environment*, 784:146957.

[Schulz et al., 2012] Schulz, W., Coe, J., Shurtleff, B., Panosky, J., Farina, P., Ricci, P., and Barsacchi, G. (2012). Kinematics of the slumgullion landslide revealed by ground-based insar surveys. *Landslides and Engineered Slopes, Protecting Society through Improved Understanding*, 2:1273–1279.

[Schulz et al., 2017] Schulz, W. H., Coe, J. A., Ricci, P. P., Smoczyk, G. M., Shurtleff, B. L., and Panosky, J. (2017). Landslide kinematics and their potential controls from hourly to decadal timescales: Insights from integrating ground-based insar measurements with structural maps and long-term monitoring data. *Geomorphology*, 285:121–136.

[Schulz et al., 2018] Schulz, W. H., Smith, J. B., Wang, G., Jiang, Y., and Roering, J. J. (2018). Clayey landslide initiation and acceleration strongly modulated by soil swelling. *Geophysical Research Letters*, 45(4):1888–1896.

[Šegina et al., 2020] Šegina, E., Peternel, T., Urbančič, T., Realini, E., Zupan, M., Jež, J., Caldera, S., Gatti, A., Tagliaferro, G., Consoli, A., et al. (2020). Monitoring surface displacement of a deep-seated landslide by a low-cost and near real-time gnss system. *Remote sensing*, 12(20):3375.

[Segoni et al., 2018] Segoni, S., Piciullo, L., and Gariano, S. L. (2018). A review of the recent literature on rainfall thresholds for landslide occurrence. *Landslides*, 15(8):1483–1501.

[Serripierri et al., 2022] Serripierri, A., Moreau, L., Boue, P., Weiss, J., and Roux, P. (2022). Recovering and monitoring the thickness, density, and elastic properties of sea ice from seismic noise recorded in svalbard. *The Cryosphere*, 16(6):2527–2543.

[Shannon, 1949] Shannon, C. E. (1949). Communication in the presence of noise. *Proceedings of the IRE*, 37(1):10–21.

[Shen et al., 2019] Shen, L., Zhang, Q., Pang, J., Xu, H., and Li, P. (2019). Prdl: relative localization method of rfid tags via phase and rssi based on deep learning. *IEEE Access*, 7:20249–20261.

[Shirzaei and Walter, 2011] Shirzaei, M. and Walter, T. R. (2011). Estimating the effect of satellite orbital error using wavelet-based robust regression applied to insar deformation data. *IEEE transactions on geoscience and remote sensing*, 49(11):4600–4605.

[Siachalou et al., 2019] Siachalou, S., Megalou, S., Tzitzis, A., Tsardoulias, E., Bletsas, A., Sahalos, J., Yioultsis, T., and Dimitriou, A. G. (2019). Robotic inventorying and localization of rfid tags, exploiting phase-fingerprinting. In *2019 IEEE International Conference on RFID Technology and Applications (RFID-TA)*, pages 362–367. IEEE.

[Sirtkaya et al., 2013] Sirtkaya, S., Seymen, B., and Alatan, A. A. (2013). Loosely coupled kalman filtering for fusion of visual odometry and inertial navigation. In *Proceedings of the 16th International Conference on Information Fusion*, pages 219–226. IEEE.

[Sorrells, 1998] Sorrells, P. (1998). Passive rfid basics. *Microchip Technology Inc*, 7.

[Stähli et al., 2015] Stähli, M., Sättele, M., Huggel, C., McArdell, B. W., Lehmann, P., Van Herwijnen, A., Berne, A., Schleiss, M., Ferrari, A., Kos, A., et al. (2015). Monitoring and prediction in early warning systems for rapid mass movements. *Natural Hazards and Earth System Science*, 15(4):905–917.

[Stella and Shi, 2003] Stella, X. Y. and Shi, J. (2003). Multiclass spectral clustering. In *Computer vision, IEEE international conference on*, volume 2, pages 313–313. IEEE Computer Society.

[Strangfeld et al., 2019] Strangfeld, C., Johann, S., and Bartholmai, M. (2019). Smart rfid sensors embedded in building structures for early damage detection and long-term monitoring. *Sensors*, 19(24):5514.

[Strigaro et al., 2019] Strigaro, D., Cannata, M., and Antonovic, M. (2019). Boosting a weather monitoring system in low income economies using open and non-conventional systems: Data quality analysis. *Sensors*, 19(5):1185.

[Strozzi et al., 2005] Strozzi, T., Farina, P., Corsini, A., Ambrosi, C., Thüring, M., Zilger, J., Wiesmann, A., Wegmüller, U., and Werner, C. (2005). Survey and monitoring of landslide displacements by means of l-band satellite sar interferometry. *Landslides*, 2(3):193–201.

[Stumpf et al., 2015] Stumpf, A., Malet, J.-P., Allemand, P., Pierrot-Deseilligny, M., and Skupinski, G. (2015). Ground-based multi-view photogrammetry for the monitoring of landslide deformation and erosion. *Geomorphology*, 231:130–145.

[Subedi et al., 2017] Subedi, S., Pauls, E., and Zhang, Y. D. (2017). Accurate localization and tracking of a passive rfid reader based on rssi measurements. *IEEE Journal of Radio Frequency Identification*, 1(2):144–154.

[Sun and Deng, 2004] Sun, S.-L. and Deng, Z.-L. (2004). Multi-sensor optimal information fusion kalman filter. *Automatica*, 40(6):1017–1023.

[Suzuki et al., 2016] Suzuki, T., Takahashi, Y., and Amano, Y. (2016). Precise uav position and attitude estimation by multiple gnss receivers for 3d mapping. In *Proceedings of the 29th International Technical Meeting of the Satellite Division of The Institute of Navigation (ION GNSS+ 2016)*, pages 1455–1464.

[Takasu and Yasuda, 2009] Takasu, T. and Yasuda, A. (2009). Development of the low-cost rtk-gps receiver with an open source program package rtklib. In *International symposium on GPS/GNSS*, volume 1, pages 1–6. International Convention Center Jeju Korea Seogwipo-si, Republic of Korea.

[Tan et al., 2020] Tan, Q., Wang, P., Hu, J., Zhou, P., Bai, M., and Hu, J. (2020). The application of multi-sensor target tracking and fusion technology to the comprehensive early warning information extraction of landslide multi-point monitoring data. *Measurement*, 166:108044.

[Tan and Sidhu, 2022] Tan, W. C. and Sidhu, M. S. (2022). Review of rfid and iot integration in supply chain management. *Operations Research Perspectives*, 9:100229.

[Tao et al., 2020] Tao, B., Wu, H., Gong, Z., Yin, Z., and Ding, H. (2020). An rfid-based mobile robot localization method combining phase difference and readability. *IEEE Transactions on Automation Science and Engineering*, 18(3):1406–1416.

[Tarchi et al., 2003] Tarchi, D., Casagli, N., Fanti, R., Leva, D. D., Luzi, G., Pasuto, A., Pieraccini, M., and Silvano, S. (2003). Landslide monitoring by using ground-based sar interferometry: an example of application to the tessina landslide in italy. *Engineering geology*, 68(1-2):15–30.

[Terzaghi, 1950] Terzaghi, K. (1950). Mechanism of landslides.

[Tesch et al., 2015] Tesch, D. A., Berz, E. L., and Hessel, F. P. (2015). Rfid indoor localization based on doppler effect. In *Sixteenth International Symposium on Quality Electronic Design*, pages 556–560. IEEE.

[Thery et al., 2020] Thery, R., Guillemot, A., Abraham, O., and Larose, E. (2020). Tracking fluids in multiple scattering and highly porous materials: toward applications in non-destructive testing and seismic monitoring. *Ultrasonics*, 102:106019.

[Tomaštík et al., 2019] Tomaštík, J., Mokroš, M., Surovỳ, P., Grznárová, A., and Merganič, J. (2019). Uav rtk/ppk method—an optimal solution for mapping inaccessible forested areas? *Remote sensing*, 11(6):721.

[Tonnellier et al., 2013] Tonnellier, A., Helmstetter, A., Malet, J.-P., Schmittbuhl, J., Corsini, A., and Joswig, M. (2013). Seismic monitoring of soft-rock landslides: the super-sauze and valoria case studies. *Geophysical Journal International*, 193(3):1515–1536.

[Tripicchio et al., 2022] Tripicchio, P., D'Avella, S., and Unetti, M. (2022). Efficient localization in warehouse logistics: a comparison of lms approaches for 3d multilateration of passive uhf rfid tags. *The International Journal of Advanced Manufacturing Technology*, 120(7):4977–4988.

[Tripicchio et al., 2021] Tripicchio, P., Unetti, M., D'Avella, S., Buffi, A., Motroni, A., Bernardini, F., and Nepa, P. (2021). A synthetic aperture uhf rfid localization method by phase unwrapping and hyperbolic intersection. *IEEE Transactions on Automation Science and Engineering*, 19(2):933–945.

[Tsanousa et al., 2022] Tsanousa, A., Bektsis, E., Kyriakopoulos, C., González, A. G., Leturiondo, U., Gialampoukidis, I., Karakostas, A., Vrochidis, S., and Kompatsiaris, I. (2022). A review of multisensor data fusion solutions in smart manufacturing: Systems and trends. *Sensors*, 22(5):1734.

[Turko et al., 2021] Turko, M., Gosset, M., Kacou, M., Bouvier, C., Chahinian, N., Boone, A., and Alcoba, M. (2021). Rainfall measurement from commercial microwave links for urban hydrology in africa: a simulation framework for sensitivity analysis. *Journal of Hydrometeorology*, 22(7):1819–1834.

[Turner, 2018] Turner, A. K. (2018). Social and environmental impacts of landslides. *Innovative Infrastructure Solutions*, 3:1–25.

[Tzitzis et al., 2021] Tzitzis, A., Chatzistefanou, A. R., Yioultsis, T. V., and Dimitriou, A. G. (2021). A real-time multi-antenna sar-based method for 3d localization of rfid tags by a moving robot. *IEEE Journal of Radio Frequency Identification*, 5(2):207–221.

[Tzitzis et al., 2019] Tzitzis, A., Megalou, S., Siachalou, S., Emmanouil, T. G., Kehagias, A., Yioultsis, T. V., and Dimitriou, A. G. (2019). Localization of rfid tags by a moving robot, via phase unwrapping and non-linear optimization. *IEEE Journal of Radio Frequency Identification*, 3(4):216–226.

[Uhlemann et al., 2016] Uhlemann, S., Hagedorn, S., Dashwood, B., Maurer, H., Gunn, D., Dijkstra, T., and Chambers, J. (2016). Landslide characterization using p-and s-wave seismic refraction tomography—the importance of elastic moduli. *Journal of Applied Geophysics*, 134:64–76.

[V Ramesh and Vasudevan, 2012] V Ramesh, M. and Vasudevan, N. (2012). The deployment of deep-earth sensor probes for landslide detection. *Landslides*, 9:457–474.

[Van Asch et al., 1999] Van Asch, T. W., Buma, J., and Van Beek, L. (1999). A view on some hydrological triggering systems in landslides. *Geomorphology*, 30(1-2):25–32.

[Van Loan, 1976] Van Loan, C. F. (1976). Generalizing the singular value decomposition. *SIAM Journal on numerical Analysis*, 13(1):76–83.

[Van Ryzin, 1980] Van Ryzin, J. (1980). Quantitative risk assessment. *Journal of Occupational Medicine*, pages 321–326.

[Varnes, 1978] Varnes, D. J. (1978). Slope movement types and processes. *Special report*, 176:11–33.

[Voisin et al., 2016] Voisin, C., Garambois, S., Massey, C., and Brossier, R. (2016). Seismic noise monitoring of the water table in a deep-seated, slow-moving landslide. *Interpretation*, 4(3):SJ67–SJ76.

[Voisin et al., 2017] Voisin, C., Guzmán, M. A. R., Refloch, A., Taruselli, M., and Garambois, S. (2017). Groundwater monitoring with passive seismic interferometry. *Journal of Water Resource and Protection*, 9(12):1414–1427.

[Vojtech et al., 2015] Vojtech, L., Nerada, M., Hrad, J., and Bortel, R. (2015). Outdoor localization technique using active rfid technology aimed for security and disaster management applications. In *Proceedings of the 2015 16th International Carpathian Control Conference (ICCC)*, pages 586–589. IEEE.

[Von Luxburg, 2007] Von Luxburg, U. (2007). A tutorial on spectral clustering. *Statistics and computing*, 17:395–416.

[Wagih and Shi, 2021] Wagih, M. and Shi, J. (2021). Wireless ice detection and monitoring using flexible uhf rfid tags. *IEEE Sensors Journal*, 21(17):18715–18724.

[Wan et al., 2022] Wan, G., Li, M., Zhang, M., Kang, L., and Xie, L. (2022). A novel information fusion method of rfid strain sensor based on microstrip notch circuit. *IEEE Transactions on Instrumentation and Measurement*, 71:1–10.

[Wang et al., 2020a] Wang, G., Qian, C., Cui, K., Shi, X., Ding, H., Xi, W., Zhao, J., and Han, J. (2020a). A universal method to combat multipaths for rfid sensing. In *IEEE INFOCOM 2020-IEEE Conference on Computer Communications*, pages 277–286. IEEE.

[Wang et al., 2011] Wang, H., Weaver, J. B., Perreard, I. I., Doyley, M. M., and Paulsen, K. D. (2011). A three-dimensional quality-guided phase unwrapping method for mr elastography. *Physics in Medicine & Biology*, 56(13):3935.

[Wang et al., 2020b] Wang, Y., Hong, W., Zhang, Y., Lin, Y., Li, Y., Bai, Z., Zhang, Q., Lv, S., Liu, H., and Song, Y. (2020b). Ground-based differential interferometry sar: A review. *IEEE Geoscience and Remote Sensing Magazine*, 8(1):43–70.

[Wang et al., 2016] Wang, Z., Ye, N., Malekian, R., Xiao, F., and Wang, R. (2016). Trackt: Accurate tracking of rfid tags with mm-level accuracy using first-order taylor series approximation. *Ad hoc networks*, 53:132–144.

[Wasmeier, 2003] Wasmeier, P. (2003). The potential of object recognition using a servo-tacheometer tca2003. *Optical*, page 48ff.

[Weiss et al., 2020] Weiss, M., Jacob, F., and Duveiller, G. (2020). Remote sensing for agricultural applications: A meta-review. *Remote sensing of environment*, 236:111402.

[White and Smyth, 2005] White, S. and Smyth, P. (2005). A spectral clustering approach to finding communities in graphs. In *Proceedings of the 2005 SIAM international conference on data mining*, pages 274–285. SIAM.

[Whitney et al., 2018] Whitney, A. M., Parker, J. M., Kratzer, Z. C., Fessler, J. T., and Whitney, J. G. (2018). Reducing rf distance error by characterizing multipath. *IEEE Transactions on Instrumentation and Measurement*, 68(9):3329–3338.

[Wu et al., 2019] Wu, H., Tao, B., Gong, Z., Yin, Z., and Ding, H. (2019). A fast uhf rfid localization method using unwrapped phase-position model. *IEEE Transactions on Automation Science and Engineering*, 16(4):1698–1707.

[Wu et al., 2015] Wu, X., Chen, X., Zhan, F. B., and Hong, S. (2015). Global research trends in landslides during 1991–2014: a bibliometric analysis. *Landslides*, 12:1215–1226.

[Xu et al., 2017] Xu, H., Ding, Y., Li, P., Wang, R., and Li, Y. (2017). An rfid indoor positioning algorithm based on bayesian probability and k-nearest neighbor. *Sensors*, 17(8):1806.

[Xue et al., 2017] Xue, J., Su, B., et al. (2017). Significant remote sensing vegetation indices: A review of developments and applications. *Journal of sensors*, 2017.

[Yang et al., 2019] Yang, Q., Taylor, D. G., Akbar, M. B., and Durgin, G. D. (2019). Analysis of kalman filter-based localization for himr rfid systems. *IEEE Journal of Radio Frequency Identification*, 3(3):164–172.

[Yang et al., 2021] Yang, S., Jin, M., He, Y., and Liu, Y. (2021). Rf-prism: Versatile rfid-based sensing through phase disentangling. In *2021 IEEE 41st International Conference on Distributed Computing Systems (ICDCS)*, pages 1053–1063. IEEE.

[You et al., 2020] You, W., Li, F., Liao, L., and Huang, M. (2020). Data fusion of uwb and imu based on unscented kalman filter for indoor localization of quadrotor uav. *Ieee Access*, 8:64971–64981.

[Zandbergen and Barbeau, 2011] Zandbergen, P. A. and Barbeau, S. J. (2011). Positional accuracy of assisted gps data from high-sensitivity gps-enabled mobile phones. *The Journal of Navigation*, 64(3):381–399.

[Zeng et al., 2019] Zeng, Y., Chen, X., Li, R., and Tan, H.-Z. (2019). Uhf rfid indoor positioning system with phase interference model based on double tag array. *IEEE Access*, 7:76768–76778.

[Zhang, 2010] Zhang, J. (2010). Multi-source remote sensing data fusion: status and trends. *International Journal of Image and Data Fusion*, 1(1):5–24.

[Zhang et al., 2022] Zhang, N., Zhang, W., Liao, K., Zhu, H.-h., Li, Q., and Wang, J. (2022). Deformation prediction of reservoir landslides based on a bayesian optimized random forest-combined kalman filter. *Environmental Earth Sciences*, 81(7):1–14.

[Zhang et al., 2017] Zhang, Y., Xie, L., Bu, Y., Wang, Y., Wu, J., and Lu, S. (2017). 3-dimensional localization via rfid tag array. In *2017 IEEE 14th international conference on mobile ad hoc and sensor systems (MASS)*, pages 353–361. IEEE.

[Zhao and Lu, 2018] Zhao, C. and Lu, Z. (2018). Remote sensing of landslides—a review. *Remote Sensing*, 10(2):279.

[Zhong et al., 2016] Zhong, M., Cao, Q., Guo, J., and Zhou, D. (2016). Simultaneous lever-arm compensation and disturbance attenuation of pos for a uav surveying system. *IEEE Transactions on Instrumentation and Measurement*, 65(12):2828–2839.

[Zhou and Griffin, 2012] Zhou, C. and Griffin, J. D. (2012). Accurate phase-based ranging measurements for backscatter rfid tags. *IEEE Antennas and Wireless Propagation Letters*, 11:152–155.

[Zhou and Griffin, 2018] Zhou, C. and Griffin, J. D. (2018). Phased-based composite ranging for backscatter rf tags: System analysis and measurements. *IEEE Transactions on Antennas and Propagation*, 66(8):4202–4212.